Charge transport in disordered organic and nanocrystalline inorganic semiconductors

Effect of charge carrier density variation

Dissertation zur Erlangung des
naturwissenschaftlichen Doktorgrades
der Julius-Maximilians-Universität Würzburg

vorgelegt von

Maria Sabine Hammer

aus Hirschau

Würzburg 2011

Eingereicht am: 26. Januar 2011
bei der Fakultät für Physik und Astronomie

1. Gutachter: Prof. Dr. Vladimir Dyakonov
2. Gutachter: Prof. Dr. Jean Geurts
3. Gutachter:
der Dissertation.

1. Prüfer: Prof. Dr. Vladimir Dyakonov
2. Prüfer: Prof. Dr. Jean Geurts
3. Prüfer: Prof. Dr. Wolfgang Kinzel
im Promotionskolloquium.

Tag des Promotionskolloquiums: 3. März 2011

Doktorurkunde ausgehändigt am:

Outline

The charge transport properties of disordered organic and nanocrystalline inorganic semiconductors as well as their combinations were investigated in terms of the charge carrier density. The results were discussed in the framework of different theoretical models. In organic semiconductors the presence of electronic disorder is characterized by statistically distributed and localized transport sites which are shown to form a Gaussian density of states. In this electronic environment the charge transport depends on the temperature and the local electric field. Particularly, a dependence of the carrier mobility on the charge concentration is observed which is a critical aspect for the universal description of the charge transport in organic semiconductor based devices. However, inorganic nanocrystalline semiconductors exhibit a somewhat different electronic structure: Within the nanocrystallite the material is assumed to reflect the electronic properties of the respective crystalline bulk material. The interface between adjacent crystallites is characterized by surface states and band bending, which create an energetic barrier. The effective barrier height can be reduced by controlled doping of the nanocrystals which results in improved transfer rates across the barrier. Simultaneously, doping results in the increase of the defect density and in the limitation of the carrier mobility due to scattering. The charge transport in the organic and inorganic material systems was characterized in field-effect-transistor (FET) structures which allow to control the carrier density by accumulation of charge carriers in its conducting channel. The requirements for achieving balanced charge carrier mobilities in FETs based on p- and n-type semiconductor combinations were evaluated beyond the consideration of the immanent transport characteristics in the neat materials. For the experiments, commercially available p- and n-type organic semiconductors were employed. Further, sol–gel synthesized n-type nanocrystalline-ZnO (nc-ZnO) with varied doping concentration was introduced in order to establish an alternative way of customizing the charge transport properties of the neat material and combinations with organic semiconductors. The electron mobility within thin films of methanofullerenes was investigated in the high charge carrier regime. Utilizing temperature dependent measurements it was found that the electron transport in methanofullerene-based FETs can be consistently described by hopping between energy-correlated states in a Gaussian energy landscape. It could be deduced that the highest mobility is achieved for a specific carrier concentration. This result was confirmed for two soluble fullerene derivatives based on C_{60} and C_{70}. The electron transport in nc-ZnO was studied focussing the influence of the carrier density variation which was realized by accumulation in FET structures *and* by extrinsic doping with aluminum. It was found that moderate doping improves the conductivity but mostly has detrimental impact on the mobility. This was attributed to the fact that doping introduces additional defects which act as scattering centers for electrons. Contrary, when increasing the carrier density via accumulation, the ionic and structural defect density remains constant and the mobility was found to increase. The adjustability of the charge transport in ZnO via Al-doping was utilized for application in hybrid poly(3-hexylthiophene)/ZnO:Al transistors. The electrical and morphological modifications of ZnO via doping had a remarkable impact on the hole mobility of poly(3-hexylthiophene). By doping nanocrystalline-ZnO as well as by customizing the morphology in the blend, balanced electron and hole mobilities in the hybrid material were achieved. Concisely, the dependence of the mobility on the carrier concentration was investigated to find a consistent description of the charge transport in semiconductor devices which operate in different regimes of the carrier density.

Inhaltsverzeichnis

1 Introduction

Solution processable semiconductors represent a modern branch of electronic materials, which allow for the low-cost mass production of thin-films via printing and wet chemical coating techniques. Prominent representatives of such functional materials are organic semiconductors such as conjugated polymers and small molecules [17, 39, 80] or inorganic semiconductors [84, 96].

Organic semiconductors are characterized by sp$_2$-hybridized molecular orbitals of which the ensemble of p$_z$-electrons establishes cumulated bonding and antibonding states being separated by an energy gap in the range of 1-3 eV. The characteristic energy of the statistically dispersed electronic states is denoted as highest occupied (HOMO) and lowest unoccupied molecular orbital (LUMO), respectively. In organic semiconductors the presence of electronic disorder (spatial and energetic distribution of states) determines the transport of charges through the respective thin films and interfaces. Their electronic disorder is characterized by statistically distributed and localized transport sites which are shown to form a Gaussian density of states. In this electronic environment the charge transport occurs via thermally assisted tunneling between the localized states and therefore depends on the temperature and the local electric field. Particularly, a dependence of the carrier mobility on the charge concentration is observed, which is a critical aspect for the universal description of the charge transport in diodes, solar cells and field effect transistors.

The properties of nanocrystalline semiconductors in thin films may substantially differ from those of their single crystalline and amorphous counterparts. The electrical and optical properties of nanocrystalline thin films may be dominated by surface- and grain-boundary phenomena: Within the nanoparticle the material is assumed to reflect the electronic properties of the respective crystalline bulk material (eventually altered by quantization effects). However, the surface of the crystallites is characterized by surface states and band bending, which create an energetic barrier between adjacent particles. Such effects lead to unique properties that sensitively depend on the size and the purity of the crystallites. Assuming that carrier transport within the nanocrystals is similar to the crystalline bulk material, charge transfer between neighboring nanocrystals, e.g. in a thin film, is considered to be the dominant mechanism limiting the macroscopic carrier mobility. Efficient charge transport in nanocrystalline thin films therefore requires sufficient thermal compensation of the interfacial barrier heights. In order to control the charge carrier mobility the effective barrier height can be reduced by controlled doping of the nanocrystals which results in improved transfer rates across the barrier. However, to some extent, doping results in the simultaneous increase of the defect density and consequently to stronger limitation of the carrier mobility due to additional scattering centers of ionic, electronic and also structural nature.

The first objective of this thesis was to investigate the charge carrier mobility in disordered organic and nanocrystalline semiconductor materials. In particular the dependence of this macroscopic quantity on the carrier concentration was investigated to find a consistent descrip-

tion of the charge transport in semiconductor devices which operate in different regimes of the carrier density, e.g. diodes, solar cells and field effect transistors. This topic was addressed by studies of the carrier transport in metal-insulator field effect transistors (MISFET) based on the respective materials. Here the carrier concentration was varied by charge accumulation and in the case of nanocrystalline ZnO-films by additional doping with aluminum. The dependence of the mobility on the carrier concentration and temperature was investigated in thin films of organic semiconductors such as soluble fullerene derivatives and nanocrystalline ZnO of varying doping level.

The second objective relates to the application of solution-processed semiconductors in the fundamental unit of logical electronic circuits—the ambipolar field effect transistor. The aim was to study and control the charge transport characteristics in blended thin films of organic and inorganic semiconductors in view of achieving balanced charge carrier mobilities for electrons and holes. The ambipolar charge transport and the options to achieve equalized carrier mobilities is discussed for MISFETs based on organic semiconductor blends (a conjugated polymer with a fullerene derivative) and hybrid composites of a polymer semiconductor and doped ZnO-nanoparticles.

2 Materials

This chapter introduces the semiconductors which were investigated in this study. The organic semiconductors (the conjugated polymer P3HT and the methanofullerene PCBM) were commercially obtained while the inorganic semiconductor, nanocrystalline ZnO:Al, was specifically synthesized for the particular experiments.

2.1 Methanofullerenes – PCBM

Soluble methanofullerenes (PCBM - [6,6]-Phenyl $C_{61/71}$ butyric acid methyl ester) have been suggested by J.C. Hummelen et al., for application as electron acceptor and n-conductor in organic bulk heterojunction solar cells [60]. This material is commercially available and is offered in various modifications: based on C_{60} or C_{70} and functionalized with single or multiple PBM-groups (mono-/multiadduct). The materials were purchased from Solenne B.V. (The Netherlands). Fig. 2.1(a) and 2.1(b) show the chemical formulae of [60]PCBM and [70]PCBM. Tab. 2.1 indicates the values of the HOMO and LUMO levels as reported in the literature.

In this thesis, PCBM-modifications were used as representative for molecular organic electron conductors, although there is also evidence for an amphoteric character of the charge conduction, i.e. PCBM exhibits n- and p-type properties simultaneously [6].
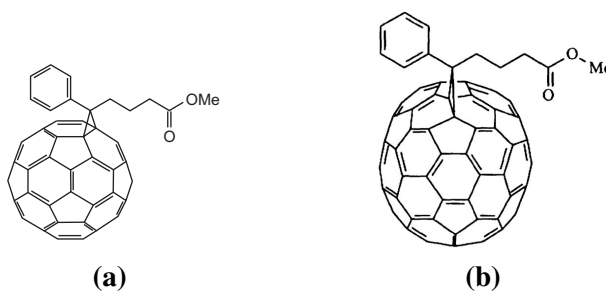

(a) **(b)**

Abbildung 2.1: Chemical formulae of the methanofullerenes [60]PCBM (a) and [70]PCBM (b)

2.2 Poly(3-Hexylthiophene 2,5-Diyl) – P3HT

Poly-alkyl-thiophenes (PAT) exhibit relatively high hole mobility ranging from $1 \cdot 10^{-5} \text{cm}^2 \text{V}^{-1} \text{s}^{-1}$ up to a quoted value of $1 \cdot 10^{-1} \text{cm}^2 \text{V}^{-1} \text{s}^{-1}$ [11, 67, 115] and a beneficial tendency to form ordered domains in annealed thin films [23]. During the past decades PATs have been extensively studied ragarding their optoelectronic properties and their application in electronic and photovoltaic devices. The chemistry of various conducting polythiohenes has been reviewed by Mc-

Coulough [79] and pioneering work on the charge transport was carried out by Bao *et al*. [11] and Sirringhaus *et al*. [115]. P3HT in the regioregular head-to-tail configuration, as shown in Fig. 2.2(a) is likely to align in a self-assembled conducting superstructure, in which the distance between the lamellae amounts to 3.6 Å (along the b-axis), while the distance between thiophene rings along the a-axis amounts to 1.6 nm [23, 61], as shown in Fig. 2.2(b). The HOMO and LUMO levels are indicated in Tab. 2.1. P3HT is generally found to be a p-conducting semiconductor; however, there is also evidence for electron conduction as reported in [26]. Regioregular P3HT was purchased at Rieke Metals.
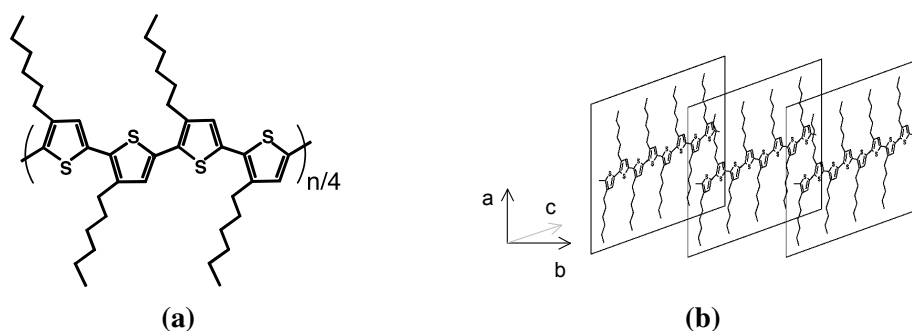

(a) (b)

Abbildung 2.2: (a) Chemical formula of regioregular P3HT. (b) Superstructure of aligned P3HT lamellae, redrawn from Ref. [114]

2.3 Nanocrystalline ZnO:Al – nc-ZnO:Al

Zinc oxide is a wide-bangap semiconductor with a direct energy bandgap of around 3.3 eV, hence ZnO is transparent for wavelengths in the visible range. ZnO is a II^b–VI compound semiconductor and crystallizes preferentially in the hexagonal Wurtzite structure as found by Bragg [19]. Under certain conditions the cubic zinc blende as well as the rock-salt structure have also been observed. II^b–VI semiconductors consist of an admixture of ionic and covalent binding character, while group IV element semiconductors like silicon exhibit completely covalent bonding. Zinc oxide in the Wurtzite structure has a polar hexagonal axis, the c-axis, chosen to be parallel to *z*. One zinc ion is tetrahedrally surrounded by four oxygen ions and *vice versa* [68]. The unit cell of ZnO is shown in Fig. 2.3. The valence band is formed by the occupied 2p-orbitals of O^{2-} or the binding sp^3 hybrid states while the lowest conduction band is formed by the empty 4s-states of Zn^{2+} or the antibinding sp^3-hybrid states. Hence, the direct overlap of the neighboring Zn-orbitals is rather large even in the amorphous phase [88]. Semiconducting zinc oxide nanocrystallites (nc-ZnO) and their optical, electrical and structural properties have been thoroughly investigated in past years [1, 73, 90, 100, 104, 107, 128]. The ability to synthesize nc-ZnO via the sol–gel technique makes this material an interesting choice for versatile applications in solution processed electronic devices such as transparent transistors [24] or hybrid organic–inorganic solar cells [16, 42, 43, 47].

After 60 years of extensive fundamental research, the bulk properties of zinc oxide are well known. It exhibits a high dielectric constant ε_{ZnO} of around 8 [72] and a high electron affinity [77], indicated in Tab. 2.1 as well as n- (and p-)dopability. Based on these advantageous bulk

properties, nanocrystalline ZnO was suggested as an alternative electron acceptor to PCBM in bulk heterojunction solar cells [16, 71] as well as an alternative n-conductor in hybrid ambipolar transitors (this work).

In contrast to bulk-ZnO the nanoparticular modification allows for alternative routes for thin film deposition. Quantum effects may show up due to substantial size reduction. Hence nanoparticular ZnO is of particular relevance for the realization of solution processed electronic devices.

For a wider range of applications, controlled doping of nc-ZnO by group-III or group-I elements is desired. However, doping nanocrystalline materials is not straightforward as the beneficial effect of doping might be compensated by the relatively large concentration of surface states. It has been shown by Orlinskii *et al*. [90] tha[...]ping of nanocrystalline ZnO is feasible. This concept is employed throughout thi[...] to alter the equilibrium carrier concentration in nanocrystalline ZnO-films. The[...]outes to synthesize Al-doped zinc oxide nanoparticles [73, 81, 104, 107, 128].
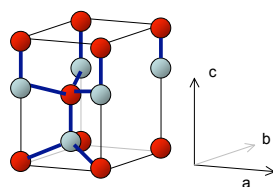

Abbildung 2.3: Unit cell of the Wurtzite crystal structure of ZnO. The red spheres represent oxygen, the blue spheres correspond to zinc. The primitive translation vectors a and b include an angle of 120° and are situated in the base plane, c is orthogonal to a and b.

The synthesis of nc-ZnO was performed according to the route introduced by Xue *et al*. [128]. 2-methoxyethanol (MTE), monoethanolamine (MEA), zinc acetate dihydrate (ZAD) and aluminium nitrate nonahydrate (ANN) were purchased from Sigma-Aldrich. The stabilizer MEA (2.1 ml) was dissolved in 100 ml of the solvent MTE to lead to a 0.35 M solution. The starting material ZAD (35 mmol) was added. Depending on the desired doping level ANN was admixed to the solution, whereas doping concentrations of up to 10 at% could be achieved. The solution was stirred for 2 h at 60°C and subsequently aged for at least one day. This yields a stable transparent solution, i.e. the solution is not saturated and no nc-ZnO precipitates.

Tabelle 2.1: HOMO and LUMO maxima of the organic semiconductors as determined from photoelectron spectroscopy [31, 45], conduction band minimum (CBM) of bulk ZnO as determined from field emission spectroscopy [77] and valence band maximum VBM.

	PCBM	P3HT		ZnO
LUMO	3.80	2.13	CBM	4.2
HOMO	5.80	4.65	VBM	7.5

3 Theoretical Background

The charge carrier mobility in disordered or nanocrystalline semiconductors is several orders of magnitude lower than in crystalline semiconductors. This must be attributed to the spatial and energetical disorder being present in these materials. Accordingly, these aspects have to be considered for an appropriate description of the charge transport in materials with substantially reduced order. The charge transport models relevant for the materials in this work will be summarized in the first part of the chapter. In this thesis field effect transistors based on the respective semiconductor materials were employed for the experimental consideration of the charge transport and its dependence on the carrier concentration. The second part of this chapter therefore presents the fundamental electrostatic description of accumulation/depletion regimes, which is of crucial relevance for determining the charge transport at high carrier densities in field effect transistor structures.

3.1 Transport Models

The charge carrier mobility μ is, to the first order, a measure of the drift velocity v_D in a given electric field F

$$\mu = \frac{v_D}{F}.$$ (3.1)

The underlying equation of motion $m^*\ddot{x} = m^*\dot{v}_D = qF$ with the collision time constant τ and the effective mass of the charge carrier m^* has the solution $m^*v_D = \tau qF$. This results in

$$\mu = \frac{q}{m^*}\tau.$$ (3.2)

Hence, the mobility is directly proportional to the relaxation time constant τ, similar to friction, i.e. it is limited by scattering. If these scattering events can be treated independently, Matthiessen's rule can be used to obtain the mobility as a function of different contributions μ_i [44]

$$\frac{1}{\mu} = \sum_i \frac{1}{\mu_i},$$ (3.3)

which implies, that the lowest mobility will dominate the charge transport. In the following, several charge transport models and its implications on the quantity μ will be discussed.

Crystalline Semiconductors

In crystalline semiconductors the periodic lattice approximation establishes a quasi-continuous extension of electronic wavefunctions. This results in the formation of broad energy bands implying negligible spacing of discrete energy levels. These energetically confined sets of bonding and antibonding orbitals refers to the valence and the conduction band, respectively, with an

energy gap of around 0.5 to 3.5 eV typical for crystalline semiconductors. At 0 K, the valence band is completely filled with electrons, leaving the conduction band completely empty. Hence, no carrier motion due to electric field gradients is possible. At finite temperatures, Fermi–Dirac statistics predict thermal excitation of a few electrons from the ground state into the conduction band, each leaving a hole in the valence band. These intrinsic carriers are considered to be quasi-free within the continuous energy bands. The density of states $D(E)$ of the respective energy bands is derived by assuming wavefunctions extended throughout the solid; the consideration is additionally restricted to only moderate doping levels. This consideration yields the parabolic approach, where $D(E)$ is a square–root function of energy E. The mobility in a three-dimensional crystalline semiconductor roughly ranges from ~ 10 cm^{2}V^{-1}s^{-1} to $\sim 10^4$cm^{2}V^{-1}s^{-1}. In crystalline materials the mobility is limited by scattering events, i.e. phonon scattering at high temperatures and impurity scattering at low temperatures [118]. Following Matthiessen's rule, these mechanisms can be treated independently, hence, the resulting mobility can be approximated by $\frac{1}{\mu} = \frac{1}{\mu_{phonon}} + \frac{1}{\mu_{impurity}}$. The suppression of impurity scattering by spatial separation of the free charge carriers from the dopants and, additionally, the suppression of phonon scatter events at low temperatures induce extremely high mobilities [4], up to the order of 10^7cm^2/Vs within a two dimensional electron gas [102].

3.1.1 Disordered Semiconductors

Solution processed organic semiconductors are likely to exhibit predominant amorphous character. The associated energetic and spatial disorder results in localization of the band states typically found in highly ordered materials. In the case of weak disorder, only the states close the band edge are localized. Increasing the degree of disorder enhances localization of the states deeper in the band until all states become localized. Transport of charge carriers is then considered to occur via hopping between interacting molecules [28].

The charge carriers taking part in transport are located in the HOMO [*] and the LUMO [†] level of the single molecules or monomers. The energy of these orbitals is statistically broadened within the molecular ensemble due to disorder induced by relative orientation, tilting etc. (see Fig. 3.1(a)).

The analysis of charge transport between localized sites requires the knowledge of the spatial and energetic position of each site. Since in this work, macroscopic quantities, such as the mobility and the conductivity are of concern, a sufficiently large number of sites is involved to justify a statistical approach to describe the transport. It is most common to describe the energy distribution in disordered semiconductor by a Gaussian distribution, as suggested by Bässler *et al.* [13], see Fig. 3.1. The density of states $D(E)$ for electrons in the LUMO and holes in the HOMO is then described by

$$D(E) = \frac{N}{\sqrt{2\pi}\sigma} \exp\left(-\frac{1}{2}\left(\frac{E - E_0}{\sigma}\right)^2\right). \tag{3.4}$$

Here, N is the density of molecular sites, facultatively multiplied by a factor which accounts for multiple redox sites, spin etc. σ is the width of the Gaussian density of states (DOS) and a

---

[*] highest occupied molecular orbital
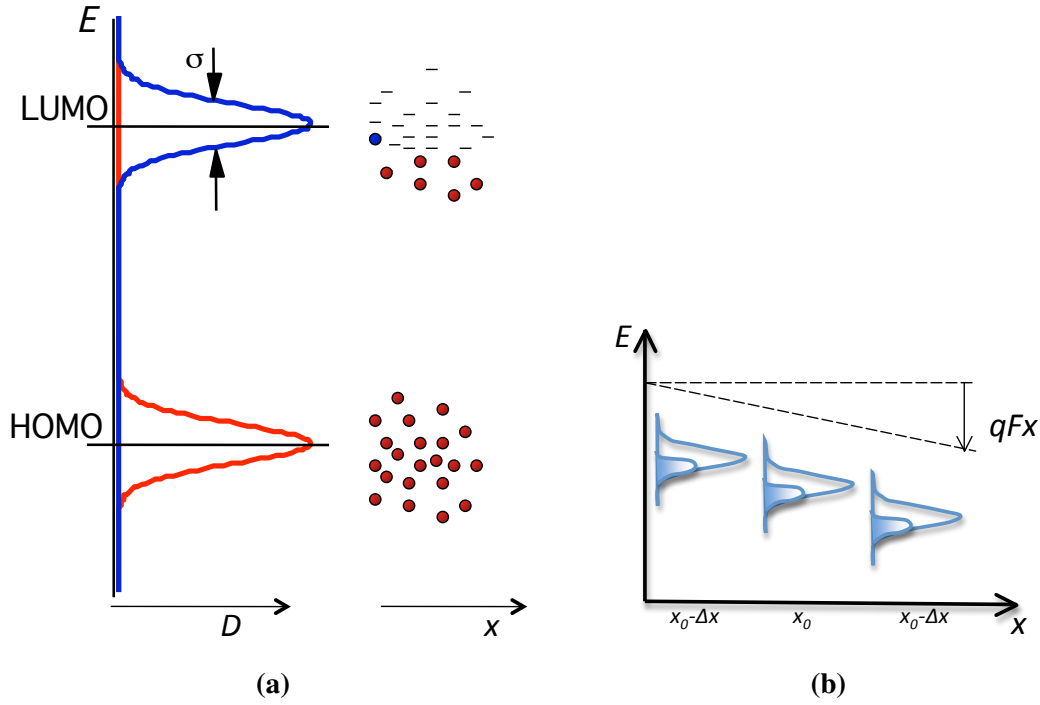[†] lowest unoccupied molecular orbital

Abbildung 3.1: Gaussian density of states. (a) The HOMO and the LUMO level of the single molecules or monomers is statistically broadened within the ensemble. The red dots represent occupied states. The tail states of the LUMO-DOS are partially filled in this picture due to an increased electron density. Charge carriers which occupy states close to the center of the LUMO-DOS (blue dot) find more next neighbors at similar energy and the mobility is expected to be higher then without electrons within the tail states. (b) Gaussian LUMO-DOS and density of occupied states (DOOS) at three different positions when applying an electric field. The mobility increases.

measure for energetic disorder, E is the energy and E_0 is the position of the maximum of the DOS.

For the thermodynamic formulation of state occupancy, it is not of interest whether the states are extended or not [93]. In the absence of an electric field, the electron n and hole p densities within the HOMO and LUMO, respectively, are determined by Fermi–Dirac statistics

$$n = \int_{-\infty}^{\infty} \frac{dE \cdot D(E - E_c)}{1 + \exp\left(-\frac{E - E_F}{k_B T}\right)} \quad \text{and} \tag{3.5}$$

$$p = \int_{-\infty}^{\infty} \frac{dE \cdot D(E_v - E)}{1 + \exp\left(-\frac{E_F - E}{k_B T}\right)}, \tag{3.6}$$

where E_c and E_v are the maximum of the HOMO and LUMO DOS, respectively. The density of occupied states (DOOS) within a specific energy interval $[\varepsilon_i, \varepsilon_j]$ can be derived from Eq. (3.6), by adjusting the integration boundaries. Hence, the DOOS(E) can be directly deduced.

In the following, the methods which contribute to the understanding of the mobility dependence on the charge carrier density in disordered semiconductors will be summarized, a more detailed description can be found in [120].

The charge carrier transport in disordered semiconductors is characterized by thermally activated tunneling between localized states. This model implies the coupling of the carriers to acoustic phonons. Mott [85] considered thermally activated tunneling between localized states within a uniform DOS and found the famous temperature dependence for the conductivity in a three-dimensional system $\sigma \propto \exp(T^{-1/4})$.

Gaussian Disorder Model

Bässler *et al.* suggested a Gaussian distribution of energy states (see Fig. 3.1(a)) for the description of the landscape of electronic levels in organic materials, which led to the Gaussian disorder model (GDM) [12, 13, 123]. This model is based on a previous concept on transfer rate equations by Miller and Abrahams [83].

The following suggestions lead to the rate equation for the charge transport in disordered systems (note that the formalisms are shown for the case of electrons, but they can be easily transferred to the world of holes as well): Outgoing from an electron localized at a site energy ε_i, one has to consider two options for the charge carrier to occupy an adjacent state: At time t the occupation probability p_i of a localized site i with high energy is low, while the transition rate W_{ij} to sites lower in energy is high. However, a low energy site has a high probability of being occupied, while the respective transition rate is low. When considering stationary solutions and neglecting recombination, the sum over the product of occupation probabilities of the system and the transition rates has to be equal to the sum over the reverse processes,

$$\frac{\partial p_i(t)}{\partial t} = \sum_{j \neq i} [-W_{ij} p_i (1 - p_j) + W_{ji} p_j (1 - p_i)] = 0 \qquad (3.7)$$

Equation 3.7 is the so-called (stationary) Master-equation. p_i (p_j) is the probability that site i (site j) is occupied and W_{ij} is the transition rate from site i to j and *vice versa*. The factor $(1 - p)$ ensures that double–occupancy of a site is prohibited, which qualitatively accounts for the Pauli-principle.

The transition rate is calculated from the spatial distance R_{ij}=|$\mathbf{R}_j$-$\mathbf{R}_i$| between the sites and the respective energy difference (ε_j - ε_i) [2]:

$$W_{ij} = \nu_0 \exp \left(-2\alpha R_{ij} - \frac{1}{2k_B T} \left(|\varepsilon_j - \varepsilon_i| + \varepsilon_j - \varepsilon_i \right) \right) \qquad (3.8)$$

ν_0 is the attempt-to-escape frequency which depends on the electron–phonon coupling strength, the phonon density of states, and other properties of the material [2, 27]. α is the inverse localization length of the wave function (order of 10/a, with a: lattice constant). The factor exp(-2R_{ij}) is proportional to the transfer integral between the two sites, and determines the tunneling probability between sites with equal energies. Upward hopping demands the supply of energy, here thermal, while for downward hopping, no restriction to the supplied energy is made and the right argument in the exponent in Eq. (3.8) is set to unity. Applying an electric field, $\varepsilon_j - \varepsilon_i$ in the above notation is replaced by $\varepsilon_j - \varepsilon_i + e(\mathbf{R}_j - \mathbf{R}_i))\mathbf{F}$. In the Monte-Carlo approach by Bässler *et al.* [13], the carrier, treated as a particle, propagates, subject to the Miller–Abrahams transition rates Eq. (3.8), on a grid consisting of states with Gaussian distributed energies. When convergenece is reached, Eq. (3.7) is fulfilled. Accordingly, the following expression for the mobility in dependence of the electric field, disorder and temperature was found by Bässler [13]:

$$\mu = \mu_0 \exp\left(-\left(\frac{2}{3}\hat{\sigma}\right)^2 + C\left(\hat{\sigma} - \Sigma^2\right)\sqrt{F}\right) \quad \Sigma > 1.5,$$

$$\mu = \mu_0 \exp\left(-\left(\frac{2}{3}\hat{\sigma}\right)^2 + C\left(\hat{\sigma} - 2.25\right)\sqrt{F}\right) \quad \Sigma < 1.5, \tag{3.9}$$

with μ_0 the mobility in the high temperature limit, $\hat{\sigma} = \frac{\sigma}{k_B T}$, C=3·10^{-4} (cm·V)$^{\frac{1}{2}}$. Σ is a parameter which reflects the spatial disorder of the semiconductor matrix. Most commonly, the $\mu(F)$ dependence is denominated Poole–Frenkel-like behavior which agrees with the experimentally found empirical relation [41]

$$\mu \propto \exp\left(\gamma\sqrt{F}\right). \tag{3.10}$$

Here, γ is a factor which accounts for the strength of the field dependence. This variation of μ with the electric field strength can be explained in the framework of the GDM: An applied bias lowers the energy barriers of the sites along the field gradient [13, 83]. The DOS and the DOOS at three different space coordinates $x \pm \Delta x$ along the field gradient are shown in Figure 3.1(b) in order to illustrate this issue.

Bässler *et al.* also showed a Gaussian–type temperature dependence, employing hopping conduction within a Gaussian DOS (see Eq. (3.9)). Usually the left part of the equation, i.e.

$$\mu \propto \exp\left(-\left(\frac{2}{3}\hat{\sigma}\right)^2\right) \tag{3.11}$$

is used for interpreting experimental data at low electric field strengths.

By temperature dependent measurements of the mobility, the width of the Gaussian DOS, σ, can be determined quantitatively. It should be noted that, when the deep levels of the DOS are filled, it is also possible to approximate exponential dependence of μ on T to fit the experimental data. Since it should be possible to consistently describe one material system by one single model, also in different devices, e.g. diodes, which are usually described by the Gaussian disorder model, and field effect transistors, the Gaussian model is better suited [119].

Investigations of the charge carrier dependence of the mobility require an experimental approach in which the (intrinsic) carrier concentration can be altered by orders of magnitude. This can be achieved via accumulation of charge carriers at the gate dielectric of field effect transistors. However, the Bässler model [13] does not describe the charge transport at high carrier densities. Several methods have been suggested to describe the density dependence of the mobility. A comprehensive study of six different models on this issue can be found in Ref. [27]. A benchmark was set by a model employing the Master equation approach by Pasveer *et al.* [99]. The Master equation approach (ME), qualitatively compares to the Monte–Carlo approach (MC) and complies with Eq. (3.7) and Eq. (3.8) but the calculation procedure is different from MC. The basic approach of ME employs the occupation probability instead of considering particles as in MC, but leads to similar results. A more detailed comparison of Monte–Carlo and the Master equation approach is presented in Ref. [132].

In Ref. [99] Eq. (3.7) was solved with Miller–Abrahams transition rates as in Eq. (3.8) with the localization length α set to 10/a. Then, the mobility was calculated from $\mu = \sum_{ij} W_{ij} p_i (1 -$

$p_j)R_{ijx}/pFA^3$, where x is the field direction, $R_{ij,x}=(\mathbf{R}_j\text{-}\mathbf{R}_i)\cdot x$, $p = \langle p_i \rangle a^{-3}$ and A^3 is the system volume. By executing the approach for a wide range of electric fields and carrier densities, a unified description of the charge transport in the framework of the extended GDM was established. The parameterization and its consequences will be discussed in the following. $\mu(T,n)$ with an exemplarily chosen parameter set as indicated by the legend is shown in Fig. 3.2(a). In the high temperature limit, i.e., when $2k_BT \gg \sigma$, the energy difference between initial and final state $\varepsilon_i - \varepsilon_j$ is not expected to limit the transport, and Eq. (3.8) reduces to $\nu_0 \exp(-2\alpha R_{ij})$, independent of charge carrier density and field (Fig. 3.2(a), upper dotted line). This circumstance is represented by a temperature independent prefactor $c_1 \approx \exp(-2\alpha a) \approx 1.8\cdot 10^{-9}$ and by a mobility prefactor μ_0, independent of α

$$\mu_0 \equiv \frac{a^2 \nu_0 e}{\sigma},$$

The temperature dependence of the mobility in the low density and low field regime as derived from the ME–approach reflects the relation found by Bässler, written in Eq. (3.11):

$$\mu_0(T) = \mu_0 c_1 \exp\left(-0.42\hat{\sigma}^2\right). \tag{3.12}$$

The arrows towards the *ordinata* in Fig 3.2(a) indicate $\mu_0(T)$ at three different temperatures. Further, the carrier density dependence of the mobility was parameterized to

$$\mu(T,n) = \mu_0(T)\exp\left(\frac{1}{2}(\hat{\sigma}^2 - \hat{\sigma})\left(2na^3\right)^{\delta}\right), \tag{3.13}$$

where δ, again depends on the degree of disorder.

$$\delta \equiv 2\frac{\ln\left(\hat{\sigma}^2 - \hat{\sigma}\right) - \ln\left(\ln 4\right)}{\hat{\sigma}^2}. \tag{3.14}$$

At low carrier densities, the mobility was found to be almost constant. This is due to the fact that at low carrier densities, the density of occupied states (DOOS) does not change its shape but only the size [27]. At high densities, the low energy states are occupied and the mobility increase scales with $\exp(n^{\delta})$. δ again is dependent on temperature and disorder, and the increase becomes more pronounced at low temperatures. The reason for the latter is, that the carrier finds more adjacent sites of similar energy when the deep states are filled due to the increased charge carrier density, see Fig. 3.1(a). The effect on the hopping probability is larger at low temperatures when the thermally supplied energy is low.

The observation of increasing mobility can be written in compact form as:

$$\mu(T,n) = \mu_0(\sigma,T) \cdot \exp(u(\sigma,T)(2na^3)^{\delta}), \tag{3.15}$$

with $u(\sigma,T) = \exp\left(\frac{1}{2}(\hat{\sigma}^2 - \hat{\sigma})\right)$. It should be noted that the model fails at charge carrier densities higher than $a^{-3}/2$, indicated by the crossing point of $\mu(T,n)$ of various temperatures, observed in Fig. 3.2(a), due to electron–hole symmetry, i.e. at charge carrier densities higher than $10^{20}\cdot\text{cm}^{-3}$.
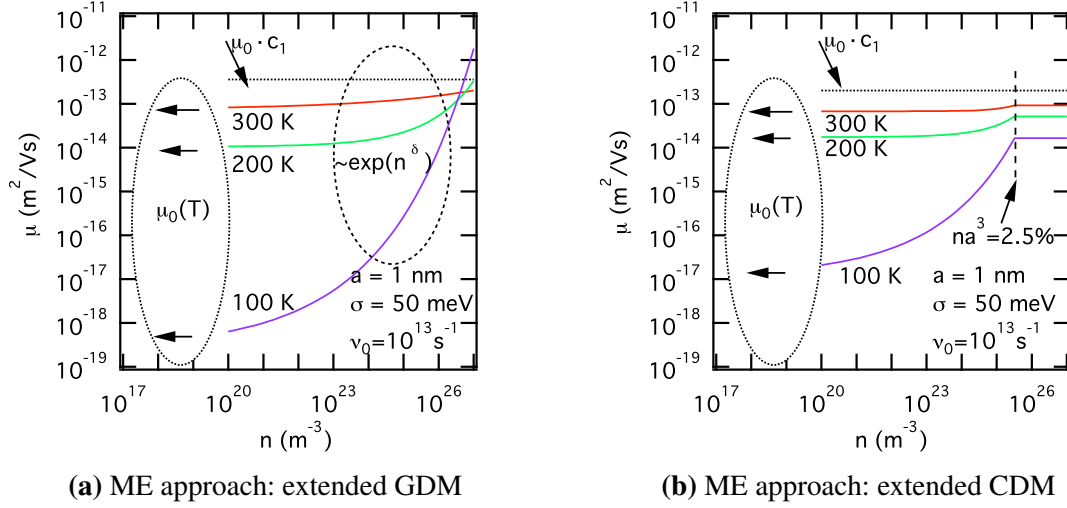
(a) ME approach: extended GDM

(b) ME approach: extended CDM

Abbildung 3.2: The mobility as a function of the charge carrier density derived from the Master equation approach. a) Parameterization by Pasveer *et al.* (Eq. (3.13)) b) Parameterization by Bouhassoune *et al.* (Eq.(3.20, 3.22)) for a given parameter set as indicated by the legend and in the text. The prefactor $c_1\mu_0$ indicates the high–temperature limit for the mobility, as indicated by the upper dotted line in (a) and (b). The temperature dependent low carrier density limit of the mobility $\mu_0(T)$ as expressed by Eq. (3.12,3.19) is indicated by the arrows towards the *ordinata*. Due to energy correlation of states, the temeperature dependence in (b) is less pronounced. The increase of μ is governed by $\exp(n^\delta)$ in both cases (not indicated in (b) to preserve clarity) as expressed by Eq. (3.13,3.20). In the CDM, the mobility saturates at densities exceeding 2.5% of the total site density, as stated in Eq. (3.22).

Additionally, the field dependence of the mobility is accounted for by an approximately carrier density independent prefactor f(T,E), so that $\mu(T,n,F) \approx \mu(T,n) \cdot f(T,F)$.

$$f(T,E) = \exp\left(0.44(\hat{\sigma}^{\frac{3}{2}} - 2.2)\left(\sqrt{1 + 0.8\left(\frac{Fqa}{\sigma}\right)^2} - 1\right)\right) \qquad (3.16)$$

The ME approach of hopping within a Gaussian DOS leads to the dependence of the mobility on the charge carrier density at various temperatures by taking into account randomly distributed site energies. Coulomb interaction was taken into account by prohibiting double occupancy of sites. Note that long-range Coulomb interactions, as investigated with MC in Ref. [75] and [33], have a negative impact on the mobility at high charge carrier densities, as the energy difference $\varepsilon_i - \varepsilon_j$ is likely to be further enhanced by the Coulomb repulsion of adjacent charge carriers.

Correlated Disorder Model (CDM)

The CDM is a variation of the GDM, with the modification that the energies of adjacent sites are correlated [89]. In this model it is assumed that the energies of the localized sites are not strictly statistically distributed but the electronic states under consideration are surrounded by sites of similar energies. This scenario takes into account, e.g. similar site energies along a particular polymer chain or site energy alignment due to dipole–dipole interaction. In the latter case, the

energy of one site is the result of a distribution of independently and randomly oriented surrounding dipole moments at each lattice site. This procedure leads to a distribution of energies which is to a good approximation a Gaussian density of states [130]. The energy of a carrier at site i is then given by

$$\varepsilon_i = -\sum_{j \neq i} \frac{q\mathbf{d}_j(\mathbf{R}_j - \mathbf{R}_i)}{\varepsilon_{sc}|\mathbf{R}_j - \mathbf{R}_i|^3},$$

(3.17)

where $q\mathbf{d}_j$ is the dipole moment of site j at distance $|\mathbf{R}_j\text{-}\mathbf{R}_i|$ from site i. ε_{sc} is the dielectric constant of the semiconductor. The resulting width of the Gaussian DOS is $\sigma_d = \frac{2.35ed}{\varepsilon_{sc}a^2}$ [130]. Note that, apart from dipoles, long–range thermal fluctuations in the molecular geometries of a polymer were suggested as a possible cause for correlation within the disordered ensemble [132].

The lattice of sites correlated in energy due to dipole–dipole interactions together with the rate equations Eq. (3.8) were used for the derivation of the mobility using the Monte-Carlo approach in Ref. [89]

$$\mu = \mu_0 \exp\left(-\left(\frac{3}{5}\hat{\sigma}_d\right)^2 + C_0\left(\hat{\sigma}_d^{3/2} - \Gamma^2\right)\sqrt{\frac{qaF}{\sigma_d}}\right).$$

(3.18)

In Eq. (3.18) C_0=0.78 and Γ were found to amount to 2. The meaning of Γ can be compared to that of Σ in Eq. (3.9) and is a factor that characterizes geometrical disorder.

In the model recently published by Bouhassoune *et al.* [18], the mobility dependence on the charge carrier density has been described in an extended correlated Gaussian disorder model, using the Master equation approach. Assuming correlated states, the interdependence of the mobility and the charge carrier density is less pronounced than in the model by Pasveer *et al.* [99]. In the framework of the extended CDM, the parameterization is modified as discussed in the following. Fig. 3.2(b) illustrates the dependence of the mobility on the charge carrier density for three different temperatures and an exemplarily chosen parameter set, as indicated by the legend. The temperature-independent prefactors $\mu_0 = \frac{a^2\nu_0}{\sigma}$ and c_1 are determined by the same suggestions as discussed for the above extended GDM model. However, the temperature dependence at low field and low carrier density is less pronounced, as indicated by the arrows towards the *ordinata* in Fig. 3.2(b). Nevertheless, adequate agreement with the temperature dependence of the mobility found employing the MC approach within the framework of CDM (see Eq. (3.18)) is achieved,

$$\mu_0(T) = \mu_0 c_1 \exp\left(-0.29\hat{\sigma}^2\right).$$

(3.19)

Below 2.5% fill factor of the site volume, the increase of μ is determined by $\exp(n^\delta)$ as in Eq. (3.13) and

$$\mu(T,n) = \mu_0(T) \cdot \exp\left(\left(-0.25\hat{\sigma}^2 + 0.7\hat{\sigma}\right) \cdot \left(2na^3\right)^\delta\right).$$

(3.20)

$$\text{for} \quad na^3 < 0.025$$

$$\delta \equiv 2.3 \frac{\ln\left(0.5\hat{\sigma}^2 + 1.4\hat{\sigma}\right) - 0.327}{\hat{\sigma}^2}$$

(3.21)

The energetic correlation of states generates domains of similar energy. Due to the increase of the charge carrier density the states within domains of low energy become occupied. Hence, the net charge flow through these domains is impeded or even totally suppressed, which results in mobility saturation and the mobility remains at a constant value

$$\mu(T,n) = \mu(T, 0.025a) \quad \text{for} \quad na^3 \geq 0.025. \tag{3.22}$$

It should be noted that a slight decrease of μ at high n was found by Bouhassoune *et al.*, although the authors mention, that long range Coulomb interactions and transitions more than $\sqrt{3}a$ were not taken into account.

In this approach, the field dependence is expressed by a prefactor $f(n,T,F)$ (compare to Eq. (3.16)) which is dependent on the charge carrier density, and its expression varies with the field strength. To be more precise, in the low carrier density regime the mobility dependence on the electric field is enhanced due to the decrease of the energy difference between adjacent sites induced by the electric field. However, these valley-like structures of low energy sites get filled at high charge carrier densities and consequently the field dependence of the mobility decreases. Therefore, the impact of f will not be enhanced at high n and not be discussed in detail, here.

The inclusion of correlations between the site energies seems to be a reasonable correction for the physical description of the disorder. Another assumption, which has been made in the models above is the validity of the transition rate expression. One has to bear in mind that by applying Miller–Abrahams transition rates Eq (3.8), it was assumed that forming of polarons, i.e. polarizations and deformations of the lattice induced by the charge carrier, is negligible. However, the excess energy from downward hopping is efficiently coupled to phonons, i.e. lattice vibrations [13, 105]. Further, it is assumed that the relaxation of the site configuration can be neglected. The Marcus theory [76], however, involves the latter point, here, the energy of an occupied site differs from the energy of an unoccupied state. The transition rate W_{ij} described within the framework of the Marcus theory is[‡]

$$W_{ij} = W_0 \exp\left(-\frac{E_a}{k_B T}\right) \tag{3.23}$$

$$W_0 = \frac{J_{ij}}{\hbar} \sqrt{\frac{\pi}{4E_a k_B T}}. \tag{3.24}$$

E_a is the polaron activation energy, J_{ij} is the overlap integral given by $J_{ij}^2 = J_0^2 \exp\left(-2\alpha R_{ij}\right)$, $\hbar$ is the reduced Planck constant. In order to preserve clarity, the simplified version of the exact Marcus jump rate has been chosen in Eq. (3.24). It considers only linear terms within the exponent. Eq. (3.24) is appropriate when $E_a \gg \sigma$ [37, 38]. By employing numerical methods, it is possible to arrive at an expression for the mobility, whether Miller–Abrahams or Marcus transistion rates, correlated or uncorrelated states are taken into account. The hopping processes are simulated with, e.g., Monte-Carlo or Master equation approach. Nevertheless, the simulations are governed by enormous computing time and only lead to parametric, not analytic solutions. Hence, analytical or semi-analytical approaches, which lead to useful results or useful and acceptable approximations have been suugested.

[‡]The complete expression for polaron transition rates is given by $W_{ij} = W_0 \exp\left(-\frac{E_a}{k_B T} - \left(\frac{1}{2k_B T}\left(\varepsilon_j - \varepsilon_i\right)\right) - \left(\frac{1}{8k_B T E_a}\left(\varepsilon_j - \varepsilon_i\right)^2\right)\right)$

Multiple trapping and release

Alternatively to the calculation of the charge transport via the Master equation of the VRH, one can also assume quasi–continuous band transport which is influenced by traps. Charge carriers can be activated from lower energies to the transport energy, the energy of most probable jumps. Charge carriers with energies higher than this transport energy contribute to the charge carrier transport [7, 12]. The quasi-free charge carriers can be trapped in sites below the transport energy and released by thermal activation. Carrier transport below the transport energy is, however, neglected. This model allows for a macroscopic description of the charge carrier transport via the Poisson- and current-equation.

There exist several other methods which aim on describing the charge transport at high charge carrier densities in a Gaussian DOS semi-analytically. Their applicability is reviewed in Ref. [27].

3.1.2 Nanocrystalline Semiconductors

So far, disordered semiconductors, in which the carrier wave function become completely localized, were in the focus. In contrast, nanocrystalline materials close the gap between strict localization on the atomic length scale and extension of electron wavefunction on the macro-molecular scale within the nanometer range. The model describing the grain barrier limited transport convincingly was originally developed by Seto [108] for polycrystalline Silicon (poly-Si). The theory was later generalized for polycrystalline semiconductors over a wide range of doping densities and grain sizes [121]. A review article on charge transport in polycrystalline ZnO and ITO can be found in [35]. The Seto model assumes, that the band structure of the single crystalline material is applicable within the nanocrystallite as there is short range lattice periodicity. However, one must assume the surface of the nanocrystallites to be characterized by disorder as there will be a high density of unsaturated bonds, adsorbates and deviations of bond lengths and angles between the host atoms. These defects may trap charge carriers and become charged while the net free carrier density decreases. The resulting alteration of the surface energy establishes a barrier which charge carriers have to overcome (by thermal activation) when being transported from one crystallite to the next. Accordingly, this barrier has to enter the transport models in terms of an activation energy ΔE.

Simplified model

A sketch of the simplified picture of crystallites, energy band diagram and charge carrier density is provided in Fig. 3.3. The following assumptions, first developed in a model by Seto [108], lead to an analytical approximation which is capable of describing the effect of doping and grain size on the activation energy and the macroscopic mobility in nanocrystalline thin films:

- a composition of identical crystallites with a grain size L_{nc} (Fig. 3.3(a)),

- applicability of the band structure of the pure and infinite crystal within the crystallite,

- negligible thickness of the grain boundary with a surface defect density Q_t of monoenergetic traps at the energy E_t (also models for Gaussian shape exist [57]),

- neutral traps at the boundary which are charged by trapping the free charge carrier (Fig. 3.3b,c). The existence of double charged defects is neglected as well as the possibility that donor atoms segregate to the interface [121].

- impurity atoms (doping centers) with density N_D are completely ionized

- negligibility of tunneling through the barrier.

Further, it is assumed that the depletion of the carriers within the crystallite starts abruptly at l (Fig. 3.3(c), the distance of the abrupt space charge from the center of the grain. Based on these assumptions the Poisson equation becomes

$$\frac{\partial^2 \Phi}{\partial x^2} = \frac{qN_D}{\varepsilon \varepsilon_0} \qquad\qquad l < x < L_{nc}/2, \qquad (3.25)$$

where Φ is the potential at distance x from the grain center, q is the elementary charge, ε is the dielectric constant of the semiconductor, L_{nc} is the linear expansion of one grain. The integration with the boundary condition $\frac{d\Phi}{dx}=0$ at l and $\Phi(x)$ is continuous and leads to

$$(3.26)$$

$$\Phi(x) = \frac{qN_D}{2\varepsilon\varepsilon_0}(x-l)^2 + \Phi_0. \qquad (3.27)$$

Φ_0 is the potential directly at the grain boundary surface. If $LN_D < Q_t$, the crystallite becomes fully depleted and with $l=0$ Eq. (3.27) becomes

$$\Phi(x) = \frac{qN_D}{2\varepsilon\varepsilon_0}x^2 + \Phi_0. \qquad (3.28)$$

The barrier height ΔE is the difference between $\Phi(0)$ and $\Phi(L/2)$

$$\Delta E = \frac{qN_D L^2}{8\varepsilon\varepsilon_0} \qquad (3.29)$$

If $LN_D > Q_t$, Eq. (3.28) and consequently $l > 0$ the barrier height becomes

$$\Delta E = \frac{qQ_t^2}{8\varepsilon\varepsilon_0 N_D}. \qquad (3.30)$$

Hence, at small doping density, ΔE linearly increases with N_D (Eq. (3.29)), while at higher doping density there is a decrease proportional to $1/N_D$ (Eq. (3.30)). To account for the energy barrier in nanocrystalline films the mobility, as a consequence from Matthiessens rule (Eq. (3.3)), is limited by thermal activation.

The thermionic emission current density j_{th} across the boundary at applied bias V_{appl} is given by Ref. [3, 22, 108] by

$$j_{th} = qn_{av}\sqrt{\frac{k_B T}{2m^*\pi}}\exp\left(-\frac{\Delta E}{k_B T}\right)\left(\exp\left(\frac{qV_{appl}}{k_B T}\right) - 1\right), \qquad (3.31)$$

where n_{av} is the average free electron density within the crystallite. If the applied voltage at a single barrier is smaller than $k_B T$, $\exp\left(\frac{qV_{appl}}{k_B T}\right)$ can be expanded to $1+\frac{qV_{appl}}{k_B T}$ and Eq. (3.31) becomes

$$j_{th} = q^2 n_{av} \sqrt{\frac{1}{2m^*\pi k_B T}} \exp\left(-\frac{\Delta E}{k_B T}\right) V_{appl}. \tag{3.32}$$

It should be noted, that the thermionic emission over isotype heterojunctions is somewhat different to the behavior at metal/semiconductor contacts, where $j_{th,me/sc} \propto T^2 \exp\left(-\frac{\Delta E}{k_B T}\right)$ [22, 118]. From $j = \sigma\frac{V_{appl}}{L_{nc}}$, the conductivity can easily be calculated

$$\sigma = L_{nc} q^2 n_{av} \sqrt{\frac{1}{2m^*\pi k_B T}} \exp\left(-\frac{\Delta E}{k_B T}\right). \tag{3.33}$$

This leads to an expression for the mobility, using $\sigma = q n_{av}\mu$

$$\mu = \mu_0 \exp\left(-\frac{\Delta E}{k_B T}\right) \tag{3.34}$$

with $\mu_0 = \nu_0 \cdot T^{-\frac{1}{2}}$ and $\nu_0 = qL_{nc}(2\pi m^* k_B)^{-1/2}$. It is worth noting here that by supposing the mean free path of the electrons to be equal to l which demands a sufficiently high bulk mobility, the prefactor μ_0 can be easily estimated from the mean thermal velocity v_{th}. For the random motion across a plane with Maxwellian distribution of velocities, v_{th} is given by

$$v_{th} = \sqrt{\frac{8k_B T}{\pi m^*}}, \qquad L = v_{th}\tau, \tag{3.35}$$

from which it follows that

$$\mu_0 = \frac{q\tau}{m^*} = \frac{qL}{\sqrt{8/\pi \cdot m^* k_B T}} \tag{3.36}$$

which differs only by a small factor from μ_0 in Eq. (3.34). Hence, if ΔE is negligible, the mobility is limited by scattering at the grain boundary.

$$\tag{3.37}$$

Charge carrier density variation

The charge carrier density can be modulated via accumulation and also via doping.

Accumulation   In a nanocrystalline semiconductor, accumulation of charge carriers at a given interface leads to spatially confined enhancement of the carrier density. This lowers the interface barriers heights [57, 58] as shown in Fig. 3.3(d).
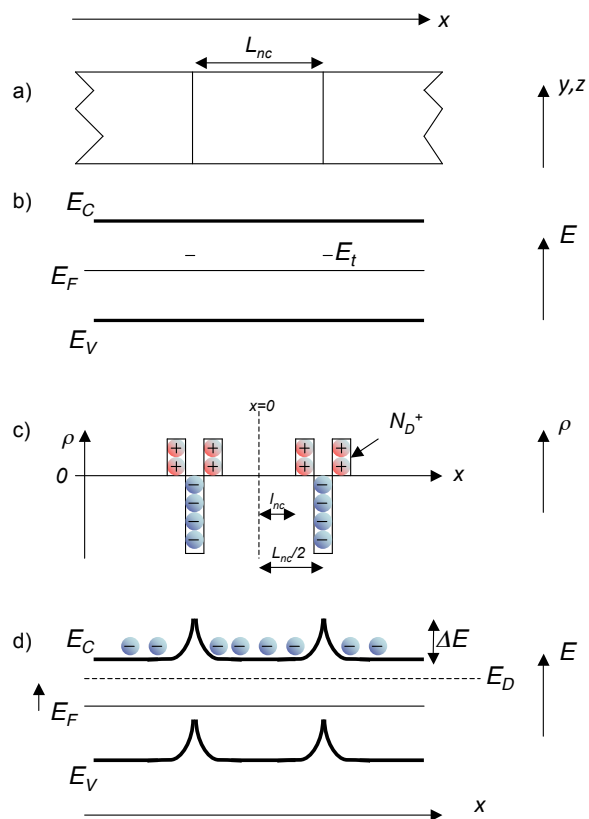
Abbildung 3.3: Model scheme of the aligned semiconductor nanocrystallites including the surface barrier between the sites: a) schematic of the idealized model, b) energy bands including surface states (without doping centers) c) Charge carrier density *vs.* space coordinate d) Band–like transport within the crystal is assumed, perturbed by a double Schottky barrier at the grain boundary.

Doping   The charge carrier density in semiconductors can by modulated as well by the addition of dopants. The dopants can be thermally ionized, leaving a charged impurity in the energy gap and an additional free charge carrier in the conduction or valence band. As in the case of accumulation of charge carriers, doping results in the lowering of the activation energy, but here, the spatially fixed space charge of the dopant serves as an additional scattering center for free charge carriers. As a result, the mobility within the bulk crystal can be diminished due to the reduction of the mean free path (see Eq. (3.36)).

Injection   Increasing the applied field increases V_{appl} in Eq. (3.31) and also the charge carrier density at x. If Boltzmann statistics can be applied, $n(x) = N_c * \exp((qV(x) - E_f)/k_B T)$. Hence, in this case, the activation energy will be effectively lowered.

3.2 Fundamental description of the charge carrier density modulation under applied bias

In the previous section the most common models for the charge transport in disordered and nanocystalline semiconductors were depicted. This section provides the theoretical background, necessary to understand the fundamental characteristics of field effect transistors in general which served as experimental tool for investigation of the carrier density dependence of the mobility in the respective semiconductors.

The space charge at the semiconductor–insulator interface In a field effect transistor, the space charge Q per unit area A, i.e. Q_i, is derived from the capacitance per unit area C_i and the gate Voltage V_g between the gate and the source electrode using

$$Q_i = \frac{Q}{A} = \frac{\varepsilon_{sc}\varepsilon_0}{d} \cdot V_g. \tag{3.38}$$

Q_i is a two dimensional quantity, but the charge transport is a function of the three-dimensional charge carrier density (p_{acc} and n_{acc} for holes and electrons, respectively) in a volume $V_{\text{Vol.}}$. p_{acc} and n_{acc} can be approximated, assuming an accumulation depth. To the first order, one can expect that charge carrier accumulation takes place only within the first monolayers with the thickness d_{acc} of the semiconductor, i.e. in this approach it is assumed that the surface charge is the projection of the volume charge onto one monolayer:

$$\frac{Q}{V_{\text{Vol.}}} = \frac{\varepsilon_{sc}\varepsilon_0}{d_{ins}d_{acc}} \cdot V_g \quad \text{and} \quad n_{acc} = \frac{Q}{V_{\text{Vol.}} \cdot q}. \tag{3.39}$$

For the special case of classical band structures and the applicability of the Boltzmann approximation, the spatial distribution of the charge carrier density as a function of the distance to the dielectric has been derived in Ref. [119]. The procedure follows the derivation of the charge carrier density within an ideal MIS diode (see e.g. Ref. [118]). For this special case, Eq. (3.39) has been shown to be a good approximation for the three-dimensional charge carrier density at the interface. The charge carrier density is attenuated by a factor of $1/e$ at a distance to the insulator interface of less then 2 nm [119].

Nevertheless, as the mobility strongly depends on the charge carrier density, it is necessary to find an exact expression for the volumetric charge density *vs.* gate voltage. For disordered semiconductors, however, the charge carrier density *vs.* V_g has to be found numerically due to the shape of the density of states.

The charge carrier density within the sample is the sum over the number of free electrons and holes as well as ionized donors or acceptors.

$$\rho = -q(n - p + N_A^- - N_D^+) \tag{3.40}$$

In the bulk, i.e. far from the dielectric/semiconductor interface, where the charge neutrality condition applies, the density of trap states can be derived from

$$p - n = -N_A^- + N_D^+ \tag{3.41}$$
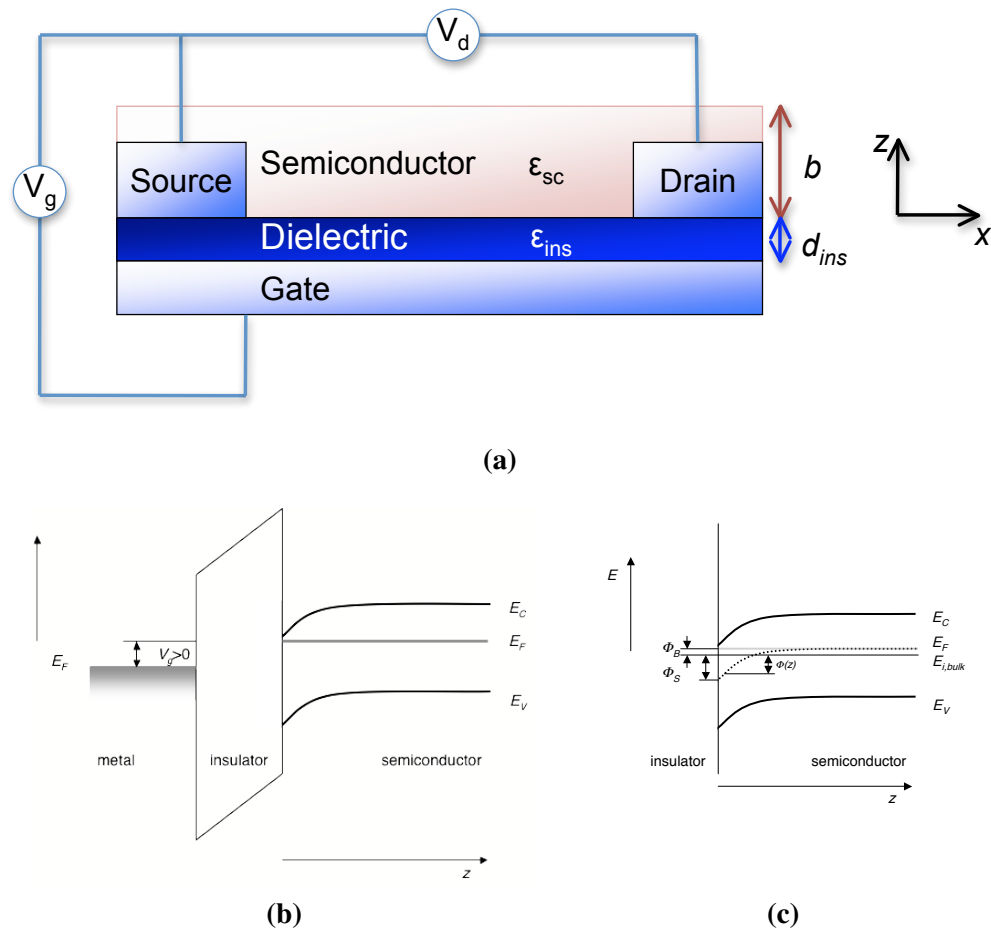
(a)

(b)

(c)

Abbildung 3.4: Field effect transistor: (a) Cross-sectional scheme of a field effect transistor illustrating the applied voltages V_d between source and drain and V_g between source and gate, respectively, as well as the x and z-axis, the thickness b of the semiconductor with dielectric constant ε_{sc}, the thickness d_{ins} of the semiconductor with dielectric constant ε_{ins}. (b) Band bending at the semiconductor–insulator interface due to an applied positive gate voltage. (c) Surface potential Φ_s, bulk potential Φ_b and potential $\Phi(z)$ measured relative to the intrinsic Fermi level in the bulk $E_{i,bulk}$.

The electric field normal to the dielectric $F_z = \partial\Phi/\partial z$ at distance z from the dielectric can be derived using the Poisson equation

$$\frac{\partial^2\Phi}{\partial z^2} = \frac{\rho}{\varepsilon_{sc}\varepsilon_0}. \tag{3.42}$$

The intrinsic Fermi level in the bulk of the semiconductor $E_{i,bulk}$ was chosen as the reference energy ($E_{i,bulk} \equiv 0$).

The following boundary conditions illustrated in Fig. 3.4(c) with

- $\partial\Phi/\partial z = 0$ at $z = b$ with b being the thickness of the device (Note that this condition is especially important when considering measurements of the electron affinity at varying thicknesses of the semiconductor in order to investigate the band alignment at an interface, as the alignment will always occur in a way, that this condition is fulfilled [93].)

- $\partial\Phi/\partial z = F_s$ at $z = 0$ for the left side of equation (3.42).

- The electron potential energy $\Phi(z)$ at $z = 0$ is $\Phi(0) = \Phi_s$ and

- $\Phi(b) = \Phi_b$ with Φ_b as the bulk potential for the right side.

lead to

$$\int_0^{F_z} \frac{\partial\Phi}{\partial z} d\frac{\partial\Phi}{\partial z} = \int_{\Phi_b}^{\Phi(z)} \frac{\rho}{\varepsilon_{sc}\varepsilon_0} d\Phi. \tag{3.43}$$

The Gauss-Fermi integral (Eq. (3.6)) is solved for electrons and holes starting from $\Phi(z)$ (see Fig. 3.4(c) for illustration) as the input parameter. The band bending is determined by $\Phi(z)$, so that $E_c \rightarrow E_c + \Phi(z)$ and $E_v \rightarrow E_v + \Phi(z)$. The resulting ρ for different $\Phi(z)$ is then used for the integration of Eq. (3.43) from Φ_b to $\Phi(z)$ (and Φ_s). This gives an expression for $F(z)$ vs. $\Phi(z)$. From the surface electric field $F(z = 0) = F_s$, V_g and the effective surface charge Q_s can be calculated, with some corrections as compared to Eq. (3.38):

$$V_g = \frac{\varepsilon_{sc}d_{ins}}{\varepsilon_{ins}}F_s - V_b + V_s + V_{FB} \ \text{ and } \ Q_s = \varepsilon_{sc}\varepsilon_0 F_s, \tag{3.44}$$

with $qV_b = \Phi_b$, $qV_s = \Phi_s$. V_{FB} is the flat band voltage, which accounts for differences in the work function of the gate electrode and the semiconductor, oxide or interface charges and oxide or interface carrier traps.

The potential (and the connected charge density n) as a function of z, follows from the relation

$$z = \int_{\Phi(z)}^{\Phi_s} \frac{d\Phi}{F_z(\Phi)}. \tag{3.45}$$

The accumulation depth, defined as $n(z) = n(0)/e$, is a function of the gate voltage V_g, since the screening length $L_{acc} = \sqrt{\frac{\varepsilon_0\varepsilon_{sc}k_BT}{\rho q^2}}$ depends on the charge carrier density. Hence, the assumption $d_{acc} \approx 1$ nm can only be valid for a small range of gate voltages.

Additionally to the accumulation, injection of carriers modifies the charge carrier density within the channel of a FET. For the overall description of FET devices, one can modify the Poisson equation as follows:

$$\frac{dF_x}{dx} + \frac{dF_z}{dz} = -\frac{q}{\varepsilon_{sc}\varepsilon_0}\left(n_{acc}(x,z) + n_d(x,z)\right) \tag{3.46}$$

Where x is the space coordinate which parallels the source–drain direction. n_{acc} is the density of accumulated charge carriers, n_d the density of injected charge carriers [69]. It is possible to circumvent the issue of $n = n(x)$ by choosing small fields between the source and drain electrode. Consequently, the field along the source–drain direction is almost constant and $\frac{dF_x}{dx} \propto p_d(x,z) \approx 0$. This approach is known as the gradual channel approximation [110].

4 Methodological Approach

This chapter adresses the methods used for the electrical and morphological characterization of the devices. The first part deals with the derivation of the mobility from the electrical characteristics of unipolar and ambipolar thin film transistors. The influence of semiconductor heterointerfaces, i.e. the semiconductor–insulator interface and the semiconductor–metal interface, on the charge transport is discussed, as well as the correction methods. The structural analysis was carried out by means of x-ray reflection and x-ray reflectivity, respectively, which is briefly described in the second part of the chapter.

4.1 Field Effect Transistor Devices

4.1.1 Unipolar Field Effect Transistor

An illustration of the Metal-Insulator-Field-Effect-Transistor (MISFET) device is shown in Fig. 4.1. The charge carrier density within a field effect transistor is varied capacitively. By applying a voltage between source and drain, charge carriers drift in the respective field, according to the respective charge carrier mobility μ within the semiconducting channel. Note that the diffusion term is assumed to be negligible in MISFETs, according to the Shockley model [110].

The application of an additional gate voltage, capacitively accumulates charge carriers within the semiconductor near the insulator surface. As the charge increases due to an increasing gate voltage V_g, the current I_d increases even though the electric field between source and drain remains constant. The charge Q_i introduced via gate voltage can by easily expressed by

$$Q_i = C_i\left(V_g - V_{th}\right). \tag{4.1}$$

C_i is the capacitance introduced by the gate dielectric and V_{th} is the threshold voltage. An additional voltage V_d between source and drain results in a variation of the local potential $V(x)$ at the location x within the channel, with $V(x)=0$ at the source contact and $V(L)=V_d$ at the drain contact. Hence, $Q_i(x)$ is determined by:

$$Q_i(x) = C_i\left(V_g - V_{th} + V(x)\right). \tag{4.2}$$

Neglecting diffusion, the current I_d between source and drain can be determined by simply applying Ohms law

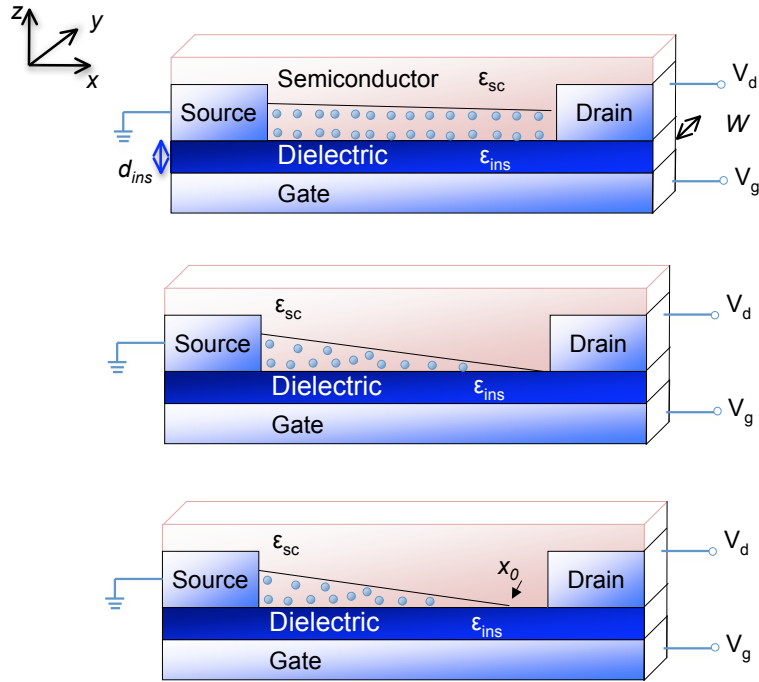$$\frac{I_d(x)}{W} = \sigma_{el} \cdot \frac{dV_d}{dx} = W\mu Q_i F_x,$$

Abbildung 4.1: Schematic of a field effect transistor in accumulation mode. Top: $V_d < V_g$, Middle: $V_d = V_g$ pinch-off; Bottom: $V_d > V_g$

where W is the channel width, σ_{el} is the conductivity, and $F_x = \frac{dV}{dx}$ is the x component of the electric field at position x. Note that the current as well as the accumulated charge are expressed as two dimensional quantities. The separation of variables yields

$$I_d dx = W \mu C_i (V_g - V_{th} - V(x)) dV. \tag{4.3}$$

The drain current follows from integration over the space coordinate x from source to drain

$$I_d = \frac{W}{L} \mu C_i \left((V_g - V_{th}) V_d - \frac{1}{2} V_d^2 \right). \tag{4.4}$$

Two different regimes can be distinguished: (i) The linear regime, where $V_g \gg V_d$ as illustrated in Fig 4.1 (top) and and Fig. 4.2(b) and the subtrahend in Eq. (4.4) can be neglected:

$$I_{d,lin} = \frac{W}{L} \mu_{lin} C_i (V_g - V_{th}) V_d \tag{4.5}$$

and (ii) the saturation regime as shown in in Fig. 4.1 (top) and Fig. 4.2, where $V_g \sim V_d$

$$I_{d,sat} = \frac{W}{2L} \mu_{sat} C_i (V_g - V_{th})^2, \tag{4.6}$$

where the current becomes independent of V_d. The channel is pinched off at $V_g = V(x)$ and charges cannot accumulate in the pinched off section of the channel. Accordingly, at $V_d > V_g$ the current remains constant as the source–drain field extracts all gate induced–charges.

The mobility is not calculated by simply dissolving Eq. (4.4) to μ, since μ can depend on the charge carrier density and, accordingly, on V_g. The linear and the saturation mobility, μ_{lin} and μ_{sat} are calculated from the partial derivative of I_d with respect to V_g. Hence, the linear mobility can be written as

$$\mu_{lin}(V_g) = \frac{\partial I_d}{\partial V_g} \frac{L}{W C_i V_d} \tag{4.7}$$

and the saturation mobility is

$$\mu_{sat}(V_g) = \frac{\partial I_d}{\partial V_g} \frac{L}{W C_i} \frac{1}{V_g - V_{th}} \tag{4.8}$$

The derivations of Eq. (4.7) and (4.8) are based on the assumption that the accumulated charge Q_i is a two dimensional quantity. If the screening length is large, the charge carrier density is rather extended across the extension of the semiconductor film. Nevertheless, electrostatics, as discussed in section 3.2, predict that the charge carrier density enhanced in the semiconductor fulfills the condition $\int_0^b \rho dz = Q_i$. If the mobility was independent of the charge carrier density, the derivation of the mobility remained unaffected by the dimensionality of the accumulated charge. However, if μ is a function of the charge carrier density, it would be in–depth dependent as the charge carrier density cannot be considered to be just two–dimensional, and hence, $\mu(V_g, z)$.

In order to explore the relation between charge carrier density and mobility, it is advantageous to investigate the linear regime, since here, the charge carrier density across the channel does not significantly vary, and the dependence of n on x can be assumed to be negligible. This approach follows the so-called gradual channel approximation (GCA), proposed by Shockley [110]. The application of the GCA demands that $\frac{\partial^2 V}{\partial x^2} \ll \frac{\partial^2 V}{\partial z^2}$. Hence, the channel potential can be assumed to be a linear function of the position x. This approximation states that the potential varies on a small scale along the channel, i.e., it requires $d_{ox} \ll L$, where L is the channel length.

Insulator and metal contact

Threshold voltage The threshold voltage V_{th} is the characteristic quantity, which describes the onset of charge accumulation at the gate–dielectric interface, i.e., $Q_i = C_i \cdot V_g$ in Eq. (4.1) becomes substituted by $Q_i = C_i \cdot (V_g - V_{th})$. The threshold voltage is governed by several contributions, as depicted in Fig 4.1.1. The surface electric field F_s determines the accumulated charge carrier density Q_i as $Q_i = \varepsilon_{sc} \varepsilon_0 F_s = \frac{\varepsilon_{ins} \varepsilon_0}{d_{ins}} (V_g - V_{th})$. V_{th} accounts for voltage losses not contributing to the formation of the surface electric field [55].

These quantities are

- the flat band voltage V_{FB}, which accounts for the work function differences between the gate electrode and the semiconductor. Also mobile and/or trapped charge carries/ions within the insulator or at the semiconductor–insulator interface modify V_{FB}.

- Another voltage drop has its origin in the difference between the surface potential (Φ_s) and the bulk potential Φ_b of the semiconductor. When the flatband condition is reached,
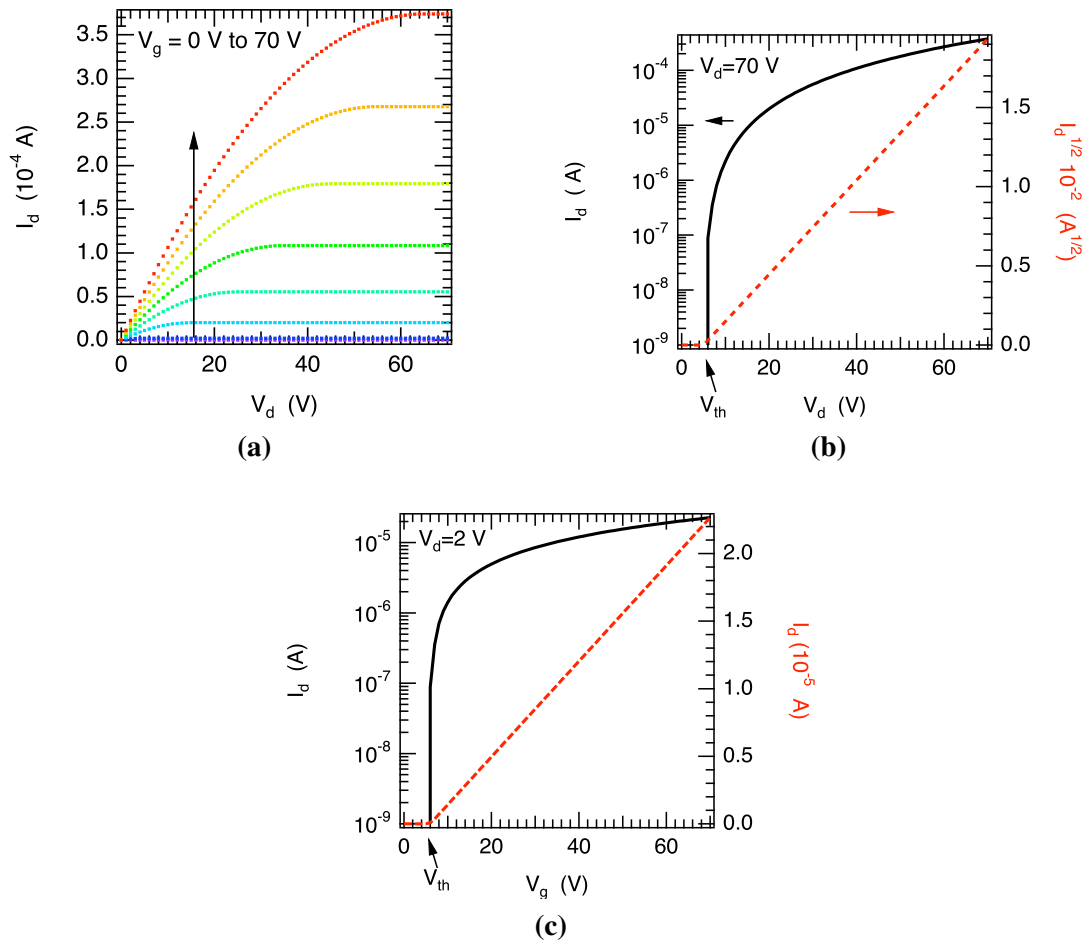
(a)

(b)

(c)

Abbildung 4.2: Generic characteristics of an unipolar field–effect–transistor as calculated from Eqs. (4.5) and (4.6) with μ_n=1·10^{-2} cm^{2}V^{-1}s^{-1}, d_{ins}=200 nm, ε_{ins}=4, L=100 μm, W=100 mm, V_{th}=5 V. (a) Output characteristics at different V_g as indicated by the arrow and by the color scale. (b) transfer characteristics in the saturation regime ($V_g = 70\ V$) and c) transfer characteristic in the linear regime ($V_g = 2\ V$). (b) and (c): The solid black lines represent the logarithmic scale of I_d and correspond to the left axis. The red dashed lines represent $\sqrt{I_d}$ and I_d and correspond to the right axis, in (b) and (c). The arrow towards the *abscissa* indicates the threshold voltage.

the potential gradient along the z direction is compensated and $\Phi_s - \Phi_b = 0$. In most cases, $\Phi_b - \Phi_s$ can be neglected, although, when using high resistivity semiconductors, its importance for the interpretation of current–voltage characteristics might become relevant. The voltage drop within the semiconductor is denoted as V_{sc}. Additionally, when dealing with doped materials, the threshold voltage is likely to shift, due to the altered bulk potential, which is connected to the doping density.

- An additional influence, which is commonly not accounted for is the voltage drop at the semiconductor–source electrode interface. As the contributions to the latter voltage drop are not unique for any device geometry, it is labeled $V_{sc,s}$ for simplicity.

- Fixed charges Q_{fixed} within the semiconductor also influence the threshold voltage. The voltage which needs to be overcome before the onset of accumulation is $\frac{-Q_{fixed}}{C_i}$.

The sum over the latter voltage drops gives the threshold voltage,

$$V_{th} = V_{FB} + V_{sc} + V_{sc,s} - \frac{-Q_{fixed}}{C_i}. \tag{4.9}$$

Each of the contributions in Eq. (4.9) can amount roughly to 1 V. When using insulator thicknesses around 100 nm and relatively high maximum gate voltages of several 10 V, the work function differences can result in a ratio $\frac{V_g}{V_{th}} \sim \frac{1}{20}$. However, the ratio becomes reduced when minimizing the device geometry to ultra thin gate dielectrics, as the fraction becomes $\frac{V_g}{V_{th}} \sim \frac{1}{3}$.

There exist several methods for the extraction of the threshold voltage [91]. As the current enters linearly in Eq. (4.5) and square-root like in Eq. (4.6), in this work, the onset of accumulation was determined by the extrapolation to $I_d = 0$ A of $I_d - V_g$–plots in the linear and of $\sqrt{I_d} - V_g$–plots in the saturation regime.

Contact resistance

Here, the theoretical origin of the contact resistance will first be briefly described, then two correction methods will be discussed. The injection barrier between the HOMO/valence band within a p–type semiconductor (or LUMO/conduction band within an n–type semiconductor) and the source and drain electrodes, results in non–Ohmic contacts and I_d is influenced by an additional voltage drop at the semiconductor–metal interface. This can cause inprecise mobility data.

A model scheme of a metal–semiconductor contact is depicted in Fig. 4.4. In thermodynamic equilibrium, the Fermi levels of the metal Φ_{Me} and the semiconductor align. In the illustrated case, the contact in formed between an n type semiconductor and a high work function material. Due to diffusion of electrons from the semiconductor to the metal, the E_{HOMO} and E_{LUMO} bend upwards. In most cases, the morphology of the semiconductor at the metal–semiconductor interface is different from the bulk morphology, e.g. due to lattice constant mismatch, molecular reorientation, a high grain density and the forming of metal-semiconductor complexes [20]. Interface states can induce interface dipoles Δ_{DIP}, which partly compensate or enhance the work function difference. Φ_{Me} is then replaced by $\Phi_{Me,eff} = \Phi_{Me} - \Delta_{DIP}$. As a consequence, a hole injection barrier δ_{HIB} and an electron injection barrier δ_{EIB} is formed.
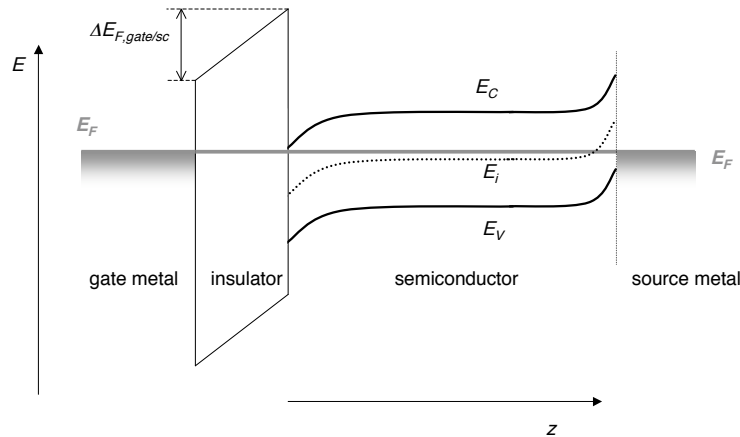
Abbildung 4.3: Model scheme of the band bending in FETs between the gate and the source metal at $V_g = 0$ V (illustration not to scale) for the case of a slightly n-doped material. The Fermi level difference between the gate metal and the semiconductor induces band bending at the insulator–semiconductor interface, the respective difference between the semiconductor and the source–electrode induces the formation of a space charge region (Schottky contact; no interface defects nor mirror charges assumed). As the voltage drop at either contact has to be compensated by the gate voltage, the threshold voltage is influenced by the work functions of the source and gate metals.
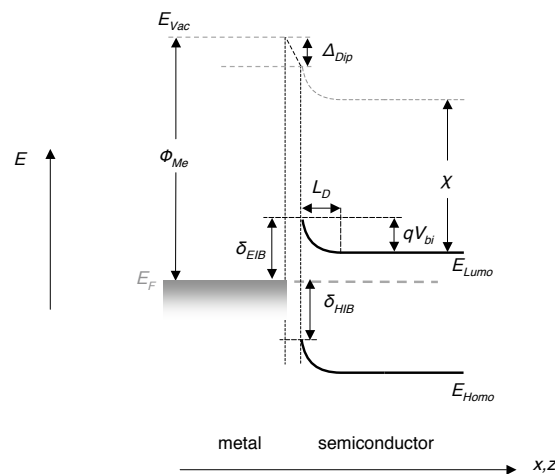

Abbildung 4.4: Model scheme of the band bending at the metal–semiconductor interface. In thermodynamic equilibrium the Fermi levels align. Φ_{Me} is the metal work function, χ is the electron affinity of the semiconductor, Δ_{DIP} interface dipole, $\Phi_{Me,eff} = \Phi_{Me} - \Delta_{DIP}$, E_{HOMO} and E_{LUMO} are the maxima of the respective Gaussian DOS, δ_{HIB} and δ_{EIB} are the hole and electron injection barrier, respectively, V_{BI} is the built in potential, L_D is the screening length which determines the width of the band bending

An additional effect, which is not depicted in Fig. 4.4, is the Coulomb binding of the charge carrier in the semiconductor to its image twin at the electrode. This lowers the potential as a function of distance x from the electrode. The lowering of the energy as a function of x is then $E_{image}(x) = -\frac{e^2}{16\pi\varepsilon_0\varepsilon_{sc}x}$ [8, 9]. The potential $\Phi(x)$ at the distance x from the electrode under applied bias becomes

$$\Phi(x) = \delta - \frac{e^2}{16\pi\varepsilon_0\varepsilon_{sc}x} - eFx, \tag{4.10}$$

where F is the field strength due to an externally applied voltage. Consequently, the maximum of the barrier height Φ_{max} is not necessarily located at the interface, instead it is found from the derivative $\frac{d\Phi}{dx} = 0$. The injection mechanism from the source metal to the semiconductor in the presence of a barrier is classically governed by either thermionic emission over or field emission through the barrier or the combination of the latter mechanisms, phonon-assisted tunneling.

Thermionic emission from a metal to a semiconductor is described by the Richardson–Schottky model. The relation between the current density j_{th}, the temperature and the barrier height is [118]

$$j_{th} \propto T^2 \exp\left(-\frac{\Phi_{max}}{k_B T}\right). \tag{4.11}$$

In Eq. (4.11) charge carrier back flow from the semiconductor to the metal is neglected. Moreover, it is assumed that the metal is an infinite reservoir for electrons and charge carrier scattering at the metal–insulator interface is negligible. As the mobility in disordered and nanocrystalline semiconductors is likely to be rather low, thermionic emission is usually not the rate-limiting process at room temperature. Instead, the presence of thin insulating layers at the metal–organic interface can decrease the current density. Depending on the width of the barrier and the electric field strength, carriers can tunnel through the barrier.* The current density for Fowler–Nordheim tunneling through a triangularly shaped potential barrier is independent of the temperature but dependent on the applied field F [118].

$$j_{FN} \propto F^2 \exp\left(-\frac{2\gamma\Phi_{max}^{3/2}}{eF}\right) \tag{4.12}$$

where γ is a constant. Note that the charge transport across a barrier can be of hybrid character, i.e., thermal activation with subsequent tunneling through the barrier.

The influence of the contact resistance can be minimized by choosing metal–semiconductor combinations which establish (almost) Ohmic contacts. In addition the contact resistance can be eliminated calculative by two different methods as described in the following.

Correction: Transmission line method (TLM)

The gated transmission line method (TLM) [46, 48] is based on the assumption that the total channel resistance R_{on} is the sum of three independent resistors, R_{source}, $R_{channel}$ and R_{drain}, at

---

*As a result from the Schrödinger equation, the wavefunction Ψ exponentially decays within the insulator as a function of the momentum $k = \sqrt{2m^*(\Phi - E)}/\hbar$ and distance as $\Psi(x+dx) = \exp(-k\,dx)$ (minus sign: propagation from left to right). When applying a voltage, the approximately triangular barrier gets shortened. As the energy levels at both sides of the barrier must be equal, the condition $x_t = \Phi/F$ must be fulfilled, with the tunneling distance x_t. Hence, the tunneling probability is proportional to $\exp(-\Phi^{3/2}/eF)$

source, channel and drain, respectively. Hence, $R_{on} = (R_{source} + R_{drain}) + R_{channel}$. R_{on} at a given V_g can be easily extracted from the slope $\left(\frac{dI_d}{dV_d}\right)^{-1}$ in the linear regime of the output characteristics. Using different channel lengths, the contact resistance can be extracted by extrapolating to $R_{on}(L=0\text{ m})$. The slope of R_{on} *vs.* L is determined by the corrected channel mobility

$$\frac{\partial \left(\frac{\partial R_{on}}{\partial L}\right)^{-1}}{\partial V_g} = \mu_{FET}(V_g, T)WC_i. \tag{4.13}$$

This determination of the corrected mobility seems to be a straight forward. Effectively, one has to keep in mind, that a high injection barrier can also result in less accumulated charge carriers. Since $\mu = \mu(n)$, smaller injection currents can also result in effectively smaller mobilities, but a misestimation of the charge carrier density is not considered by this method.

Correction via drain and transconductance

In this approach, it is assumed, that V_d has to be corrected for a voltage drop at the series resistance R_s, i.e. $V_d \rightarrow V_d - I_d R_s$ [56].

$$I_d = \frac{W}{L}C_i\mu(V_g - V_{th})(V_d - I_d R_s) \tag{4.14}$$

A prerequisite for the applicability of this method is, that μ does not (or only weakly) vary with V_g.

Using the drain conductance g_d, which corresponds to $1/R_{on}$ in the above the TLM–method,

$$g_d = \frac{\partial I_d}{\partial V_d} \tag{4.15}$$

and the transcontuctance g_m

$$g_m = \frac{\partial I_d}{\partial V_g} \tag{4.16}$$

one obtains an expression for the mobility

$$\frac{g_d}{\sqrt{g_m}}\sqrt{\frac{LV_d}{WC_i}} = \sqrt{\mu}(V_g - V_{th}), \tag{4.17}$$

and an expression for the contact resistance

$$R_s = \frac{1}{g_d} - \frac{L}{WC_i}\frac{1}{\mu(V_g - V_{th})}. \tag{4.18}$$

Hence, the contact resistance R_s corresponds to $R_{on}(L)$ in the TLM. An advantage of this method is the possibility of deriving the contact resistance and the corrected mobility from measurements on only one transistor structure. When the output and linear transfer characteristics are available, the respective R_{on} and μ_{corr} can be easily calculated, which is comfortable especially at variable temperature measurements.

Measured *vs.* actual μ at different channel length L

It was found, that the effect of the contact resistance on the mobility can be minimized, when large L are chosen, as in this case, the channel resistance outweights the contact resistance [50, 52] .

Correction for the derivative of the mobility

As μ is a function of V_g, especially in disordered and nanocrystalline semiconductors, its derivative has to be taken into account in Eq. (4.4) according to Katz [64].

$$\frac{\partial I_d}{\partial V_g} \propto \mu(n_{acc}) + f(\frac{\partial \mu}{\partial V_g}).$$

(4.19)

In contrast, a partial derivative actually excludes the latter approach, so that the derivative of the current with respect to the charge carrier density (as long as n_{acc} is known) will lead to the correct mobility [133]. An attempt to correct the mobility according to Eq. (4.19) is done iteratively

$$\mu_0 + \frac{\partial \mu_0}{\partial V_g} \cdot (V_g - V_{th} - \frac{1}{2}V_d) + f\left(\frac{\partial \frac{\partial \mu_0}{\partial V_g}}{\partial V_g}\right)....$$

(4.20)

Eq. (4.20) converges if μ changes only slowly with V_g. As large variation of μ *vs.* V_g can occur in disordered semiconductors, the resulting μ_{corr} often does not converge.

Katz *et al*. [64] suggested an approach to correct the mobility for the surface charge carrier density n_s at the position x along the channel. By modifying Eq. (4.2), n_s becomes

$$n_s = \frac{\varepsilon_{ins}\varepsilon_0}{d_{ins} \cdot e} \cdot (V_g - V_{th} - V(x)).$$

(4.21)

Since any function can be fitted by a polynomial expansion, $\mu(V_g)$ can be expressed as

$$\mu(n_s(x)) = \sum_{n=0}^{N} \mu_n (V_g - V_{th} - V(x)),$$

(4.22)

where μ_n are the respective coefficients of the polynomial. For the sake of completeness, the drift current I_d, neglecting the contact resistance, is

$$I_d = Wen_s(x)\mu(x)\frac{dV(x)}{dx}$$

(4.23)

Inserting Eq. (4.21) and Eq. (4.22) into Eq. (4.23) leads to

$$\int_0^L \frac{I_d\varepsilon_{ins}\varepsilon_0}{W d_{ins}}dx = \int_0^{V_d} \sum_{n=0}^{N} \mu_n(V_g - V_{th} - (V(x))^{n+1}))dV$$

(4.24)

The integration gives an expression for I_d

$$I_d = \frac{W\varepsilon_{ins}\varepsilon_0}{Ld_{ins}} \sum_{n=0}^{N} \frac{1}{n+2}\mu_n((V_g - V_{th} - V_d)^{n+2}) - (V_g - V_{th})^{n+2}).$$

(4.25)

The transconductance in the linear regime can therefore be written as

$$\frac{\partial I_d}{\partial V_g} \frac{w\varepsilon_{ins}\varepsilon_0}{L d_{ins}} \sum_{n=0}^{N} \mu_n \left(V_g - V_{th} - V_d \right)^{n+1} - \left(V_g - V_{th} \right)^{n+1}. \tag{4.26}$$

The coefficients μ_n can be found by applying the polynomial expansion in Eq. (4.22) to the derivative of the experimental I_d–V_g characteristics. Hence, the dependence of μ on n_s can be found (note: not μ vs. V_g).

The strength of this method is, that an error due to $\frac{\partial \mu}{\partial V_g}$ can be corrected. However, one has to keep in mind, that two assumptions have to be made for the application of this method: (i) only surface charges at the gate dielectric contribute to the charge transport and (ii) for the calculation of their density Eq. (4.21) is valid, i.e. the mobility does not vary along z.

4.1.2 Ambipolar Field Effect Transistor

In ambipolar FETs, both charge carrier species, electrons and holes, notably contribute to the charge transport. When applying a positive (negative) gate voltage, electrons (holes) are accumulated, while holes (electrons) get depleted from the channel. In the saturation regime of an *unipolar* transistor, as described by Eq. (4.6), the current can not further increase with V_d, as charge accumulation is inhibited by the superposition of the source–gate field with the source–drain field. In an *ambipolar* transistor, the effective gate potential sign change at $V_d > V_g - V_{th,p}$, allows for the injection of holes and electrons from opposite sides of the channel.

Assuming an infinite recombination rate of electrons, charges recombine at a certain definite point x_0 in the channel, as in an abrupt *pn*–junction. At x_0, the accumulated charge is zero and consequently $V_g - V(x_0) = 0$. The total resistance can then be described as the series resistance of two independent transistors, i.e. the resistance R_n in the electron accumulation region and R_p in the hole accumulation region [106, 116].

Neglecting the threshold voltage for simplicity, the channel resistance $R(x)$ between source ($x=0$) and x at $V_d \geq V_g$ is given by

$$R(x) = \int_0^x \frac{dx}{\sigma_{el}(x)} = \int_0^x \frac{dx}{W\mu Q(x)} \tag{4.27}$$

$R_{tot} = R(L)$, hence, $V(x)$ is given by the fraction $\frac{R(x)}{R_{tot}}$ of V_d

$$V(x) = V_d \frac{R(x)}{R_{tot}} \tag{4.28}$$

substituting $V(x)$ in Eq. (4.2) a subsequent differentiation for x gives

$$\frac{dQ}{dx} = \frac{C_i V_d}{R_{tot}} \frac{1}{W Q_i(x)\mu.} \tag{4.29}$$

The charge carrier density at the source contact ($x=0$) is given by $C_i V_g$. The integration of Eq. (4.29) gives

$$Q(x) = \sqrt{C_i^2 V_g^2 - 2\frac{C_i V_d}{\mu W R_{tot}}x} \tag{4.30}$$

with $Q(L) = C(V_g - V_d)$ in the linear regime, the channel resistance is

$$R_{tot} = \frac{L}{\mu W C_i \left(\frac{1}{2}V_d - V_g\right)}. \tag{4.31}$$

At high drain bias, where the channel is pinched off in the case of an unipolar transistor, charges of the opposite sign can penetrate into the sample from the drain contact. Assuming infinite recombination rates, the channel can be devided into two resistors, the n–channel resistor R_n (from $x=0$ to $x = x_0$) and the p–channel resistor R_p (from $x = x_0$ to $x = L$), as shown in Fig. 4.5(a).

$$R_n = \frac{2x_0}{W\mu_n C_i(V_g)}, \quad R_p = \frac{2L - x_0}{W\mu_p C_i(V_d - V_g)}. \tag{4.32}$$

As the current through both resistors is equal, the recombination zone x_0 is given by

$$x_0 = \frac{LV_g^2}{V_g^2 + \frac{\mu_n}{\mu_p}(V_d - V_g)^2} \tag{4.33}$$

Eq. (4.30) and Eq. (4.2) yield $Q(x)$ (see Fig. 4.5(b)) and $V(x)$ (not shown) by replacing R_{tot} by either R_n between $x = 0$ and $x = x_0$ or R_p between $x = x_0$ and $x = L$.

The drain current is derived using $I_d = V_d/R_{tot}$. The threshold voltages for electrons $V_{th,n}$ and holes $V_{th,p}$ usually differ. Hence, ambipolar FETs are governed by three different transport regimes, i.e. the linear ($V_d \leq (V_g - V_{th,n})$ and the saturation regime $V_d \geq (V_g - V_{th,n})$ but $V_d \leq (V_g - V_{th,p})$), as in unipolar transistors, and the ambipolar regime $V_d \geq (V_g - V_{th,p})$. In the latter regime, electrons as well as holes are injected and recombine at at certain distance from the electrodes.

For the positive bias condition $V_g > 0 \wedge V_d > 0$, which can be easily transferred to $V_g < 0 \wedge V_d < 0$, the current–voltage characteristics are then determined by these three different cases:

linear range: $V_d \leq (V_g - V_{th,n})$

$$I_d = \frac{W}{L}\mu C_i \left((V_g - V_{th,n})V_d - \frac{1}{2}V_d^2 \right),$$

Saturation range: $V_d \geq (V_g - V_{th,n})$ but $V_d \leq (V_g - V_{th,p})$

$$I_d = \frac{2W}{L}\mu C_i (V_g - V_{th,n})^2 \Theta(V_g - V_{th,n}),$$

ambipolar range: $V_d \geq (V_g - V_{th,p})$

$$I_d = \frac{2W}{L}C_i(\mu_n \cdot (V_g - V_{th,n})^2 \Theta(V_g - V_{th,n}) + \mu_p \cdot (V_d - (V_g + V_{th,p})^2)). \tag{4.34}$$
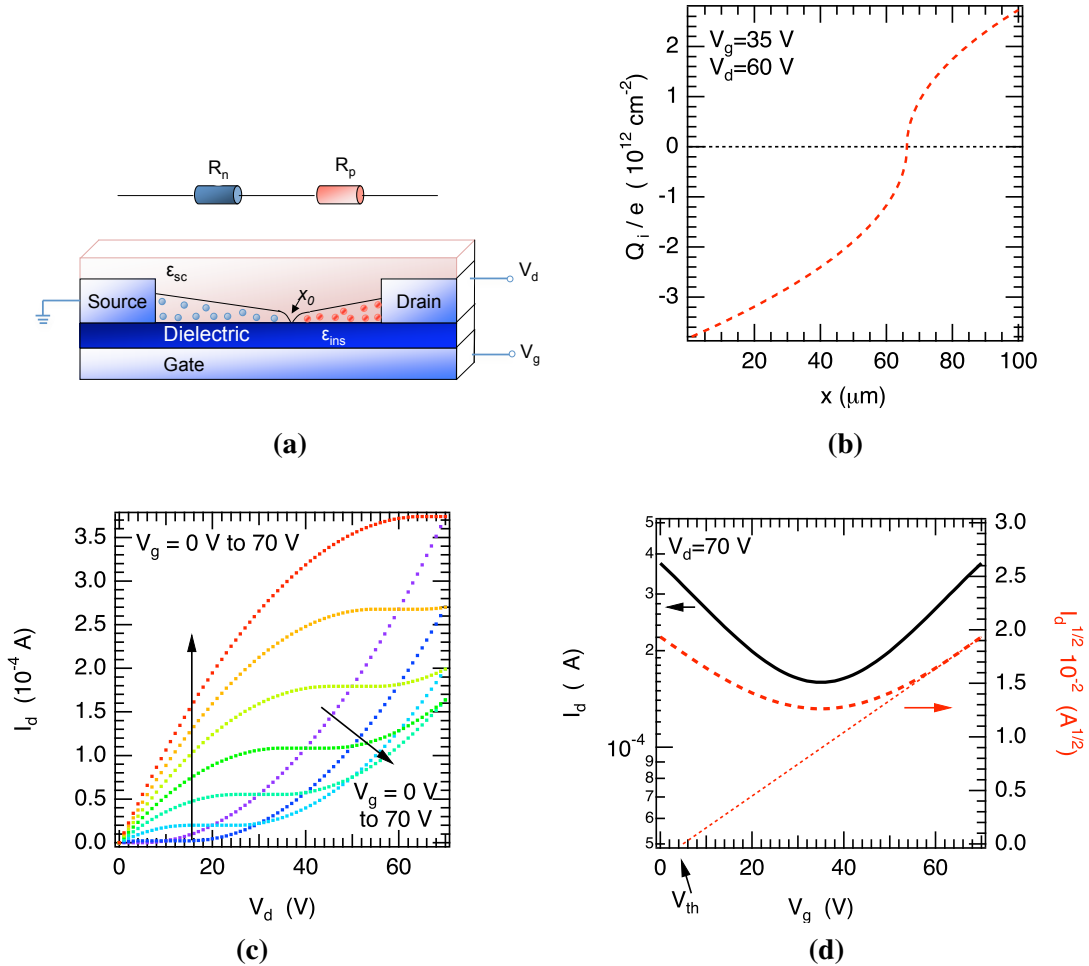
Abbildung 4.5: Ambipolar transistor: (a) Schematic of a field effect transistor working in the ambipolar range. For the mathematical description, the total channel resistance is divided into R_n and R_p as described in the text. (b) Charge distribution along the channel in the ambipolar range as calculated from Eq. (4.30) and Eq. (4.2). (c) and (d) Generic characteristics of an ambipolar transistor as derived from Eqs. (4.34) with $\mu_n = \mu_p = 1 \cdot 10^{-2}$ cm^{2}V^{-1}s^{-1}, d_{ins}=200 nm, L=100 μm, W=100 mm, $V_{th,n}$=-$V_{th,p}$=5 V at positive gate and drain voltages. (c) Output characteristics at different V_g as indicated by the arrows and by the color scale. (d) Transfer characteristic in the saturation regime ($V_g = 70\ V$). The solid black line represent the logarithmic scale of I_d corresponding to the left axis. The red dashed line represents $\sqrt{I_d}$ corresponding to the right axis. The arrow towards the *abscissa* indicates the threshold voltage. Note that the linear transfer characteristic (not shown) for ambipolar transistors equals that for unipolar transistors in Fig. 4.2(b).

Θ is the Heaviside step function.

The generic output and transfer characteristics for $\mu_n = \mu_p$ and $V_{th,n} = -V_{th,p}$ are shown in Fig. 4.5. Note that all values, except $V_{th,p}$ and μ_p are chosen equally to the parameters in Fig. 4.2. At small V_g and high V_d the ambipolar regime results in diode–like output characteristics which becomes less pronounced at high V_g, as the pinch-off point ($V_g - V_{th,n} = V_d$) is shifted to higher V_d as shown in Fig. 4.5(c). The transfer characteristics in the saturation regime, as indicated in Fig. 4.5(b), is governed by a high current at $V_g = 0$, as a result from electron and hole injection. I_d then decreases with increasing V_g, due to hole depletion. The subsequent increase of I_d is mainly caused by electron accumulation. Ambipolar transistors exhibit a low on/off ratio[†] which is a major drawback for the application in complimentary metal–oxide semiconductor technology.

4.2 Structural analysis

X-ray analysis

X-ray diffraction (XRD) The crystallographic properties of semiconductors can be characterized by X-ray diffraction. The wavelength of the impinging beam (e.g. λ=1.5406 Å for Cu_{K_α} is in the order of the lattice constant of solids. Assuming specular reflectance,[‡] the variation of the incident angle θ leads to interference fringes being specific for the crystal lattice constant due to constructive interference of the beam at the lattice planes. The distance a between lattice planes can be determined from Bragg's law

$$m\lambda = 2a\sin\theta \tag{4.35}$$

where m is an integer representing the order of diffraction. Historically, in XRD, the angle is measured relative to the horizontal z of the sample plane.[§] Large angles correspond to small distances or higher orders of diffraction. The constructive interference in an X-ray measurement is in fact a measure for the reciprocal lattice. Hence, it is convenient to describe the diffraction data in terms of the reciprocal lattice vector G and the wave vector transfer $q_z = \frac{4\pi}{\lambda}\sin\theta$ instead of the angle θ, as q_z is independent of the wavelength. The wave vector transfer also provides facile comparable data of diffractograms recorded with ray of different wavelength. Bragg's law can be easily written as

$$2\vec{q}\cdot\vec{G} = G^2, \tag{4.36}$$

which is known as the Laue condition. When only considering the wave vector transfer, one can write

$$q_z = G \tag{4.37}$$

It is worth mentioning that the analysis of XRD diffractograms provides information on the lattice plane spacing perpendicular to the surface while the charge carrier motion in field effect

---

[†]the current ratio between the maximum applied voltage $V_{g,max}$ and the minimum applied voltage $\frac{I_d(V_{g,max})}{I_d(V_g-V_t=0)}$, measured in decades

[‡]specular reflectance: angle of incident beam = angle of reflected beam

[§]in contrast to optics, where the angle is measured relative to the surface normal

transistors occurs parallel to the substrate. However it is a good measure for the degree of crystallinity in the sample.

The crystallite height l can be assessed from the full width at half maximum $\Delta(2\theta)$ of the peak employing the Debye–Scherrer formula

$$\Delta(2\theta) = (K_s\lambda)/(l \cdot \cos\theta), \tag{4.38}$$

where θ the peak maximum position, K_s is a factor accounting for the shape of the crystallite and is approximately unity. [62]. Note that strain effects, which can also broaden the peak are neglected in Eq. (4.38).

X-ray reflectivity (XRR)

X-ray reflectivity provides a non-destructive way to monitor the stoichiometry, thickness and roughness of thin layers. Its main strength over other methods, e.g. AFM, SEM, lies in the study of buried layers and interfaces. The method will be briefly described here, a more detailed review is found in Ref. [49, 101].

While XRD is commonly used at angles $5° < \theta < 90°$, XRR employs the smaller angles $\theta < 5°$. Here, the oscillations of the detected signal with varying θ, the so-called Kiessig fringes, correspond to the thickness of the studied thin film. Thicknesses around 1 Å up to approximately 200 nm can be detected.[¶]

When X-rays penetrate a material, they become scattered mainly by the electron density, which is a material specific parameter. At small angles, the electron density is effectively continuous, allowing for the description of the reflection and transmission with a material specific refractive index n_x. As the real part of n_x for X-rays within a solid is smaller than one, i.e., smaller than the index of air or vacuum, total reflection at the surface occurs at small angles θ typically between $0°$ to $0.2°$. Larger electron densities ρ_e, i.e. larger material densities, involve larger critical angles θ_c, see Fig.4.7(a). The complex index of diffraction can be written as

$$n_x = 1 - \delta - i\beta. \tag{4.39}$$

δ corresponds to dispersion and its value (usually around 10^{-5} to 10^{-6}) is positive, β corresponds to absorption within the material ($\beta \approx \delta/10$ to $\delta/100$). From the scattering by a classical dipole oscillator, the following relations can be found:

$$\delta = \frac{\lambda^2}{2\pi}r_e\rho_e \qquad \beta = \frac{\lambda}{4\pi}\mu_{abs} \tag{4.40}$$

where $r_e = 2.8 \cdot 10^{-15}$m is the classical electron radius, ρ_e is the electron density of the material, μ_{abs} is the linear absorption coefficient and λ is the characteristic wavelength of the incident X-ray beam. Snell's law relates the angle of the incident beam θ_i to the angle of the transmitted beam θ_t

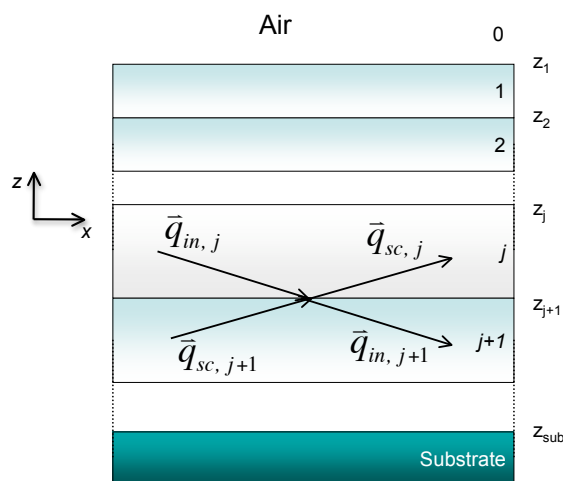$$n_x = \frac{\cos\theta_i}{\cos\theta_t}. \tag{4.41}$$

[¶]The determinable thickness depends on the impinging wavelength. It is also possible to monitor reflection curves by neutron scattering which is sensitive to the density of atomic cores ρ_{nuclei}
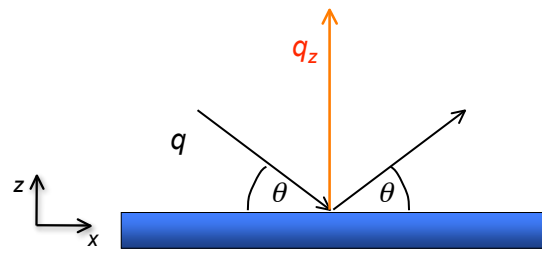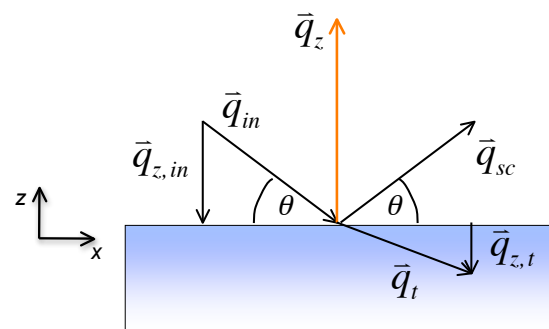
Abbildung 4.6: (a) Schematic to illustrate the impinging and backscattered wave vector for XRD, (b) Schematic to illustrate the transmitted wavevector at small angle (the medium can be considered to be continuous and the index of refraction n_x can be used classically) (c) illustration of multiple reflection.

The more convenient form in the reciprocal space is

$$\vec{q}_t = n_x \vec{q}_i \tag{4.42}$$

where q_t is the wave vector of the transmitted ray and q_{in} is the wavevector of the incident beam. The boundary condition from electrodynamic considerations states that the parallel components $q_{t,x}$ and $q_{i,x}$ remain unchanged upon reflection

$$q_{i,x} = q_{t,x}. \tag{4.43}$$

An approximative relation between the critical angle and the electron density can be found using the Taylor expansion

$$\theta_c \sim \sqrt{2\delta} = \lambda \sqrt{r_e \rho_e / \pi}. \tag{4.44}$$

Fresnel coefficients In oder to calculate the transmitted and the reflected intensities, T and R, respectively, the Fresnel-coefficients, r and t, respectively, are utilized. The reflected amplitude is then obtained by assuming continuity of the electric and magnetic field at the interface.$^{\parallel}$

$$r = \frac{q_{z,in} - q_{z,t}}{q_{z,in} + q_{z,t}} \tag{4.45}$$

$$t = \frac{2q_{z,in}}{q_{z,in} + q_{z,t}} \tag{4.46}$$

The amplitude of the reflected signal is then with $q_c = q_z(\theta_c)$

$$R(q_z) = rr^* = \left| \frac{q_z - \sqrt{q_z^2 - q_c^2 - \frac{32i\pi^2\beta}{\lambda^2}}}{q_z + \sqrt{q_z^2 - q_c^2 - \frac{32i\pi^2\beta}{\lambda^2}}} \right|^2, \tag{4.47}$$

Neglecting absorption and applying the Taylor expansion to $\sqrt{q_z^2 - q_c^2} = q_z\sqrt{1 - q_c^2/q_z^2}$ leads to

$$R(q_z) \approx \left(\frac{q_c}{q_z} \right)^4 \tag{4.48}$$

The decrease of the reflected intensity with q_z^{-4} is another prominent feature of XRR–spectra.

$$\tag{4.49}$$

Multiple interfaces The Kiessig fringes which result from multiple reflections at interfaces give an estimate for the film thickness

$$d = \frac{2\pi}{\Delta q_z}. \tag{4.50}$$

In order to describe the data more precisely, the Fresnel coefficients for each layer have to be calculated. A method to assess the reflectance from multiple interfaces was introduced

---

$^{\parallel}$The difference between *s*- and *p* polarization is small and be usually neglected.
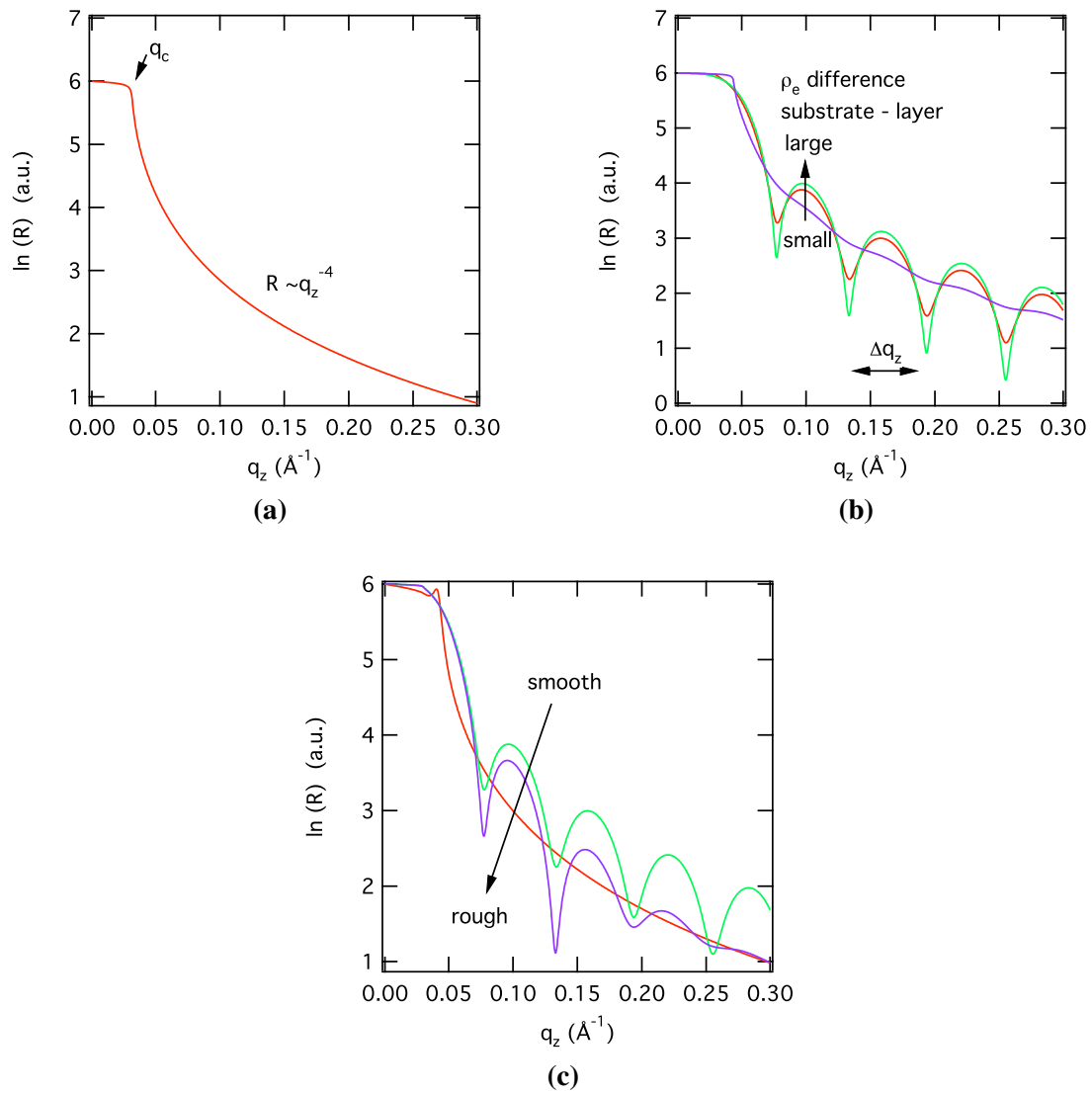
Abbildung 4.7: (a) Reflection of X-rays at a smooth interface, q_c and the rapid decrease of R with q_z^{-4} are indicated. (b) Reflection at a thin layer (here 10 nm) with smooth interface. The distance between two adjacent Kiessig–fringes Δq_z is a measure for the layer thickness, The difference between the electron density of the substrate and the layer is varied, as indicated by the legend. c) Reflection at a thin layer at various surface roughness. The reflectivity was calculated with a program presented in Ref. [87]

by Parratt [98]. The basic assumptions are drawn here. Each layer ist treated as a box, for which the transmitted and reflected light is calculated. The ratio between the reflected and the transmitted amplitude in the jth layer is calculated starting from the bottom (Nth) layer, as shown in Fig. 4.6(c).

$$X_j = \frac{r_j}{t_j} \tag{4.51}$$

$N+1$ iterations, for each layer result in the reflection from the surface. The influence of the interface roughness is taken into account with $R_{rms,j}$, the square root of the mean squared height fluctuation $h(x,y)+h_0$

$$R_{rms,j} = <(h(x,y)+h_0)>^{1/2} \tag{4.52}$$

In the case of rough interfaces the Fresnel coefficient becomes enhanced by a factor $\exp(q_{z,j}q_{z,j+1}R_{rms,j}^2)$. For a one layer system, the theoretical curves are shown in Fig. 4.7(c). Due to surface roughness, the Kiessig Fringes get attenuated. The calculated reflectivity is then compared to the experimental data. By refinement of the starting parameters, the deviance χ^2 between calculated and measured reflectivity data is minimized.

5 Sample Preparation and Measurement

Field-Effect-Transistor Devices

The field effect transistor structures were prepared on Sb-doped silicon wafers purchased at Silicon Materials, Germany. The highly n++-doped Si (001) with a nominal resistivity of about 0.02 Ωm serves as the gate electrode of the FET structure. The top layer of the wafer consists of 200 nm thermally grown SiO_2 which forms the dielectric. In this work, top as well as bottom-contact structures, as depicted in Fig. 5.1 were used.
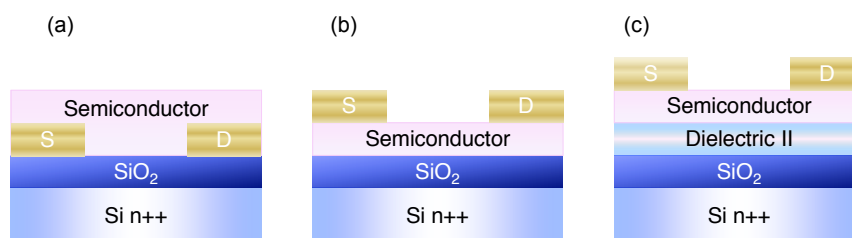

Abbildung 5.1: Layer setup of the FET structures employed for the investigations (S/D: source/drain electrode): Device geometries used throughout this thesis (a) bottom contacts on top of the SiO_2 layer (b) top contacts with SiO_2 dielectric (c) top contacts with a modification of the dielectric.

Throughout this thesis, unless otherwise stated, the following geometries were used:

- The bottom-contact structures shown in Fig. 5.1(a) were in either case built upon SiO_2 using photo-lithographic patterning of the source and drain electrodes. The procedure of patterning the electrodes demands high-work-function metals, in this work Au with a nominal work function Φ_{Me} of 5.1 eV was used.

- For the top-contact structures shown in Fig. 5.1(b), the semiconductor was first applied upon the SiO_2 dielectric, followed by thermal evaporation of the source and drain electrodes through a shadow mask.

- For the top-contact structures shown in Fig. 5.1(c), an additional dielectric was applied on top of the SiO_2 dielectric prior to the application of the semiconductor. The evaporation of the source and drain metal is analogous to the device in Fig. 5.1(b).

In the case of the top contact structures, also low-work-function materials such as Al (Φ_{Me}= 4.3 eV) and Ca (Φ_{Me}=2.9 eV) can be used. The metal workfunctions are depicted in Tab. 5.1.

Photolithography was used to get well-defined source–drain structures, such as ringlike geometries (Caribou structure) as depicted in Fig. 5.2(a). This structure avoids parasitic effects,
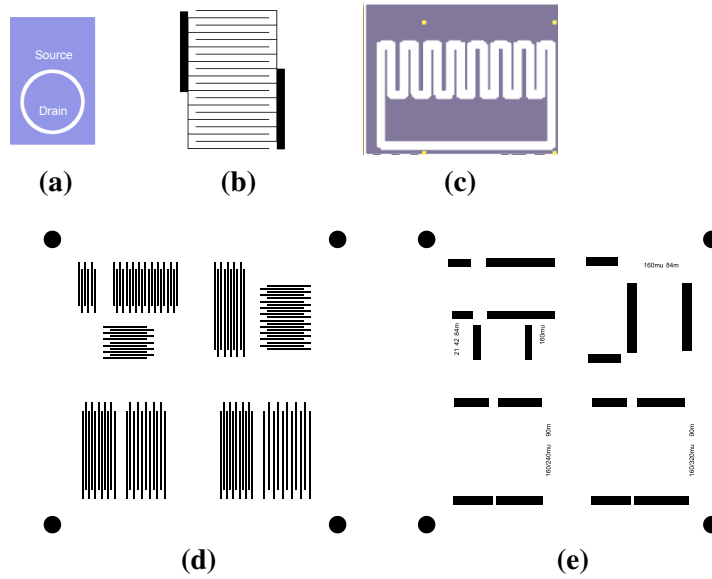
Abbildung 5.2: (a) The Caribou structure of the source and drain contacts which reduces parasitic effects at the edges such as current leakage between S/D and the gate electrode. (b) Interdigitated structure of source- and drain-electrodes. (c) combination of the Caribou and the interdigitated structure (d) and (e) Top contact masks: after subsequent use, an interdigitated structure is attained.

which have their origin in the floating potential at the edges of linear structures. Also, interdigitated structures were used which have the advantage of large channel width and hence, large currents and the averaging over large areas of the sample. The advantages of the structure in Fig. 5.2(a) and Fig 5.2(b) are combined in the structure shown in Fig. 5.2(c).

For bc-Au devices, the following lithography steps were applied:

- An adhesion promoter containing Ti spin cast on SiO_2.

- A lift-off resist which is soluble in the developer spin cast on top.

- photosensitive positive resists spin cast on top.

- Light exposure followed by development: Light-exposed regions are removed in the developer. The lift-off resist develops isotropically creating a bi-layer reentrant sidewall profile The lift–off resists improves the contrast.

- 1 nm Ti as an adhesion layer and subsequently 19 nm thick Au contacts were thermally evaporated on top of the dielectric.

- Lift-off in an ultrasonic bath with acetone, the photoresist and Ti/Au on top of the resist are removed

As a last step, the semiconductor is deposited from solution.

For the top-contact geometry, either rectangular-shaped source- and drain-contacts separated by the channel length L were evaporated or interdigitated structures were achieved in a two step process: First, digits were evaporated with a mask shown in Fig. 5.2(d), then the digits

were connected with the mask indicated in Fig. 5.2(e). This increases the channel width W and, hence, the drain current, while the the long term mechanical stability of the evaporation mask is provided.

The advantage of the bottom contact geometry is that the design of the metal electrodes is arbitrary, while the design of a top contact mask is limited by mechanical stability. Moreover, ringlike geometries are not possible for top contact structures. When using a shadow mask instead of photo-lithographical steps, low-workfunction metals can be used (also for bottom-contact geometries). The main advantage of the top contact structure is the improved injection due to the source-gate electric field.

Electrical Characterization

For characterization of the field-effect transistor structures both, room temperature and temperature dependent measurements were independently carried out in different setups. The room temperature measurements were carried out under inert gas atmosphere in a nitrogen-supplied glove-box system. The transistors were mounted on a temperature-stabilized metal plate which served as the electrical connection to the gate terminal. Contacting positions on the source and drain electrodes were identified with a magnifying CCD-camera while electrical sensing of the S-D channel was realized with micro-probes. The temperature dependent characterization of the FET structures was carried out either in a Helium closed cycle cryostat (Leybold) or by means of a continuous-flow cryostat (LN2 or LHe) combined with a micro-probe station (Janis S500) and a magnifying CCD camera. All signal processing and data acquisition was done with an Agilent 4155C parameter analyzer. The temperature adjustment and stabilization was realized with Lakeshore 332 and 330 temperature controllers, respectively.

6 Results

6.1 Charge Transport in PCBM Thin Films Employing a Gaussian Density of States

The charge transport in materials with disordered energy landscape is significantly influenced by the charge carrier density as discussed in Section 3.1.1. The electron-density dependent mobility can be probed by utilizing the field-effect transistor geometry. Due to the gate-voltage induced filling of tail states in the Gaussian density of states, charges can access more states at higher energy due to accumulation and, therefore, the mobility in organic disordered semiconductors is expected to increase with higher charge carrier density [27]. For moderate charge carrier densities, an increase of the mobility in organic semiconductors has been observed experimentally in FETs made of conjugated polymers [50, 119] and was proposed theoretically from the Master-equation approach [18, 99]. Surveying literature, the DOS in [60]PCBM [113, 124] and [70]PCBM [5] based FETs, so far, was assumed to be exponential as estimated from temperature dependent measurements between 300 K and 180 K. In contrast, the charge transport in [60]PCBM-based diodes [82], i.e., in the regime of low carrier densities, was described by the correlated Gaussian disorder model (CDM, see sec. 3.1.1). As the exponential DOS is a good approximation for the originally Gaussian DOS in the regime where the organic FET operates [27, 119], the finding of an exponential DOS in methanofullerene-based FETs was reconsidered in this work.

In analogy to former publications, increasing mobilities with higher charge carrier density n in PCBM-based transistors were measured in this work. In contrast to earlier works [113, 127], gate fields up to $2 \cdot 10^8 \, \frac{\text{V}}{\text{m}}$ were utilized, where a decrease of the mobility μ was observed. When a high fraction of states was occupied a maximum in μ was reached, which is in agreement with the extended correlated Gaussian disorder model (extended CDM), see Fig. 3.2(b). At higher electron densities, however, the mobility decreased again. Several potential artifacts were excluded, prior to discussing the physical origin of the mobility dependence on the charge carrier density.

These artifacts are:

- the leakage current through the insulator superimposing the drain current,

- the neglecting of derivative of the mobility (see Section 4.1.1),

- the contact resistance and

- the misestimation of the charge carrier density.

As the variance of the DOS is influenced by the interaction of charge carriers with the dipole field of the FET-dielectric, its effect on the mobility dependence on the charge carrier density

will be discussed below. Using the spatially resolved charge carrier density and applying the extended CDM, the experimental data were consistently expressed in the framework of the extended CDM. As the extended CDM parameterization is not strictly valid in the high electron density regime, an empirical fit for the mobility decrease is given, which is attributed to long-range Coulomb interaction.

Specific experimental details

Top contact devices with an additional organic insulator, i.e. polyvinylalcohole (PVA) were used, as shown in Fig. 5.1(c). The use of an PVA layer aims on the investigation of electron trapping often encountered on SiO_2 surfaces and the probing of energetic disorder at the semiconductor/insulator interface.

For the FET-structures with modified dielectric, an additional layer of PVA was spin coated from aqueous solution (3.6 mg/ml) on top of the SiO_2 in air. Subsequently, the substrates were heated to 150 °C in nitrogen atmosphere. This resulted in very smooth films ($R_{rms} \approx 1\ nm$) with a thickness around 220 nm. The thickness was determined separately for each layer with a Veeco Dektak 150 profilometer. The PCBM solution (1 wt.% in chlorobenzene) was spin coated at 1500 rpm for 60 s in N_2-atmosphere within a glovebox. Au, Al and Ca (50 nm) electrodes were vacuum-deposited in the case of top contact structures. The current–voltage characteristics were recorded under nitrogen atmosphere or in a vacuum chamber while exposure to ambient conditions during transfer from the glovebox was avoided. The dielectric constants ε_{diel} were determined by capacitance–voltage measurements using an Agilent E4980A LCR-meter. ε_{diel} was around 6 for PVA . For the mobility analysis the serial capacitance of SiO_2 and PVA was used, if applicable. The reproducibility of the electrical characteristics was provided by employing at least four different channel lengths for bottom contact and at least eight different channel lengths for top contact geometry. For each channel length several identical transistor geometries were prepared on one substrate while the results were also confirmed for structures built on different substrates. The channel length was measured by an optical microscope in order to avoid misestimation due to improper shadowing by the mask during evaporation of the metal electrodes. The difference between the nominal and the actual channel length can in some cases be as high as 50 μm, which could lead to overestimations of the mobility.

Alternatively to PVA, SiO_2-layers ($\varepsilon \approx 4$) as well as PPcB (polypropylene-co-1-butene, $\varepsilon \approx 2$) have been used in order to confirm the general effect of $\mu(n)$–data. Although good agreement with the $\mu(n)$ data obtained for PVA-based devices have been found, scattering of mobility data in FETs with SiO_2 dielectric was observed which was attributed to the surface energy mismatch of PCBM and SiO_2. Spin coating of PCBM solutions on top of SiO_2 surfaces results in worse filming properties as compared to the PVA dielectric. For the PPcB devices, polypropylene-co-1-butene (12 wt% 1-butene, Aldrich) was dissolved in anhydrous decaline (cis/trans mixture, Aldrich) (20 mg/ml) at 190 °C and spin coated in air on top of the SiO_2 surface using a preheated copper chuck. The device was heated for one minute at 200 °C in air and then transferred into the glove box. On the PPcB dielectric films lowered mobilities and high threshold voltages were observed. Hence, the accumulation of high carrier densities was suppressed by some mechanism. It should be noted that the attempts of using other organic dielectrics, such as polymethylmetacrylate (PMMA) and polystyrene (PS), that are soluble in chlorobenzene at room temperature as PCBM, were discarded due to obvious reasons.
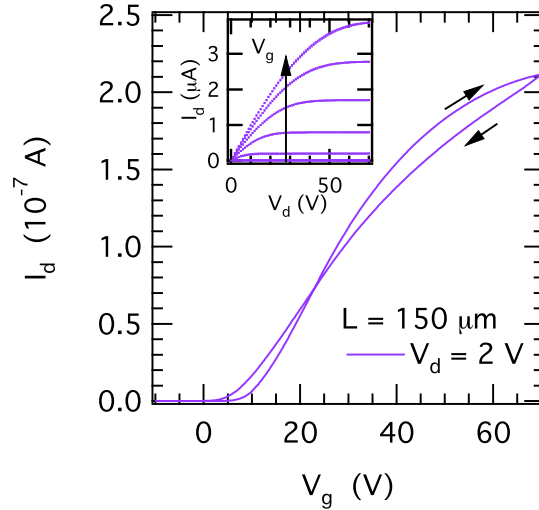
Abbildung 6.1: Generic transfer characteristics of a calcium tc-FET with a PVA dielectric (L=150 μm, W=2 mm). A small hysteresis can be observed due to charging. We observe a not strictly linear increase of I_d vs. V_g. Inset: the respective output characteristics exhibit linear onset of the current at low V_g.

Results

Similar current-voltage characteristics for top and bottom contact (Au, Al or Ca) field effect transistors based on [60]PCBM and [70]PCBM employing PVA (ε_{diel}=6) dielectrics were observed. The generic linear transfer characteristics of [70]PCBM with Ca source–drain contacts and PVA dielectric are shown in Fig. 6.1. A small hysteresis was observed which is attributed to charging of the sample. Although a linear dependence of accumulated charge density on V_g is expected the drain current increases not strictly linearly with the applied gate voltage. The maximum leakage current I_g through the dielectric ranges from 0.1% to 1% of I_d and can be excluded from causing artifacts. The inset of Fig. 6.1 shows the output characteristics, which indicates linear onset of the drain current at low V_d. It should be noted that unipolar hole transport was not observable.

Applying the 2D-approximation, the surface electron density n_{2d} was determined via

$$n_{2D} \approx \frac{1}{e} C_i V_g. \tag{6.1}$$

In Fig. 6.2 the electron mobility as derived from the linear regime is shown versus the carrier density n_{2D}. The room temperature measurements revealed a very similar dependence of the mobility on the charge carrier density for [60]PCBM and [70]PCBM, almost independent of the contact metal. A mobility increase up to a maximum value of $2 \cdot 10^{-2}$ cm^2/Vs at $1.5 \cdot 10^{12}$ cm^{-2} was obtained, which is in agreement with the predictions by the extended CDM. Nevertheless, at even higher densities the mobility was found to decrease. An effect which could cause the drop of the mobility at higher carrier densities is the neglection of the derivative of the mobility in Eq. (4.7). Therefore, the correction presented in sec. 4.1.1 was applied to the $I_d - V_g$ data in the linear regime. For a representative [70]PCBM sample on PVA-dielectric with Ca-top contacts the corrected mobility is indicated by the black full line in Fig. 6.4. The correction
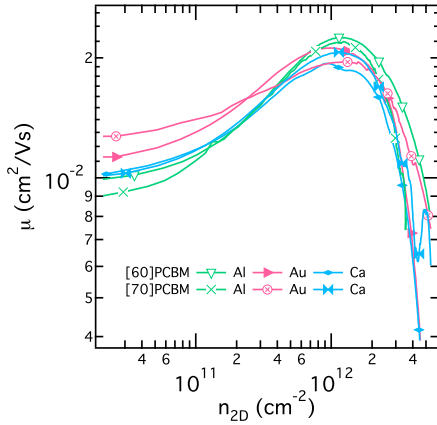
Abbildung 6.2: Mobility *vs.* charge carrier density of [60]PCBM and [70]PCBM. The mobility was derived from the slope of the transconductance. For all samples shown L exceeds $150\,\mu$m.
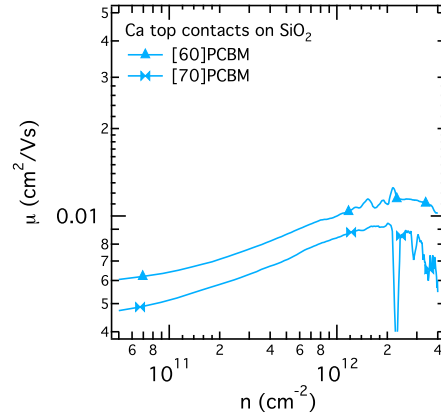
Abbildung 6.3: Mobility in [60]PCBM and [70]PCBM thin films with Ca top contacts on SiO$_2$ dielectric. For all samples L exceeds $150\,\mu$m.

does, however, not change the trend of reaching a maximum in n_{2D}. Note that this method does not allow for a contact resistance correction.

The contact-resistance correction was performed by applying the transmission-line method as presented in sec. 4.1.1. The total resistance versus channel length for [70]PCBM on PVA with calcium top contacts is shown in Fig. 6.5. The contact resistance R_c (Fig. 6.6) was determined from the intersection of the linear fit at constant gate voltage with the *ordinata*. R_c decreases with increasing gate voltage, which supports the injection of electrons, especially in top contact structures. As shown in Fig. 6.4 the contact resistance has almost negligible influence on the mobility and was therefore neglected, in particular due to the very similar μ *vs.* n_{2D} data measured for different contact metals.

As discussed in Section 3.2, the charge carrier density within the channel is rather a three-dimensional quantity than simply described by the surface charge density n_{2D} in Eq. (6.1). Moreover, the accumulated charge may be significantly influenced by the energy distribution of electronic states [93]. In contrast, a linear dependence of the charge carrier density on the gate voltage is assumed for derivation of the mobility, which could lead to misestimations.

Accordingly, the relation between n, V_g and the distance z from the dielectric had to be found: The Fermi-integral for a Gaussian density of states has been solved for electrons and holes followed by the solution of Poisson's equation at the semiconductor–insulator interface. Details can be found in section 3.2.

The flat-band voltage V_{FB} has been set to zero, different values of V_{FB} do not dramatically change the picture as the I_d–V_g-data were corrected for the threshold voltage. N_A^+ was set to $1 \cdot 10^{21}$ m^{-3}, accounting for impurity doping of the material. This was chosen due to the fact that organic semiconductors are expected to be unintentionally impurity-doped and also, this procedure provides comparability to Refs. [93, 119]. In Fig. 6.7 the surface-charge density derived from the simple method in Eq. (6.1) is compared to the surface-electron density derived from the solution of the Poisson equation. The overall behavior of the charge carrier density, shown
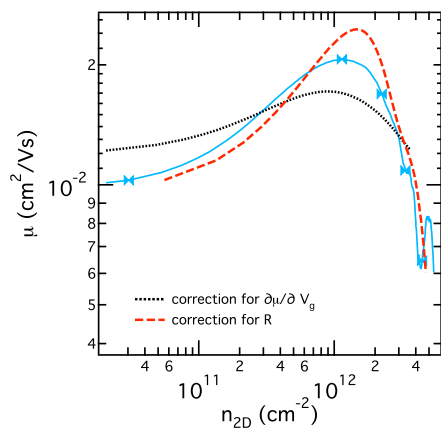
Abbildung 6.4: Two different correction methods were applied for the [70]PCBM sample with calcium top contacts on PVA dielectric.
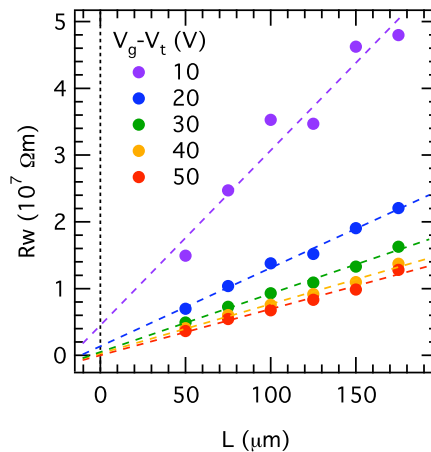

Abbildung 6.5: Total resistance of [70]PCBM field-effect transistor with calcium top contacts *vs.* channel length
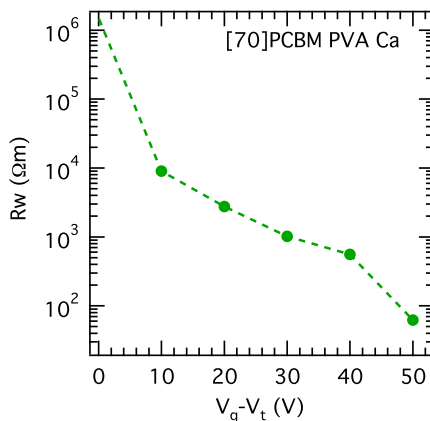

Abbildung 6.6: Total resistance of [70]PCBM field-effect transistor with calcium top contacts *vs.* the effective gate voltage
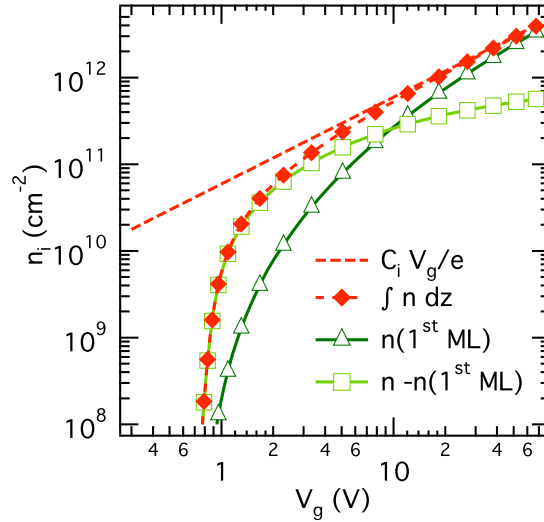
Abbildung 6.7: Electron density per unit area n_i as a function of V_g: The dashed line represents the charge carrier density as usually derived from the capacitance, i.e Eq. (6.1). The diamonds reflect the projection of the three-dimensional electron density of the layer to the surface. The triangles indicate the projected charge carrier density within the first monolayer, squares indicate the total projected charge carrier density subtracted by the charge carriers within the first ML. Calculations were carried out according to Section 3.2 for the SiO$_2$/PVA dielectric using σ=65 meV, ε_{sc}=4, N_A^+=1· 10^{16}cm^{-3}.

as a red dashed line, and the effective surface charge Q_s (red diamonds) does not dramatically change. Note, that experimentally only mobility data for $V_g >2$ V can be accessed due to the requirement $V_d < V_g$. Nevertheless, a difference of the areal electron densities at gate voltages $\lesssim 1$ V was found which is attributed to the filling of tail states and compensation of acceptor levels. At low V_g the supplied energy is not sufficient to excite charge carriers into the LUMO, while at higher charge carrier densities $C_i V_g/e$ and n coincide. The integration of the electron density within the first monolayer, $n(1^{st}$ ML$)\int_0^a ndz$ can be compared to the free electron density which is not located within the first monolayer, i.e. spread over the bulk, $n - n(1^{st}$ ML$)$. Concisely, due to the large screening length at low charge carrier densities, the carriers are almost homogeneously distributed over the sample at low V_g, while at higher densities (and larger V_g) most of the accumulated charges are found within the first monolayer.

Although the charge carrier density can be determined locally from numerical simulations the experiments are of integral nature and result in the total drain current:

$$I_d = W \cdot \frac{V_d}{L} \int n(z)\mu(n(z))dz. \tag{6.2}$$

Neglecting the dependence of the mobility on the charge carrier density to the first order, the mobility can be derived from the experimentally determined current and the charge carrier density deduced from the solution of the Gauß–Fermi integral and the Poisson equation via

$$\mu(n) \approx \frac{L}{WV_d} \frac{\partial I_d}{\partial (\int ndz)}. \tag{6.3}$$
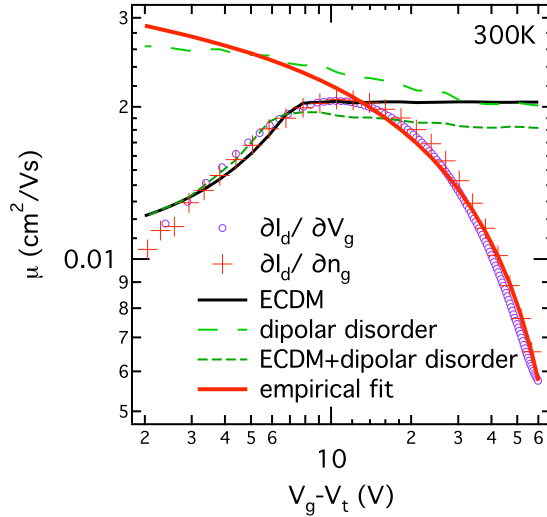
Abbildung 6.8: Electron mobility in [70]PCBM at 300 K: from experimental data using Eq. (4.7) ($\partial I_d / \partial V_g$), mobility from experimental current derived by the charge carrier density from the Poisson equation using Eq. (6.3) ($\partial I_d / \partial n_i$), from the extended CDM using $n(z)$ from Poisson equation, with dipolar disorder broadening and the combination of extended CDM and dipolar disorder broadening. The red line shows the empirical fit of μ at high n using Eq. (6.6), also in Fig. 6.11.

The resulting mobility is indicated by the red crosses in Fig. 6.8. An almost negligible shift of the mobility compared to the derivation of the drain current for the gate voltage (purple symbols) was observed, as Eq. (6.3) is a rough first order estimate. In order to confirm the suggestion that the charge transport in PCBM is described by the energy correlated disorder model, the spatially distributed mobility $\mu(n(z))$ was derived with the extended CDM (Section 3.1.1) and fitted to the experimental data using the derivative of Eq. (6.2). The black full line in Fig. 6.8 indicates the mobility *vs.* charge carrier density at 300 K. The data can be well described for moderate charge carrier densities. Nevertheless, the authors of Ref. [18] did not give a parameterization for carrier densities exceeding 2.5 % occupation of the DOS. The authors mentioned that the simulation might not be strictly valid in the high carrier density regime due to the disregard of long-range Coulomb interactions and carrier transitions further than to the third next neighbor.

Another effect which can cause the decrease of μ is the dipolar-disorder broadening of the DOS induced by the dielectric: Charge carriers interact with the dipole field established by the insulator. The probability for this interaction was calculated using Poisson statistics and the width of the broadened Gaussian DOS in dependence on z was derived, according to Richards *et al.* [103]. In the latter reference a good description of the decreasing mobility data via dipolar-disorder broadening of the DOS induced by the dielectric has been demonstrated. As shown in Fig. 6.7, the charges are distributed over the sample at low V_g, while the main part of charges can be found within the first monolayer at high gate voltages. Therefore, the broadening of the DOS at the interface will have the most pronounced impact on the mobility at high V_g. Although no dependence of $\mu(n)$ on ε_{diel} could be observed, a description of the data according to the analytical model was approached.

For a dipole strength of 2D and a monomer density of PVA of $10^{27} \cdot m^{-3}$ the broadening of σ as a function z is shown in Fig. 6.9. The variance of the DOS is broadened in the vicinity of
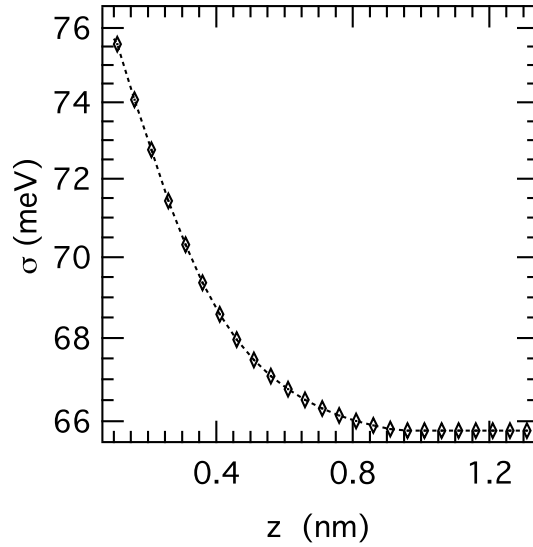
Abbildung 6.9: Dipolar disorder broadening caused by the dielectric, calculated according to [103] using ε_{sc}=4, ε_{ins}=6, σ=65 meV in the bulk, dipole strength of 2D and a monomer density of PVA of $10^{27} \cdot m^{-3}$.

the interface and amounts to around 76 meV. At a distance $z \approx 1$ nm the width approaches its original value of σ=65 meV in the bulk.

Assuming only the dependence of μ on σ, as suggested in Ref. [103], the mobility can be calculated via $\mu(z) \propto \exp(-(c\sigma(z)/k_B T)^2)$. Following this approach, a monotonic decrease of μ vs. n was observed, as shown in Fig. 6.8. At low V_g, the electrons are spread over the sample, while at high gate voltages, a larger portion of the accumulated charge carrier density is near the dielectric which is an effect of the screening length $L \propto \sqrt{n^{-1}}$. Hence, dipolar-disorder broadening will have the most pronounced effect at high V_g and the mobility is lower compared to low V_g. A point which was neglected in Ref. [103] is, though, the dependence of the mobility on the charge carrier density. Although a higher value of σ diminishes the mobility within the first monolayer, the higher charge carrier density near the dielectric should, in turn, increase the mobility. Therefore we combined $n(V_g, y)$ with the broadened $\sigma(z)$ and the parameterization given in Ref. [18]. Although the mobility saturates at high n as a result of the extended-CDM-parameterization, the broadening of the DOS is not sufficient to describe the pronounced decrease of μ, as illustrated in Fig. 6.8. This is also the case, if one assumes large differences between the dielectric constants of the semiconductor and the dielectric.

At low to moderate carrier densities, the room temperature data were well described by the extended CDM. A saturation of the mobility at n above 2.5% occupied states and even a slight decrease of μ was found in the framework of the respective model [18]. The applicability of the model for the description of the charge transport in PCBM needs to be verified by temperature-dependent mobility measurements.

Within the framework of the extended CDM, the width of the Gaussian DOS σ at low carrier densities can be estimated from

$$\mu_0(T) = \mu_0 c_1 \exp\left(-0.29\hat{\sigma}^2\right), \tag{6.4}$$

where $\mu_0 c_1$ is a temperature-independent prefactor which scales with the Miller–Abrahams transition rates and therefore with the attempt-to-escape frequency ν_0. The mobility at different temperatures and $V_g - V_t$ is shown in Fig. 6.10. $\ln\mu$ *vs.* T^{-2} plots indicate two distinct temperature regimes with transition at T=160 K. The width of the Gaussian DOS σ estimated by using Eq. (6.4) amounts to 65 meV in the high-temperature regime and 34 meV in the low-temperature regime. At higher carrier densities, the temperature dependence of $\mu_0(T)$ gets superimposed with a carrier-density dependence as described in Section 3.1.1.

$$(6.5)$$

In the experiments the maximum of the mobility for varying temperature remains nearly at the same charge carrier density, as shown in Fig. 6.11, which indicates the applicability of the enhanced CDM to the experimental data.

The temperature dependent data were fitted to the enhanced CDM employing the spatially resolved charge carrier density $n(z)$. The best temperature-dependent fits of the experimental $\mu(T,n)$–data to the extended CDM parameterization were achieved by using σ=65 meV and a=3 nm. Additionally a temperature dependence of $\mu_0 c_1$ was allowed for, which is reasonable as $\mu_0 c_1$ scales with the attempt-to-escape frequency (see Fig. 6.12). Using Miller–Abrahams transition rates ν_0 is temperature-independent, while a temperature dependence is established in Marcus theory [76] (see Eq. (3.24)).

Fig. 6.11 shows the experimental data and the fits at different temperatures. Good agreement between the extended CDM and the experimental data was found at low gate voltage and even the saturation of the mobility could be described. At high n $\mu(n)$ remains constant within the parameterization, although actually a decrease was observed in Ref. [18]. This agrees with our finding of a significant decrease of μ at high carrier concentrations.

Discussion

The electron mobility of [60]PCBM and [70]PCBM was found to be very similar and independent of the injecting metal, which is consistent with room-temperature data in Ref. [127]. Annealing the samples to 400 K in vacuum did neither change the electron mobility nor it induced hole transport. This observation holds for different contact metals as well as for the used dielectrics. In contrast, hole transport upon vacuum-annealing was observed by Anthopoulos *et al*. [6]. A decreasing mobility at high charge carrier densities was observed which in general agrees with the findings by Bouhassoune *et al*. [18], although no parameterization was given for high densities. Assuming that the decrease at high n can be described as a function of the average free-electron distance $r = 1/\sqrt{n_{2D}}$, the data can be described by the empirically found relation as indicated in Figs. 6.8 and 6.11,

$$\mu = \mu_0 \exp\left(-\frac{4}{5}\hat{\sigma}^2\right)\left(1 - 2\frac{a}{r}\right), \qquad (6.6)$$

with μ_0 is $3.2 \cdot 10^{-1}$ cm^2/Vs. At low temperatures, μ_0 must be slightly enhanced by a factor of five. The temperature-dependent mobility above 160 K reveals a width of the Gaussian DOS being σ around 65 meV in the framework of the enhanced CDM, which agrees with activation energies around 150 meV reported in literature [5, 113, 124]. The result is in agreement with Ref. [82] in which the temperature dependent mobility in PCBM diodes was interpreted in the
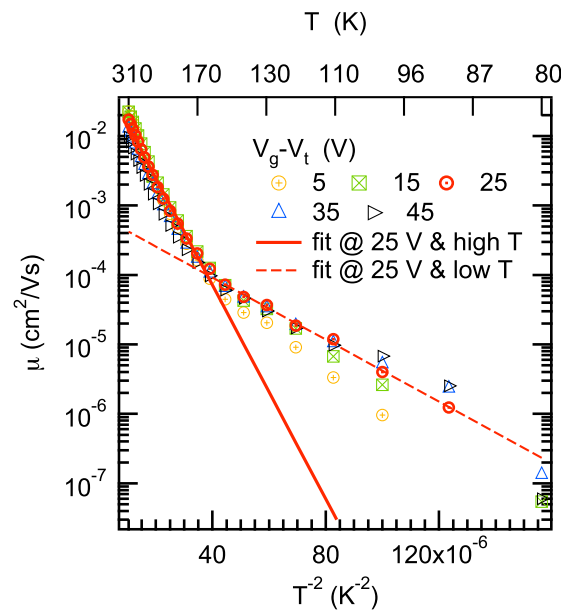
Abbildung 6.10: Charge carrier mobility *vs.* T^{-2} at several $V_g - V_t$, as indicated by the legend. The graph shows the representative data for different device geometries. Selected is a [70]PCBM sample with calcium top contacts
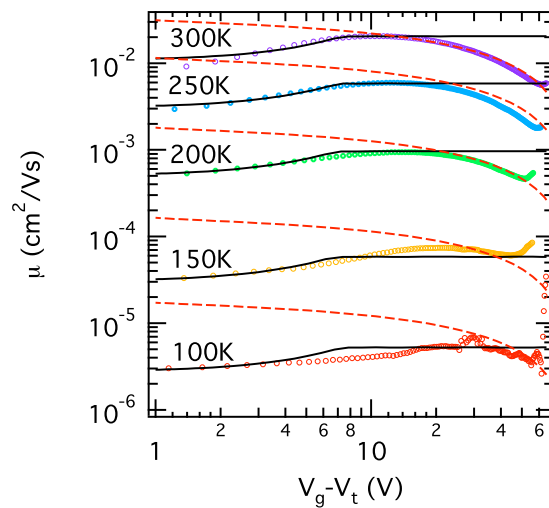

Abbildung 6.11: Mobility *vs.* gate voltage of the [70]PCBM sample with Ca top contacts as derived from Eq. (4.7) (circles) and fits resulting from the derivative of Eq. (6.2) (full line) at various temperatures as indicated by the legend. The dashed lines correspond to empirical fits to the high density range according to Eq. (6.6)
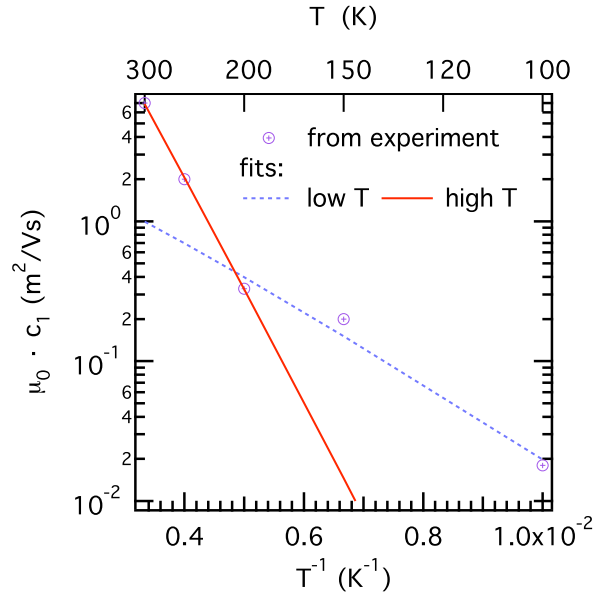
Abbildung 6.12: Prefactor for the temperature dependent mobility in Fig. 6.11 and fit according to $c_1 \propto W_{ij}$ from Eq. (3.24)

framework of the CDM [89]. In the low-temperature range below 160 K we observe a different value for σ of around 34 meV which was not reported in literature so far for methanofullerenes. The effect is attributed to two different transport regimes, thermally activated hopping at high temperatures and thermally assisted tunneling at low temperatures. Different temperature regimes were also found for small molecules [54] and for polymers [126]. In the low to medium electron-density range well up to $n_{2D} \approx 2 \cdot 10^{12}$ cm^2/Vs, the mobility data can be well described by the enhanced CDM, although the prefactor of the temperature-dependent mobility had to be varied. We attribute this to the assumption of temperature-independent attempt-to-escape frequencies ν_0 in the enhanced CDM using Miller–Abrahams transition rates, while a temperature dependence is established in Marcus theory [76]. The lattice constant a within the parameterization was set to 3 nm. As a should be considered as an effective hopping distance [99] this is in satisfying agreement with our experimental data and the findings on PCBM diodes in Ref. [82].

Summary

[60]PCBM and [70]PCBM exhibit comparable mobility values which are almost unaffected by the source–drain metal and dielectric. The mobility exhibits a maximum of $2 \cdot 10^{-2}$ cm^2/Vs. Several artifacts as well as dipolar-disorder broadening in the vicinity of the dielectric were excluded from causing the subsequent mobility decrease at high carrier densities. The temperature-dependent measurements reveal two different transport regimes, above and below 160 K. The width of the Gaussian DOS σ amounts around 65 meV in the high temperature range and around 34 meV in the low temperature range. The data could be described by the extended correlated Gaussian disorder model in the low to medium electron density regime with σ=65 meV for the entire temperature range when using polaronic transition rates.

6.2 Charge Transport in Al-Doped Nanocrystalline ZnO *

In crystalline semiconductors, doping usually lowers the mobility due to the enhanced ionic scattering [35]. In contrast, a mobility enhancement due to doping in poly- and nanocrystalline ZnO systems at high doping levels has been reported [10, 92, 108], which was attributed to a reduction of the barrier height located at the crystallite–crystallite interface (see Section 3.1.2). Doping has also a strong influence on the crystallite size [100, 107]. The simulations of charge transport within field effect transistors performed in Ref. [57] ascertained the influence of the grain boundary density on the charge carrier mobility.

By extrinsic doping of ZnO nanoparticles one can increase the net free carrier density of the material, which allows for control of the electrical conductivity and partial compensation of acceptor-like defect levels, retaining the advantages of the processability at the same time.

In bulk ZnO, aluminum acts as an electron donor and introduces an allowed energy state just below the conduction band energy. The thermal release of electrons into the conduction band leads to an increase of the charge carrier density and, consequently, the electrical conductivity. The electrical transport properties of ZnO are commonly investigated by four probe conductivity technique as well as by Hall-effect measurements [1, 73, 100, 104, 107].

In this work, the structural and electrical transport properties of the sol–gel processed nanocrystalline ZnO with variable doping level was investigated by using X-ray diffraction (XRD), scanning electron microscopy (SEM) and field-effect transistor (FET) measurements. In contrast to the traditional techniques used for mobility determination, the use of FET-structures provides a tool to determine the mobility, the conductivity and the charge carrier density. A further, and for this thesis decisive advantage lies in the variation of the charge carrier density at a constant defect density. The influence of charge carrier density achieved by extrinsic substitutional doping and by the gate-induced accumulation of charges on the mobility will be compared. This section reports on the investigation of nc-ZnO:Al in terms of doping- and carrier-density-induced variation of the electron mobility and the structural properties.

Specific experimental details

The bottom contact field effect transistors with 200 nm SiO_2 dielectric with Ti/Au source–drain metals were prepared according to the layer setup as depicted in Fig. 6.15(b). After applying the nc-ZnO:Al from solution via spin coating, the samples were sintered at 500°C in order to improve the particle–particle cohesion and to remove residual organic impurities which could establish detrimental structural and electronic effects. film thickness of nc-ZnO:Al was about 25 nm and does not significantly vary with doping level. The film thickness was determined using a Profilometer (Dektak 150).

The X-ray analysis of nc-ZnO:Al was carried out with a XRD spectrometer (Philips PW 1729) using the Cu-K_α line. As SiO_2 exhibits XRD-signatures close to or coinciding with the Wurtzite reflections, we investigated samples cast on amorphous glass substrates. In order to get a good signal to noise ratio, thicker nc-ZnO:Al layers as in the SEM and FET studies were employed. This was achieved by sequentially applying the nanoparticle solution five times. The
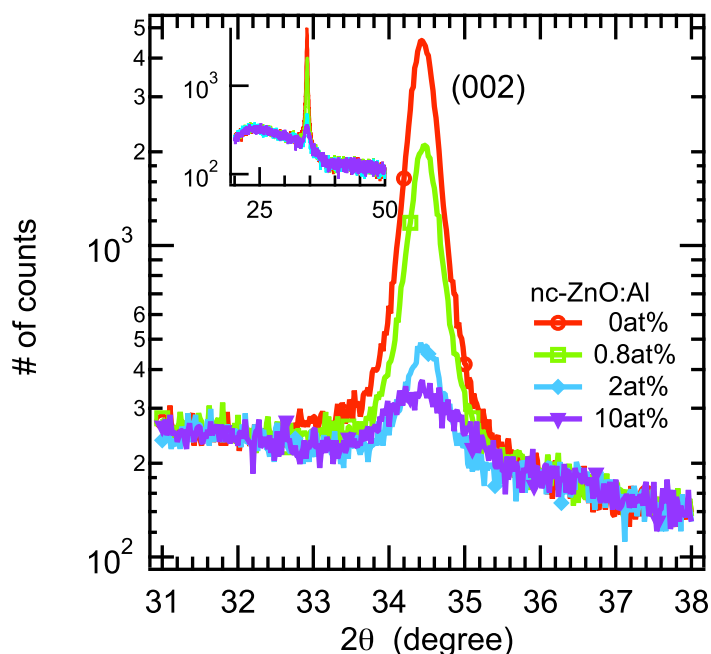
Abbildung 6.13: X-ray diffraction pattern of nc–ZnO:Al with varying doping level as indicated by the legend. Inset: XRD-pattern shown for the full range of the diffraction angle. It is clearly seen, that except the (002)-reflections there is no other indication evolving from the noisy background of the substrate

Tabelle 6.1: Average crystallite sizes of undoped and variedly Al–doped nc-ZnO estimated from XRD spectra using the Debye-Scherrer formula.

	0 at%	0.8 at%	2 at%	10 at%
size/nm	20.8	19.6	15.0	7.2

sample was heated to 300°C after each spin coating step to remove MEA from the layer, to avoid inclusions of carbon compounds in the nc-ZnO film. Moreover, the intemediate annealing steps allow densification of the films in order to prevent dissolution during cast of the subsequent coatings. Subsequently, the sintering step at 500°C was applied. The thickness of the entire film was around 120 nm and it was almost independent of the doping level.

Structural analysis

In order to determine the structure and orientation of the nanocrystals XRD measurements were carried out . The XRD spectra (Fig. 6.13) show only one peak corresponding to the orientation along the c-axis of the Wurtzite structure. Other peaks resulting from different orientations of the nanoparticles on the substrate are not observable as indicated by the inset in Fig. 6.13. This indicates that the particles are highly oriented on the substrate. Depending on the doping level, the maximum of the (002) peak decreases while the FWHM becomes larger. An estimation of the nanocrystallite size was done by using the Debye-Scherrer formula $\Delta(2\theta) = (0.94\lambda)/(l \cdot \cos\theta)$,
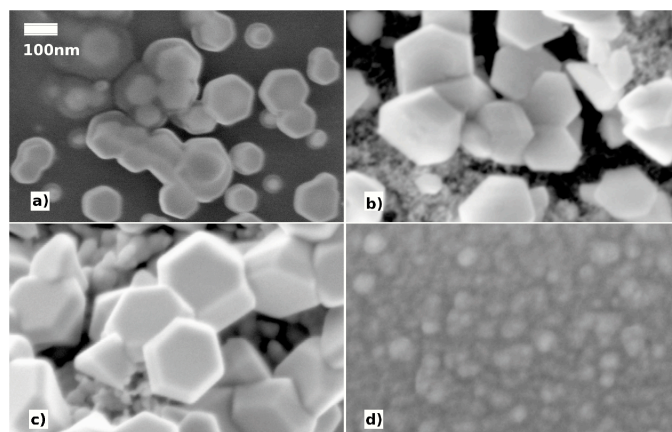
Abbildung 6.14: SEM micrographs taken with 3 kV acceleration voltage using the inlens detector. The images give a clear indication of the hexagonal structure and c-axis orientation of the undoped and variedly doped nc-ZnO: a) 0 at%; b) 0.8 at%; c) 2 at%, d) 10 at%. Note that the surface roughness is varied upon doping. Highly n++-doped Si:Sb/SiO$_2$ was used as substrate.

where l is the particle diameter, λ the X-ray wavelength, $\Delta(2\theta)$ the full width at half maximum of the peak and θ the peak maximum position [62]. A shrinking from about 20 nm in the undoped case to about 7 nm for the highest doping level is found as summarized in Table 6.1. Although the estimation of the particle size at the highest doping level is less accurate due to the low peak intensity and the large peak width, the tendency of a decreasing crystallite size with increasing extrinsic doping level is clearly visible.

The XRD spectra provide evidence of the average crystallite size, but the sintering-induced linking between particles is important to establish continuous pathways for the charge transport. Indeed, the sintering was successful for 0 at%, 0.8 at%, 2 at% and to a lesser extent for 10 at% doping, as demonstrated by the SEM micrographs in Fig. 6.14. The particles also exhibit a hexagonal geometry, which is a clear indication of the c-axis orientation. It is worth noting that the SEM images in Fig. 6.14 show large hexagonal particles with diameters >100 nm. Though this is contradictory to the particle size estimation from the FWHM of the XRD-signatures, one should keep in mind, that the dominant presence of small crystallites will obscure the narrow reflection peaks of large domains in the XRD patterns. Also note that one particle can consist of several crystallites.

Characteristics of undoped nc-ZnO

The field effect transistor geometry provides a way to determine the charge carrier mobility for various carrier densities without affecting the defect density. A sketch of the used device structure is shown in Figure 6.15. The output and the transfer characteristics of the nominally undoped sample (Fig. 6.15) indicate the effect of charge accumulation due to the applied gate potential V_g. The output characteristics (Fig. 6.15(a)) show the drain current I_d *vs.* drain voltage V_d for several constant gate voltages V_g. The output characteristics reflect the transistor performance for the *n*-conducting case at positive V_g. There is no significant injection barrier at the gold/nc–ZnO interface, as can be seen from the ohmic behavior at small V_d. The charge carrier mobility was determined from the transfer characteristics I_d *vs.* V_g at a constant source–drain
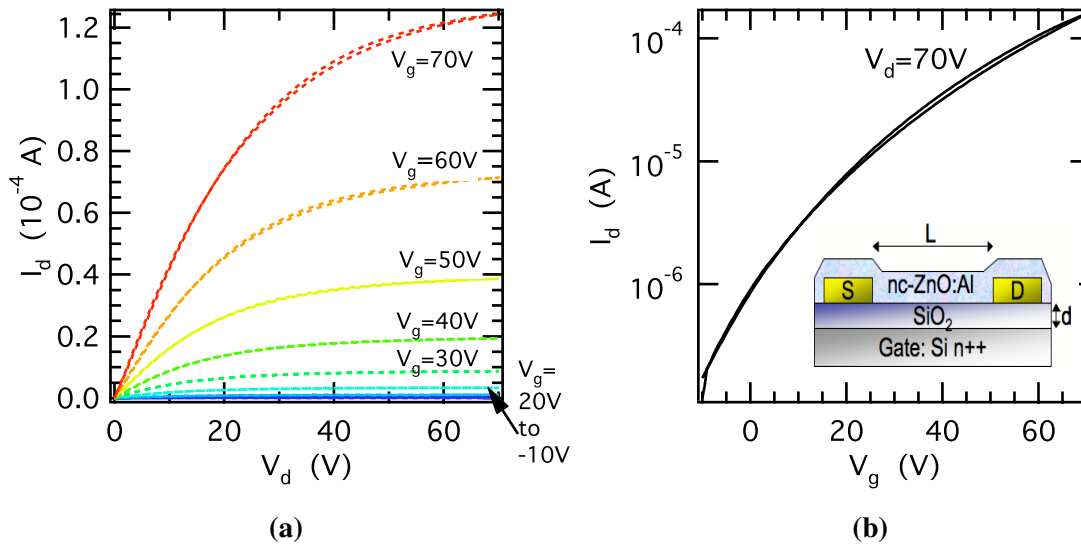
Abbildung 6.15: FET characteristics of undoped nc-ZnO at T = 300 K: 6.15(a)) Output characteristics: I_d–V_d in dependence of V_g as indicated by the legend and by the color scale. 6.15(b)) Transfer characteristic I_d–V_g at V_d=70 V and schematic of the FET device (d: thickness of the dielectric). Transistor details: L=160 μm, Au bottom contacts (Caribou structure) on SiO$_2$ dielectric.

voltage of 70 V (Fig 6.15(b)). The charge carrier depletion of the channel due to decreasing gate voltage usually results in a constant low level drain current, the off-current. In the *n*-conducting case, one estimates the off-current at low gate voltages. In the present study, a rather high off-current was observed, pointing at a high charge carrier concentration being initially present in the channel as a result of unintentional doping. In the following, the focus lies on the effect of extrinsic doping on the charge transport, i.e., the conductivity, free charge carrier density, mobility and also the mean barrier height at the nanocrystallite interface.

Conductivity and Charge Carrier Density   The conductivity σ_{el}, the free charge carrier density n and the mobility μ are related via

$$\sigma_{el} = en\mu, \tag{6.7}$$

where e is the elementary charge. Appropriate extrinsic doping is supposed to cause thermally activated free charge carriers and, accordingly, a higher conductivity is expected as long as the mobility remains unaffected.

In order to estimate the values of σ_{el} and n, $I_d - V_d$ characteristics were recorded at zero gate voltage in the linear regime, i.e., at low drain voltages. σ_{el} was extracted using Ohm's law $\sigma_{el} = j/(V_d/L)$, where j is the current density. j results from I_d normalized for the contact area, which is the product of the channel width W and the minimum thickness of the transport layer or the injecting electrode, amounting to 20 nm in our case. Fig. 6.16 shows the values of σ_{el} (circles) for the undoped and the differently Al-doped nc-ZnO. The conductivity of the nominally undoped nc-ZnO was found to be $1.8 \cdot 10^{-2}$ Sm^{-1}. σ_{el} reaches a maximum of $3.4 \cdot 10^{-2}$ Sm^{-1} at 0.8 at% doping level. The conductivity derived for the high doping level approaches the value of the nominally undoped material with $1.8 \cdot 10^{-2}$ Sm^{-1}.
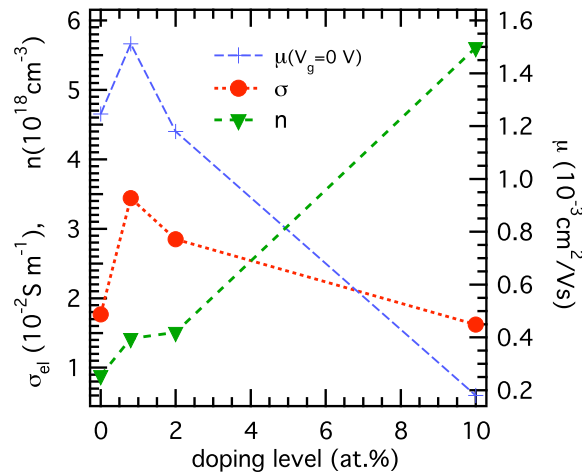
Abbildung 6.16: Electrical conductivity (circles), free charge carrier density (triangles) and electron mobility (crosses) *vs.* doping level of zinc oxide nanoparticles at T=300 K; dashed lines: guides to the eye.

The field-effect mobility, which will be addressed in detail in the next paragraph, and the conductivity have been used to calculate the free charge carrier density using Eq. (6.7). The extracted values for *n* are shown in Fig. 6.16 (triangles). The free charge carrier density increases with the extrinsic doping concentration from $8.9 \cdot 10^{17}$ cm^{-3} to $5.6 \cdot 10^{18}$ cm^{-3}. Note that for a thin layer, the determination of the free charge carrier density is restricted to the electrical characterization of nc-ZnO. Optical methods, such as infra-red reflection-spectroscopy, require a film thickness largely exceeding the screening length in order to estimate the plasma-frequency. Moreover, as a relatively high density of carrier scattering centers enhances the damping term, infrared reflection spectra (not shown) exhibit an ambiguous decrease with increasing frequency of the impinging light ray.

Mobility Here, the focus lies on the effect of free charge carrier density on the electron mobility, as a results of both, accumulation as well as extrinsic doping.

Channel length of L=160 μm were chosen since in this case the channel resistance was found to sufficiently exceed the contact resistance, so the electrical characteristics are dominated by the channel properties. Consequently, the linear and saturation mobility are almost identical (not shown). The presented mobility data were derived from the saturation regime.

As it was not possible to determine the off-current of the transistor, the threshold voltage V_t could not be extracted. V_t was therefore neglected in Eq. (4.8), noting that this can imply a misestimation of the intrinsic and doping-induced charge carrier density, respectively. However, the general dependence of the transport parameters remains unchanged as the doping-induced variation in n, which directly contributes to V_t, is on a much smaller scale than the variation observed in the accumulation mode (Fig. 6.17).

In order to estimate a three-dimensional charge carrier density within the channel, it is assumed that accumulation takes place within the first two nanometers as a result from the Debye-screening length discussed in Section 3.2, i.e. $d_{acc} \approx 2$ nm. The charge carrier density resulting from the field effect measurement, n_{acc}, can then be determined from $n_{acc} = C_i (q d_{acc})^{-1} V_g$.
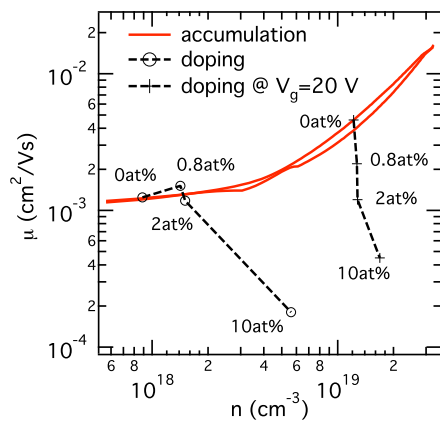
Abbildung 6.17: Electron mobility *vs.* charge carrier density at T=300 K. Solid line: increasing mobility due to accumulation within the field effect channel. Symbols: FET mobility *vs.* doping: Circles correspond to V_g=0 V, crosses to V_g=20 V, dashed lines: guides to the eye. Note: forward and backward accumulation directions show little charging effects. The variation of the entire charge carrier density (see text) due to doping is smaller than due to the field effect accumulation.

Abbildung 6.18: Temperature dependent mobility data of undoped nc–ZnO (crosses) taken at various V_g as indicated by the legend. The solid lines represent fits according to Eq. (6.10). Two different transport regimes at high and low temperatures can be distinguished. (high T: Dominant thermionic emission, Low T: Dominating field emission)

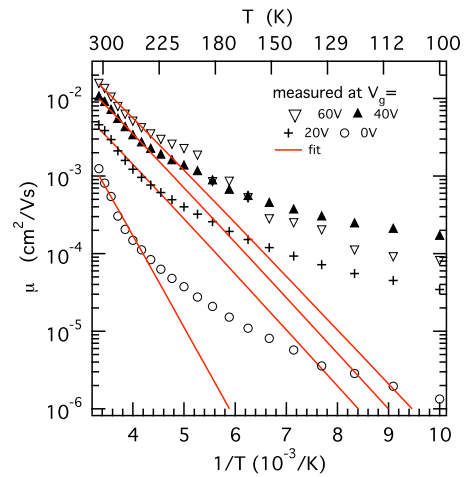Note, that the assumed accumulation layer of 2 nm is a rough estimate as the screening length depends on the charge carrier density and, hence, on the dopant concentration [111]. Since the charge carrier density varies only on a small scale due to doping, as compared to the variation due to accumulation, the misestimation of n due to doping in (Fig. 6.17 is around $2 \cdot 10^{17}$. Furthermore, additional free charge carriers have been accounted for, as a total free charge carrier density was calculated, which has its origin in doping *and* accumulation, i.e., the initial intrinsic and extrinsic charge carrier densities were added to get the entire free charge carrier density in the channel.

The mobility *vs.* charge carrier density plot (Fig. 6.17) indicates that accumulation of charges within the undoped nc-ZnO results in an electron mobility increasing by more than one order of magnitude from $1.3 \cdot 10^{-3}$ cm^{2}V^{-1}s^{-1} to $1.5 \cdot 10^{-2}$ cm^{2}V^{-1}s^{-1}. This is consistent with findings of Hossain *et al.* [57] who simulated grain boundary barrier modulation within ZnO-FETs and concluded that an increasing gate voltage leads to a barrier height lowering.

Since doping leads to an increased charge carrier density, resulting in a higher mobility with increasing doping level similar to the effect of accumulation is expected. For clarity, the field effect mobility at various doping levels at $V_g = 0$ V and $V_g = 20$ V are presented in Fig. 6.17. The variation of the mobility at $V_g = 0$ V is also indicated by the circles in Fig. 6.16. For $V_g=0$ V, the charge carrier mobility is slightly higher at 0.8 at% as in the undoped case. In contrast, at $V_g=20$ V, μ monotonically decreases with raising extrinsic doping level from $4.6 \cdot 10^{-3}$ cm^{2}V^{-1}s^{-1} to $4.5 \cdot 10^{-4}$ cm^{2}V^{-1}s^{-1}. The decrease is attributed to doping-induced disorder and scattering of electrons due to increased density of ionized dopants. The simulations in Ref. [57] indicate that the mobility is exponentially lowered with the number of grain boundaries within the transistor channel and therefore with decreasing particle size. Our experimental data indeed reveal an exponential relation between the mobility at $V_g=20$ V and the doping level (not shown). As the mobility is not only determined by the crystallite size and disorder, but also by scattering events, such as electron–electron and electron–ion scattering, it is not possible to give an explicit dependence between the crystallite size and the mobility.

Potential barriers at the crystallite boundaries In order to investigate the charge transport in regard of the internal structure of the semiconductor film in more detail, temperature dependent mobility measurements were performed. Fig. 6.18 exemplarily shows the mobility of undoped nc-ZnO at various V_g. The electron mobility in the nanocrystalline material consists of the contributions from the bulk of the crystallites and from the interfaces between the crystallites, as discussed in Section 3.1.2. If thermally activated hopping across the energy barriers between the crystallites is the dominant transport limiting factor in nc-ZnO [65], the potential barrier height ΔE can be quantitatively derived from temperature-dependent mobility data using

$$\mu(T) = \mu_0 \exp\left(-\Delta E / k_B T\right) \tag{6.8}$$

where the mobility prefactor $\mu_0 = \nu_0 T^{-1/2}$ with ν_0 being temperature independent. The behavior results from thermionic emission over isotype heterointerfaces [108] .

Two different slopes for the full temperature range were observed and attributed to different transport regimes. Usually, the high temperature regime is assigned to thermionic emission over the barrier, whereas at low temperature thermally assisted tunneling is dominant [92]. As the latter mechanism involves thermally activated tunneling, a lower activation energy is anticipated as charge carriers directly pass through the barrier. The activation energy evaluated in the high

temperature regime, can then be related to the other parameters, such as the conductivity, charge carrier density, and mobility, derived at 300 K.

Fig. 6.19 shows the activation energy ΔE *vs*. carrier concentration in the high temperature regime. For the undoped material, the activation energy monotonically decreases with increasing carrier density has been observed. Doping also results in a decrease in ΔE up to a doping level of 2 at%, in the case of V_g=0 V as well as V_g=20 V, which suggest that the same effect is responsible here. At the highest doping level of 10 at%, however, a higher potential barrier of 95 meV (V_g=20 V) and 113 meV (V_g=0 V), is present, which is ascribed to the influence of structural disorder.

Mean free path   As discussed in Section 3.1.2, the mean free path within the crystallites can be estimated from μ_0, i.e. the extrapolation of the temperature-dependent mobility to infinite temperatures. Here, the thermionic emission over the grain boundary can be excluded from limiting the transport. The variation of μ_0 with the carrier concentration is shown in Fig. 6.20. For the undoped material, μ_0 is decreasing from 214 $cm^2V^{-1}s^{-1}$ to around 5 $cm^2V^{-1}s^{-1}$ with increasing charge carrier density due to scattering at impurities and structural lattice pertubations. Doping of nc-ZnO results in a tremendous decrease of μ_0 by 2 orders of magnitude. The increasing charge carrier density due to accumulation in the doped samples further decreases the zero mobility by an order of magnitude. The mean free path of the electrons is directly proportional to the mobility and indicated by the right axis in Fig. 6.20. The mean free path in the undoped material is roughly one nanometer and decreases with increasing charge carrier density. The decrease is more pronounced in the case of doping due to additional structural or ionic defects.

Discussion

The experimental results presented in this section indicate that extrinsic doping influences the electrical parameters of the nanocrystalline ZnO in a complex way. In the following, this will be discussed in the context of charge carrier density variation superimposed by crystallite size modification and structural disorder.

The analysis of the XRD spectra indicates a significant decrease in the (002) peak height with increasing doping level, which can be explained by the additional disorder and a gradual transformation of the material to the amorphous phase, induced by the high amount of dopants in the material. Analysis of the spectra with the Debye-Scherrer method indicate that the crystallite size decreases with increasing doping level, resulting in a higher density of grain boundary. In contrast, the maximum particle size, as seen with SEM, is increasing up to a doping level of 2 at%. Note that the discrepancy between crystallite sizes estimated by the Debye-Scherrer method and the particle sizes seen in SEM micrographs has been previously reported for sputtered ZnO:Al layers [112] and for other nanocrystalline systems [34]. The origin of this difference is attributed to particles, consisting of a few crystallographic domains. Between those grains the grain barrier is being formed. One also has to keep in mind the possiblity, that the ordering within the first few nanometers of the material can be different from the bulk material.

The charge carrier density in the nominally undoped samples is surprisingly high. Considering the large energy gap of 3.3 eV [117] one can neglect the intrinsic equilibrium carrier density to contribute to the electrical conductivity. However, the experimentally observed charge carrier
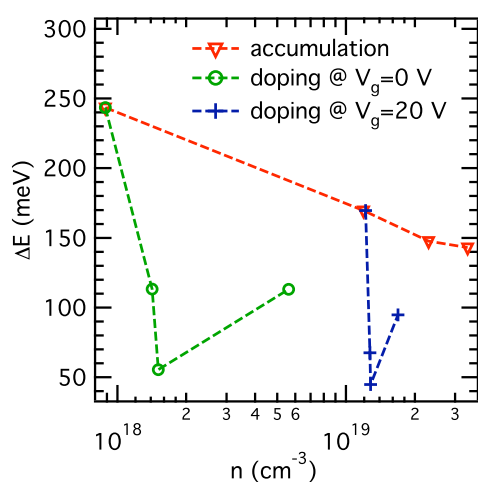
Abbildung 6.19: Potential barrier height ΔE *vs.* charge carrier density derived from temperature dependent mobility data at various V_g using Eq. (6.10). Comparison of the effect of doping (circles) and accumulation (triangles). The crosses represent the barrier height for various doping levels at V_g=20 V. Dashed lines: guides to the eye
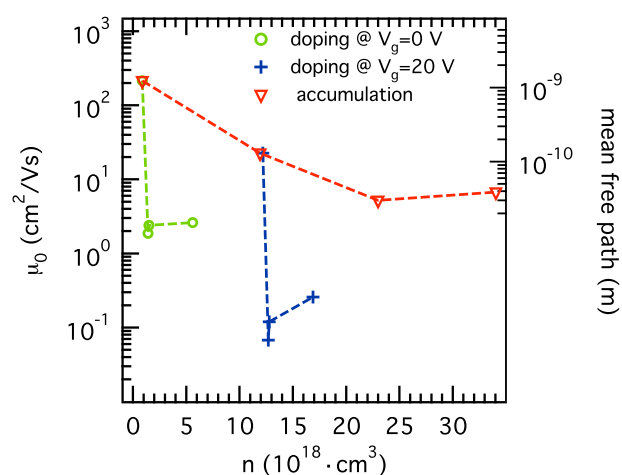
Abbildung 6.20: The extrapolation of the mobility to infinite temperatures μ_0 (left axis) gives an estimate for the mean free path (right axis) for electrons within the crystallites (assuming m/m^*=0.27). It is shown, that the mean free path is far beyond the crystallite size.

densities in the undoped case are in good agreement with literature for sputtered i-ZnO [78] and sol–gel processed i-ZnO [73]. The unintentional intrinsic doping of zinc oxide is probably due to oxygen and zinc lattice defects [74], as well as due to hydrogen interstitials, identified in crystalline systems [30, 53]. It should be noted that the purity of sol-gel-synthesized nc-ZnO also depends on the purity of starting materials. Such impurity traces (e.g. lithium [90]) may be incorporated in the nanocrystalline phases and eventually act as doping and trapping centers.

Depending on the Al-doping level, the charge carrier density increases from $8.9 \cdot 10^{17}$ cm^{-3} in the nominally undoped case to $5.6 \cdot 10^{18}$ cm^{-3} at 10 at%. The doping efficiency, i.e. the density of free carriers divided by the nominal density of dopants ranges around 1 %, in consistency with the literature on sol–gel derived ZnO:Al [100, 104].[†] Note that in some cases the opposite charge carrier density dependence on the doping level can be observed in Hall measurements [100]. There, a lowered n in sol-gel derived ZnO was reported at high doping levels. This trend could not be confirmed by our measurements.

For low doping levels, the increasing free charge carrier density leads to an enhanced conductivity, whereas the impurity-induced disorder lowers the mobility at high doping levels and thus counteracts the positive effect of a doping-induced high carrier concentration on the conductivity. Therefore, an optimal value for the conductivity can be found at 0.8 at% extrinsic doping level (Fig. 6.16). Note that the values of conductivity and mobility in nc-ZnO studied in this work are low in comparison to those reported in other publications [73, 104]. This effect is attributed to the low thickness of nc-ZnO layers, which are required by the field effect transistor geometry. An increase of the conductivity and the mobility proportional to the layer thickness has been reported previously [1, 107]. Also, an influence of contact barriers cannot be neglected for the determination of σ_{el}, even though this effect is expected not to be dominant. Assuming a very high contact resistance of 10 MΩm leads to a conductivity and free charge carrier increment of only a factor of two.

In the absence of electron accumulation (V_g=0 V) a slightly higher mobility at 0.8 at% as compared to the nominally undoped sample can be observed, which is attributed to a doping-induced lowering of the barrier height typically found in polycrystalline systems [10, 65, 92, 108], which was also reported for sol–gel synthesised nc-ZnO:Al [100, 104]. Further extrinsic doping of the nc-ZnO with Al leads to a decreasing electron mobility with increasing doping level, as shown in Figure 6.16. At V_g=20 V, decreasing mobilities for increasing doping levels are observed. Here, the charge carrier mobility is thus proportional to the crystallite size (see Table 6.1).

In order to investigate the charge transport properties of nc-ZnO in more detail, temperature dependent mobility measurements were performed. As seen in Fig. 6.18 the nominally undoped sample exhibits two different transport regimes as indicated by the changing slope of the temperature dependent electron mobility. This effect is well known for polycrystalline semiconductors; the high temperature regime is usually assigned to thermionic emission over energy barriers at the grain boundaries, whereas at low temperature thermally assisted tunnelling [92] or variable range hopping between donor states within the crystallites [86] is dominant. In case of tunneling the effective barrier height appears to be lower than in case of thermionic emission as the carriers are transported *through* the barrier. The activation energy derived in the high temperature regime initially decreases with increasing doping level with a minimum

---

[†]The nominal density of dopants was derived using the density of Zn atoms ($3.5 \cdot 10^{27}$ m^{-3}) in the Wurtzite structure.

barrier height at 2 at%. The sample with the highest dopant concentration shows an increase in the activation energy, as seen in Fig. 6.19. The decreasing activation energy for increasing doping level up to 2 at% is consistent with the above-mentioned doping-induced barrier height reduction. However, as the electron mobility in our systems mostly does not show the expected increase with lowered energy barrier, the charge transport is treated as not to be limited by thermionic emission over the grain boundaries but rather by the reduced mean free path (the average distance between two collisions) within the crystallite, as shown in Fig. 6.20. Note that high doping levels in crystalline systems also lead to a diminished temperature dependence of the mobility due to the reduction of the mean free path within the crystallites.

Concisely, two possible scenarious concerning the decreasing charge carrier mobility increasing doping level, (i) intercrystallite scattering due to a higher density of grain boundaries, and (ii) scattering within the crystallites at the defects in the band gap, could both explain our experiments by a formation of additional scattering centers. The first option, following the approach of Hossain et al. [57], has been considered: In the experiments presented here such dependence was not found. The domain size decreases gradually with increasing doping level, whereas the decrease of the electron mobility scales much stronger with the doping concentration (see Fig. 6.16). The barrier heights derived from the thermionic emission model would suggest enhanced electron mobility with increasing doping concentration. However, this could not be confirmed by the experiments presented here. Thus the explanation (i) is discarded for interpretation of the results raised in this section. The second scenario, scattering by doping-induced disorder and impurities, becomes thus the most probable explanation for the charge carrier mobility decreasing for doping concnetrations above 0.8 at%. This is in accordance with the strongly reduced mean free path of electrons in the doped films.

In contrast to the case of extrinsic doping, the mobility gradually increased with accumulation of charge carriers in the field effect transistor channel (see Fig. 6.17), whereas the trap density remains rather unchanged. The activation energy calculated from the temperature-dependent mobility via Eq. (6.8), shown in Fig. 6.19, decreases correspondingly. Thus, in the case of accumulation, where the density of scattering centers remains constant, the experimental results raised here suggest that the electron transport across grain boundaries is enhanced through a reduced effective barrier height.

Conclusions

Al-doped nanocrystalline zinc oxide has been synthesized via a sol–gel route, resulting in average crystallite sizes between 20 nm to 7 nm corresponding to doping concentrations from 0 at% to 10 at%. The thin films of nc-ZnO exhibit the Wurtzite structure as derived from XRD and SEM studies. The charge transport has been investigated by using field effect transistor structures prepared on SiO_2 with Au bottom contacts. The maximum conductivity was achieved at the doping concentration of 0.8 at% at room temperature. The accumulation of charge carriers in thin films of undoped zinc oxide nanoparticles results in higher charge carrier mobilities. In contrast, despite the extrinsic Al-doping leading to an increasing charge carrier density as well, the mobility decreases at higher doping levels. This is attributed to the formation of additional trap states of ionic, electronic and/or structural origin acting as scattering centers. High doping levels lead to smaller potential barrier heights at the crystallite interfaces. The potential barrier height derived from temperature dependent mobility measurements reaches its minimum

at a doping concentration of 2 at%. Further doping, however, leads to an increase of the charge transport activation energy, as the doping-induced structural defects become dominant. To conclude, the Al doping of sol–gel processed nanocrystalline zinc oxide is adjustable and can be controlled, but it does not automatically lead to improved electric transport properties as it simultaneously generates structural disorder and thus increases the scattering of charge carriers.
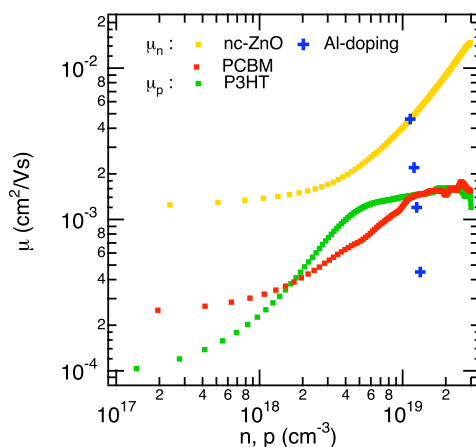
Abbildung 6.21: Mobility *vs.* estimated charge carrier density on SiO_2 dielectric at room temperature: undoped nc-ZnO (yellow dots) and Al doping at V_g=20 V (blue crosses), P3HT (green dots), PCBM red dots.

6.3 Comparison of Organic and Inorganic Nanocrystalline Semiconductors

Prior to the discussion of the charge transport in semiconductor blends, an interim result of the charge transport in PCBM and nc-ZnO:Al as well as their comparison with the hole transporting material P3HT is expedient. The results obtained for the hole transporting conjugated polymer were previously published in [50].

The Au bottom contact structures were chosen as the common reference geometry. It should be mentioned here, that the optimized electron mobility obtained for PCBM on the PVA dielectric is one order of magnitude higher than on SiO_2 with Gold bottom contact. For clarity, only the electron mobility in [60]PCBM is chosen here, as [70]PCBM and [60]PCBM show very similar results.

The mobility is shown as a function of the estimated charge carrier density in Fig. 6.21. On the SiO_2-dielectric, P3HT and PCBM show very similar dependence: The mobility is initially increasing by one order of magnitude and reaches a maximum of $1.5 \cdot 10^{-3}$ $cm^2V^{-1}s^{-1}$ in both materials. The mobility of nc-ZnO is somewhat higher, around $1 \cdot 10^{-2}$ $cm^2V^{-1}s^{-1}$ and and increases monotonically with the accumulation-induced carrier density. As indicated by the crosses, a low Al-doping of nc-ZnO presumably results in balanced electron and hole mobilities in blends with P3HT.

Concisely, the three materials exhibit increasing mobility with accumulated charge carrier density. In the case of organic semiconductors, this is explained by filling of tails states of the Gaussian density of states, whereas in the inorganic material, the effect is an interplay of barrier height lowering and—presumably—trap filling.

6.4 P3HT:PCBM Ambipolar Transistor

In solution-processed organic solar cells P3HT:PCBM blends are commonly employed as reference system for testing new absorber materials. Koster *et al*. have suggested that in such blended thin films a balanced mobility is essential to prevent charging of the absorber thin film by the slower type of charge carrier which would go alongside with electron–hole recombination [70] . To control the electron and hole mobilities for this demand one can alter the active layer nanomorphology (for a fixed blend composition) or one can vary the blending ratio of the polymer:fullerene composite. For the latter case one has to bear in mind that the polymer fraction should be sufficiently high to allow for strong photon absorption in thin films (note that the absorption coefficient of fullerenes is relatively poor in the visible range). Mostly based on empirical optimization of P3HT:PCBM solar cells, it is common acceptance that the optimal blending ratio lies in the range of 1:1 by weight. Whether this is in agreement with balanced carrier mobilities remains, however, under discussion [14, 32]. This issue is, however, of a more general meaning as it suggests the control handles to manipulate the charge transport properties of full-organic composite semiconductors, e.g. in respect of the initial objective to achieve balanced carrier mobilities in solution-processed FET structures.

Specific experimental details

P3HT and [60]PCBM were separately dissolved in chlorobenzene to give solutions of 1 wt.% concentration. Compositions with a relative PCBM content of 0.33, 0.5, 0.67, 0.75, 0.8 and 0.9 were prepared by appropriate mixing of the P3HT and PCBM solutions. For the field effect transistors SiO_2 was chosen as gate dielectric and Au-electrodes were used as bottom source and drain contacts. In order to average over a large sample area the contact structures shown in Fig. 5.2(c) were chosen. The respective composite films were applied via spin coating on top of the SiO_2/Au-structures. Facultatively, an annealing step at 120° C was carried out for the completed devices under inert gas atmosphere. In case of the 1:1-blend ratio an alternative FET-structure with top contacts (Fig. 5.2(d) and 5.2(e)) made from aluminum was studied as well.

Results

The ratio-dependent electron and hole mobilities in annealed blends were evaluated at a fixed charge carrier density, i.e., $V_g - V_{th}$=10 V, see Fig. 6.22.[‡] As the mobility increases with the carrier concentration, this does not necessarily provide the maximum achievable mobility. The hole mobility of the blend was observed to decrease with increasing PCBM content from $4 \cdot 10^{-5}$ cm^{2}V^{-1}s^{-1} (pure P3HT) to $1 \cdot 10^{-5}$ cm^{2}V^{-1}s^{-1} (1:1 blend, i.e. 50% PCBM), followed by a pronounced increase of the hole mobility $2.2 \cdot 10^{-3}$ cm^{2}V^{-1}s^{-1} in the case of 80% PCBM content. At higher PCBM content, unipolar hole transport was not observable. The increase of the hole mobility at high PCBM loads in the blend can have its origin in (i) the enhanced hole mobility within P3HT due to an advantageous morphological change or (ii) as stated in [14] an enhanced hole mobility in PCBM. Unipolar electron transport could only be observed at PCBM

[‡]For SiO_2 (100 nm) gate voltages below |50 V| are uncritical while the threshold voltage amounts up to 30 V (if applicable), depending on the blend ratio. Hence, evaluating the mobility at $V_g - V_{th}$=10 V is reasonable.
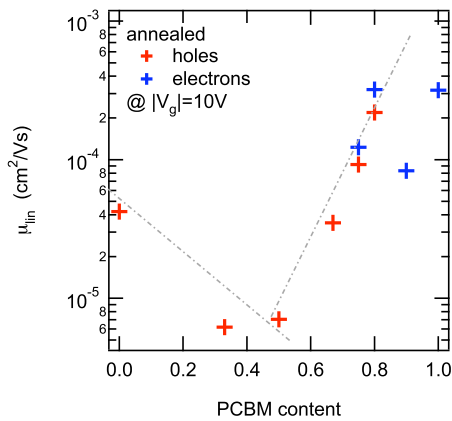
Abbildung 6.22: Mobility *vs.* PCBM content in P3HT:PCBM FETs (SiO$_2$/Au-structures. films annealed at 120° C)
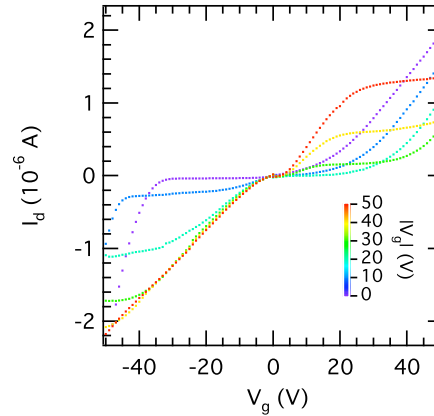
Abbildung 6.23: Output characteristics of an annealed P3HT:PCBM (1:3) FET. The gate voltage is indicated by the color scale. (SiO$_2$/Au-structures. films annealed at 120° C, L=80 μm, W=56.9 mm, d_{ins}=100 nm)

ratios exceeding 70% with a maximum mobility of $3 \cdot 10^{-3}$ cm^{2}V^{-1}s^{-1}. The balance of electron and hole mobilities was achieved for a 1:3 mixture of P3HT and PCBM.

The output characteristics of an annealed P3HT:PCBM (1:3) FET is shown in Fig. 6.23. The enhancement of electron (hole) concentrations occurs at positive (negative) V_g and V_d. At high V_d and low V_g an exponential increase of the current was observed: Both, electrons and holes can be injected into the off-pinched channel and create a recombination zone in the channel which position depends on the fraction V_d/V_g as described in Section 4.1.2. Applying high negative (positive) V_g and low V_d removes the electrons (holes) from the channel and the device behaves as an unipolar hole (electron) accumulating transistor. At high negative V_g (hole accumulation) the channel behaves as a resistor and no pinch-off point could be observed. This is attributed to a high contact resistance for hole injection outweighing the channel resistance, as presumably only a low fraction of P3HT is present at the source and drain contact. At low $|V_d|$ an injection barrier for electrons and for holes could be observed from the S-shaped current.

The electron and hole mobilities of the neat materials exhibit equal values at high charge carrier densities on SiO$_2$/Au, as shown in Sec. 6.3. From the mobilities found in the neat materials at $|V_g - V_{th}| = 10$ V, one would conclude balanced electron and hole transport at 50% PCBM content or even lower, unless the blend/SiO$_2$ interface morpholgy was changed. One possible explanation of this disagreement of results obtained for neat and blended materials is that PCBM withdraws from the organic/dielectric-interface. In such situation, the desired electron accumulation in the channel is reduced or even fails. Several studies have confirmed the difference between the surface and the bulk composition of an organic blend [95], specifically in P3HT:PCBM-composites deposited on SiO$_2$ and indium tin oxide substrates [40, 97]. Accordingly, the diminished electron mobility observed for P3HT:PCBM blend ratios smaller than 1:3 may be ascribed the deficient fraction of PCBM at the SiO$_2$ interface. In FETs based on blends of n- and p-type organic semiconductors, balanced electron and hole mobilities could only be
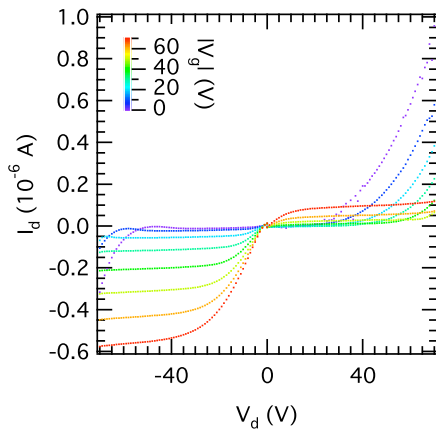
Abbildung 6.24: Output characteristics of a pristine P3HT:PCBM (1:1) FET in a top-contact configuration. The semiconductor film was directly applied on the SiO_2 dielectric. The electron conduction is improved compared to FETs with the same semiconductor film but with bottom contacts made from gold. (SiO_2/Al-structures, pristine film, L=80 μm, W=82 mm, d_{ins}=200 nm)
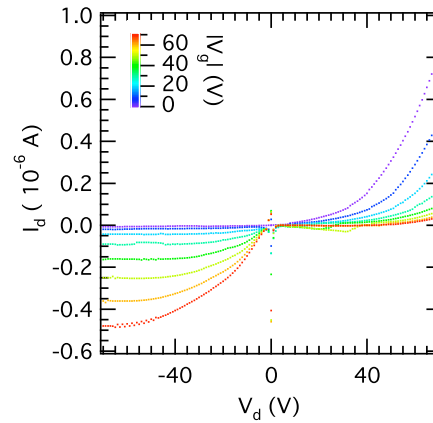
Abbildung 6.25: Output characteristics of an annealed P3HT:PCBM (1:1) FET in a top-contact configuration. Upon annealing, the unipolar electron regime (positive V_g and V_d) is diminished compared to the pristine case shown in Fig. 6.24.

observed in the cases where effectual PCBM is present at the interface, here at P3HT:PCBM ratios of 1:3 and 1:4. It has to be noted, that the reproducibility of the as-cast (non-annealed) devices was not sufficient, which indicates, that the morphology of the pristine layer is not stable. Even though, unipolar electron transport in the pristine samples was only observed at PCBM contents exceeding 75%. As electron transport was confirmed in as-cast and annealed FETs only for PCBM concentrations exceeding 50% one may anticipate that the composition of the blend at the dielectric interface differs considerably from that in bulk. This result is astonishing, as P3HT:PCBM bulk heterojunction solar cells show their best performance when blending ratios close to 1:1 are employed. It should be pointed out here that the effect of PCBM depletion at the interface could be present in solar cells and FET structures as the surface energies of indum tin oxide (transparent window electrode in organic solar cells) and SiO_2 are nearly the same [40]. For solar cells these results suggest that not only the bulk morphology but also the in-depth variation must be considered for the explanation of the optimum performance at 1:1 blend ratios.

In order to check whether the bottom interface was really depleted from PCBM due to the minimization of the free energy of the P3HT:PCBM–SiO_2 system [40], top contact FETs were used in order to improve the injection and to confirm the PCBM accumulation at the surface by an increased conductivity. The output characteristic of non-annealed P3HT:PCBM (1:1) on SiO_2 with aluminum top contacts is shown in Fig. 6.24. In this case, unipolar electron transport (positive V_g and V_d) is observable even at a PCBM concentration of 50%. The resulting electron mobility is $1 \cdot 10^{-4}$ cm^{2}V^{-1}s^{-1}, the hole mobility is $3 \cdot 10^{-4}$ cm^{2}V^{-1}s^{-1}. This finding is attribu-

ted to an improved electron injection into the PCBM phase, compared to the injection from Au bottom contacts. Nevertheless, the electron and hole mobilities differ by a factor of three, which again indicates that the SiO_2 interface composition is partly depleted of PCBM. It has to be noted, that the reproducibility of transport within pristine films is not satisfactory reproducible, although Al top-contacts were used.

The output characteristics of the annealed Al-top-contact FET with SiO_2 dielectric is shown in Fig. 6.25. The unipolar electron regime (positive V_g and V_d) is diminished compared to Fig. 6.24, and the electron mobility in the channel is no longer accessible due to thermally-induced electron depletion of PCBM. The absolute drain current at negative V_g and V_d is diminished compared to the non-annealed case, which is in consistency with higher hole mobilities for increasing PCBM content [14].

Discussion und Conclusion

The hole and the electron transport in P3HT:PCBM blends were studied depending on the relative concentrations of the hole and electron conductors on SiO_2 using Au bottom contacts. The results are in general agreement with literature data for P3HT:PCBM FETs reported in [63, 80, 109, 125]. Nevertheless, the 1:1-ratio did not result in balanced electron and hole mobilities, as it was naively expected based on the results obtained for the neat materials and from the optimum ratio for the solar cell performance. As the FET measurement is an interface-sensitive technique, the diminished electron mobility was attributed to the PCBM-depleted SiO_2-(and also ITO) interface [40, 97].

By using Al top contacts it was possible to observe ambipolar charge transport even in FETs with blending ratio of 1:1, which was attributed to the improved injection into the PCBM phase from the top interface. Upon annealing this specific device, the accumulation-induced unipolar electron transport is suppressed, which again could be attributed to PCBM-segregation from the SiO_2 interface.

A clear relationship between the charge transport in solar cells and FETs could not be established here. On the one hand, the charge transport in solar cells occurs perpendicular to the surface of the ITO electrode and hence to the charge transport direction in FETs. Nevertheless, as the anode in solar cells (ITO) has a similar surface energy as SiO_2, similar surface compositions of P3HT:PCBM blends are expected in solar cells and FETs. However, the FET measurements provide a strong evidence, that PCBM segregates from the SiO_2 interface. In contrast to the assumption of a bulk-heterojunction (BHJ) [131] these findings rather imply a fractal heterojunction, comparable to extremely thin absorber (ETA) cells with interpenetrating pn-junction [36]. This might be an alternative explanation for the working principle of the so-called "BHJcells.

By adjusting the P3HT:PCBM ratio, it was possible to achieve ambipolar transport in P3HT:PCBM blends on SiO_2 using Au bottom contacts, although a high fraction of PCBM had to be employed. By skipping the annealing step and using Al top contacts, even an 1:1 ratio of P3HT and PCBM resulted in almost balanced mobilities.

Concisely, it is technologically demanding to achieve reproducible and stable ambipolar FETs with two molecular materials. As the dielectric-semiconductor interface is likely to become depleted of one phase, balanced field-effect mobilities could only be achieved by using high fractions of this component.

In order to achieve balanced mobilities in the P3HT:PCBM system, it is essential to have well defined conditions regarding the interfaces, interface morphology, contact metals and the FET geometry. The realization of solution processable ambipolar FETs requires an alternative n-type semiconductor, preferentially with adjustable electronic properties in order to account for balanced ambipolar charge transport.

6.5 nc-ZnO:Al/P3HT Ambipolar Transistor [§]

The fabrication of printable electronics requires the development of solution-processed complementary circuits, where both n-type and p-type semiconductors are incorporated using a simple device architecture. In this context, ambipolar field-effect transistors employing a single organic compound as active layer have been reported [106]. A drawback of the latter device is that such single-material device is that electron and hole mobilities are generally unbalanced and, technologically more demanding, two different metals have to be used for electron and hole injection. It has been shown in the last section that by blending organic p- and n-conductors the desired ambipolarity can be achieved in transistors. However, the performance of these devices was supposed to be sensitive to the interaction of the specific semiconductors with the dielectric and to the FET geometry. A promising approach presented here is the use of an organic/inorganic hybrid system. Inorganic materials offer the customizability of the charge transport properties via doping and establishes an advanced concept for achieving optimum ambipolar performance in combination with the organic semiconductor. The organic counterpart offers all advantages of polymer technologies, e.g. printability and infiltration ability. Furthermore, doping of nanocrystalline semiconductors is likely to result in structural modifications of the respective inorganic thin films, such as surface roughness and porosity, which allows to define a three dimensional matrix for the subsequent intrusion of the organic polymer. Though nanocrystalline zinc oxide has been employed as electron acceptor in hybrid solar cells [15] and bilayers of the thermally evaporated pentacene on ZnO have been investigated in FETs [94], the general characteristics of ZnO–polymer hybrids in ambipolar field-effect transistors have not been explored yet.

Here, sol–gel processed nc-ZnO with varied Al-doping level was used as the n-type semiconductor and regioregular poly(3-hexylthiophene), as the p-type component, to fabricate field effect transistors (FETs) with gold source and drain contacts on a SiO_2 dielectric. In Section 6.2 it was demonstrated that doping has a strong effect on the structural and electrical properties of sol–gel processed sintered ZnO:Al. Along with increasing doping concentration the electron mobility was found to decrease due to the formation of structural, morphological, and ionic defects.

In order to achieve the presence of both semiconductors close to the conducting channel an interpenetrating structure of the two semiconductors has to be realized. One approach is to mix the precursor solutions of the neat materials and subsequently to apply blended thin films via spin coating; however, this simple technique has the drawback that thermal removal of monoethanolamine (MEA) from the nc-ZnO:Al moiety must be omitted. Attempts to fabricate hybrid thin films via this approach were not successful due to unsatisfactory reproducibility of the electronic and structural thin film properties. An alternative route is to apply the nc-ZnO:Al precursor solution on top of the dielectric followed by thermal removal of the MEA but leaving out the sintering step required for condensing the nc-ZnO. This technique is expected to result in ZnO thin films with some porosity which allows infiltration of the organic component. Being a prerequisite for the realization of hybrid ZnO:P3HT field-effect transistors the success of the polymer intrusion was verified for differently doped ZnO-films via X-ray reflectivity – a proven technique to study multilayer structures with buried interfaces.

Specific experimental details

The synthesis of Al-doped ZnO was performed according to the route introduced by Xue *et al.* [128]. P3HT was dissolved in chlorobenzene at 0.1 wt%. The field-effect transistor structures were prepared on Si:Sb/SiO$_2$ with Ti/Au bottom contact structures as shown in Fig 5.2(c). Channel lengths of 160 μm were chosen, so that the channel resistance dominates the contact resistance and, hence, minimizes the influence of the contact on the measured transport parameters. The ZnO solution with the intended Al doping level was spin coated and thereafter, the substrate was heated to 300° C in an oven in ambient atmosphere in order to remove MEA. The sintering step at 500° C was left out. Then the samples were transferred to a glovebox where the P3HT solution was spin coated on top of the nc-ZnO:Al film. Finally, the samples were slowly dried for 15 hrs. The reproducibility of FETs was confirmed for several samples in regard of their electrical characteristics. The room-temperature measurements were performed in nitrogen atmosphere before and after the infiltration of P3HT. The absorption spectra of the material system on sapphire were recorded using a PerkinElmer Lambda 950. The X-ray reflectivity measurements were carried out using an X-ray diffractometer from General Electrics (3003 T-T). The X-ray measurement provides a non-destructive way of probing the layer thickness, interface roughness and the electron density of single and multi layers. For XRR, the sample is exposed to the radiation of a Cu K$_\alpha$ tube with the characteristic wavelength of λ=1.5406 Å. From θ =0° up to a critical angle θ_c, total reflection dominates, as radiation can penetrate the layer only evanescently. As discussied in Section 4.2 θ_c is a measure for the electron density ρ_e and hence, a measure for the effective material density. The intermixing of the two phases can thus be determined from the attenuation of the corresponding Kiessig fringes.

Results

Field-effect-transistor measurements

In Section 6.2 the charge transport in nc-ZnO:Al field-effect transistors has been investigated. These structures experienced a sintering step for achieving sufficient particle condensation. For the fabrication of hybrid FETs, however, this high-temperature step is left out in order to achieve the desired porosity for the subsequent intrusion of the polymer. Prior to the fabrication and optimization of hybrid structures the reliable operation of unsintered nc-ZnO:Al needs to be verified.

The output characteristics of a field-effect transistor with unsintered ZnO:Al (2 at.%) is shown in Fig. 6.26. The gate and the drain voltage have each been varied between 0 V and 70 V. The output characteristics exhibit Ohmic behavior in the linear regime, indicating efficient injection from the gold contact into the conduction band of ZnO:Al and saturation of the drain current at high drain voltages can be observed. The pinch-off voltage increases quadratically with the applied gate voltage.

The threshold voltage V_{th} (see Fig. 6.27(a)) has been extracted from the transfer characteristics in the saturation regime. Ohmic injection provided, V_{th} is a measure for trapped charges in the material and at the ZnO:Al/dielectric interface and also for free charge carriers intrinsically present in the channel. It has to be noted that additional charge carriers introduced via Al-doping will compensate these electron traps up to the Fermi level. The threshold voltage of nc-ZnO:Al transistors varies between 5.5 V for the doping concentration of 0.8 at.% and 25 V for 5 at.%
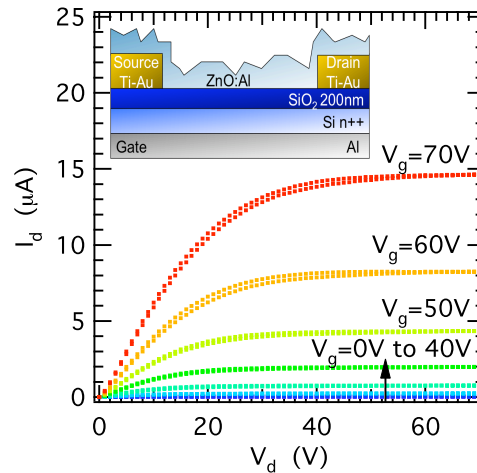
Abbildung 6.26: nc-ZnO:Al (2 at.%) output characteristics. Transistor details: Ti/Au bottom contacts L=160 μm, W=62.4 mm, SiO$_2$ thickness d=200 nm. The inset shows a schematic drawing of the device.

(see Fig. 6.27(a).

In order to consider the effect of doping in unsintered ZnO:Al the charge transport properties were analyzed in terms of the carrier density and the threshold voltage. The conductivity σ_{el} was deduced from the linear regime of the output characteristics without carrier accumulation, i.e. V_g=0 V. Then $I_d = j * W * d_{Au} = \sigma_{el} V_d / LW d_{Au}$, where W and L are the width and length of the channel and d_{Au} is the effective height of the channel approximated by the thickness of the S/D-contacts (see Fig. 6.27(b). For the electrical conductivity a maximum of $3 \cdot 10^{-3}$ Ω^{-1}m^{-1} was observed for 0.8 at.% doping level which nicely corresponds to the characteristics of respective FET structures with sintered ZnO:Al. (see Section 6.2). The conductivity exhibits a global minimum at 5 at.% doping level and slightly increases when further increasing the doping level. The latter effect was confirmed for various samples but remains unexplained, yet. With evaluating $\sigma_{el} = \mu n e$ at low gate and drain voltage it is further possible to obtain a rough estimate of the charge carrier density. Fig. 6.27(b) shows the variation of n with the doping concentration. The lowest value of $2 \cdot 10^{16}$ cm^{-3} was obtained for 2 at.% and is followed by a gradual increase of n at higher doping concentrations. Doping generally leads to an increase of the carrier concentration but also increases the impurification of the host material (structural and compositional) which is expected to result in enhanced scattering of charge carriers and thus a reduced mobility. In a FET structure the threshold voltage is *inter alia* influenced by the equilibrium concentrations of free and trapped charge carriers. In case of unsintered ZnO:Al V_{th} exhibits a qualitative correlation with the carrier density as deduced for the different doping levels (Fig. 6.27(a)).

Hybrid ZnO:Al/P3HT-Transistors After the characterization of the field-effect transistors with bare nc-ZnO:Al at several doping levels, the electronic behaviour of transistors with ZnO:Al/-P3HT layers were analyzed. The output characteristics of ambipolar ZnO(2 at.%)/P3HT transistor on a semilogarithmic scale in Fig 6.25 (a) is shown in Fig. 6.28(a). At high V_d and low V_g both, electrons and holes can be injected into the channel and form a recombination zone within the channel, as discussed in Section 4.1.2. Applying high negative (positive) V_g and low
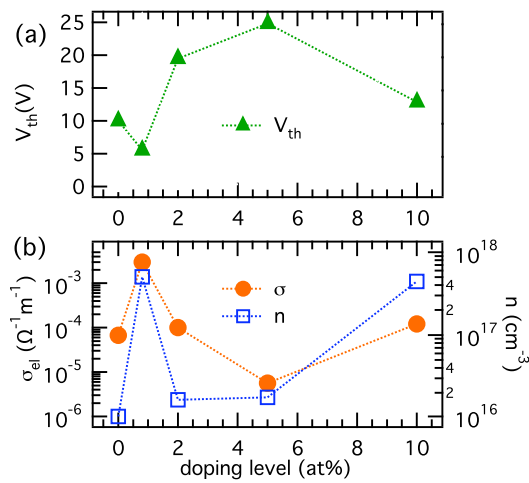
Abbildung 6.27: Neat ZnO:Al: (a) Threshold voltage for electron transport in the saturation regime. (b) Estimated conductivity and free charge carrier density. As indicated, there is a qualitative correlation between V_{th} and n.
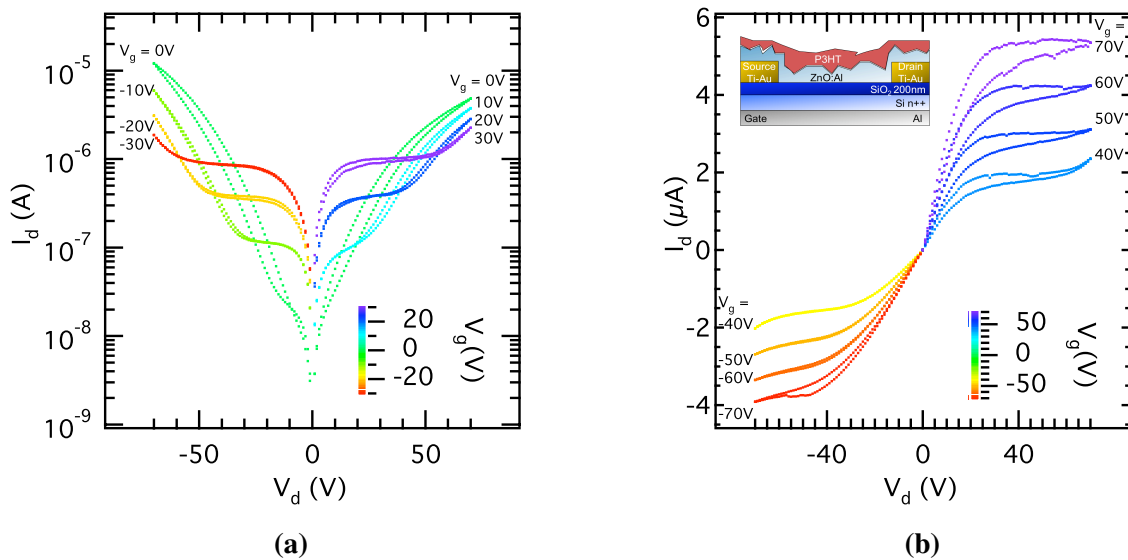
Abbildung 6.28: ZnO:Al (2 at.%)/P3HT-transistor: Output characteristics; V_g is indicated by the by the legend. Shown is the same device as in Fig 6.26 but with additional P3HT hole transport layer: (a) from V_g=-30V to 30V in semilogarithmic scale, (b) from V_g=-70 V to -40 V and from 40 V to 70 V. The inset shows a schematic drawing of the device.

V_d depletes the electrons (holes) from the channel and the device behaves as an unipolar hole (electron) accumulating transistor (see Fig. 6.28(b)). Furthermore, the unipolar regime in both, hole and electron accumulation regions, shows Ohmic behaviour at low V_d. It has to be noted that this Ohmic behavior was achieved using gold for electron *and* hole injection and no additional modification of the dielectric was applied, making the device architecture straightforward and simple to prepare. Comparing the output characteristics of the pure ZnO:Al (2 at.%) FET (see Fig. 6.26) with the device, where P3HT had been coated, only a slight decrease in the maximum drain current was observed. In the electron accumulation regime (Vg>0), an enhanced hysteresis can be observed: The occupation of trap states leads to the formation of space charges which partially screen the applied electric field. Note that in neat ZnO:Al FETs with gold electrodes no hole accumulation could be observed.

Fig. 6.29(a-e) shows the corresponding transfer characteristics in saturation at $|V_d|$=40 V of the ambipolar hybrid transistors for different doping levels of the inorganic component.

The undoped system exhibits unipolar behaviour for electrons. Similar values for the drain current at high positive V_g can be observed at negative V_d and low gate voltages although hole accumulation occurs only below $V_g = -50$ V. The difference between the drain current at V_g=0 V at positive and negative V_d is directly correlated to the difference of e and h-mobilities: Assuming negligibility of the difference between $V_{th,n}$ and $V_{th,p}$, the quotient of the drain currents at positive and negative V_d in the ambipolar range at V_g=0 V, in Eq. (4.34) reduces to

$$\frac{I_d(+V_d)}{I_d(-V_d)} \approx \frac{\mu_p}{\mu_n} \qquad (6.9)$$

Almost symmetric behaviour of the respective tranfer characteristics can be observed for the P3HT:ZnO:Al (2 at.%) system. The transfer characteristics of P3HT/ZnO (5 at.%) has the drawback of a small on/off ratio. For 10 at.% doping the onset of hole accumulation occurs at negative voltages higher than $|V_g|$=70 V.

Fig. 6.30(a) shows the threshold voltage V_{th} *vs.* doping level for electrons ($V_{th,n}$, closed symbols) and holes ($V_{th,p}$, open symbols) for the saturation regime. While $V_{th,n}$ increases from around 0 V in the undoped case to 17.5 V and stays nearly constant for higher doping levels, large fluctuations of $V_{th,p}$ between +23.6 V and −50.9 V were observed.

The electron mobility, μ_e, at $|V_g - V_{th}|$=40 V and $|V_d|$=40 V is shown in Fig. 6.30(b). μ_e decreases over one order of magnitude from $3.2 \cdot 10^{-3}$ cm^{2}V^{-1}s^{-1} for the undoped system to $6.5 \cdot 10^{-5}$ cm^{2}V^{-1}s^{-1} at an Al-concentration of 10 at.%. This behaviour is attributed to additional defects of structural, ionic and/or electronic origin introduced via doping [51]. Obviously, the infiltration of P3HT does not significantly affect the electron mobility, i.e., the impact of polymer infiltrating is negligible and the transport parameters of undoped and doped zinc oxide remain almost the same. μ_e in the hybrid system decreases decreases by one order of magnitude upon increasing the doping concentration from 0 at.% to 10 at.% from $2 \cdot 10^{-3}$ cm^{2}V^{-1}s^{-1} to $2 \cdot 10^{-4}$ cm^{2}V^{-1}s^{-1}.

The hole mobility (see Fig. 6.30(b)) in the hybrid system, without Al-doping and at a doping level of 0.8 at.%, is about two orders of magnitude lower than the hole mobility observed in pure P3HT transistors (see sec. 6.3). 2 at.% Al doping of ZnO induces an increase of the hole mobility of more than one order of magnitude to $5 \cdot 10^{-4}$ cm^{2}V^{-1}s^{-1}.

In the case of hole accumulation, ZnO:Al can be assumed to be an additional dielectric on
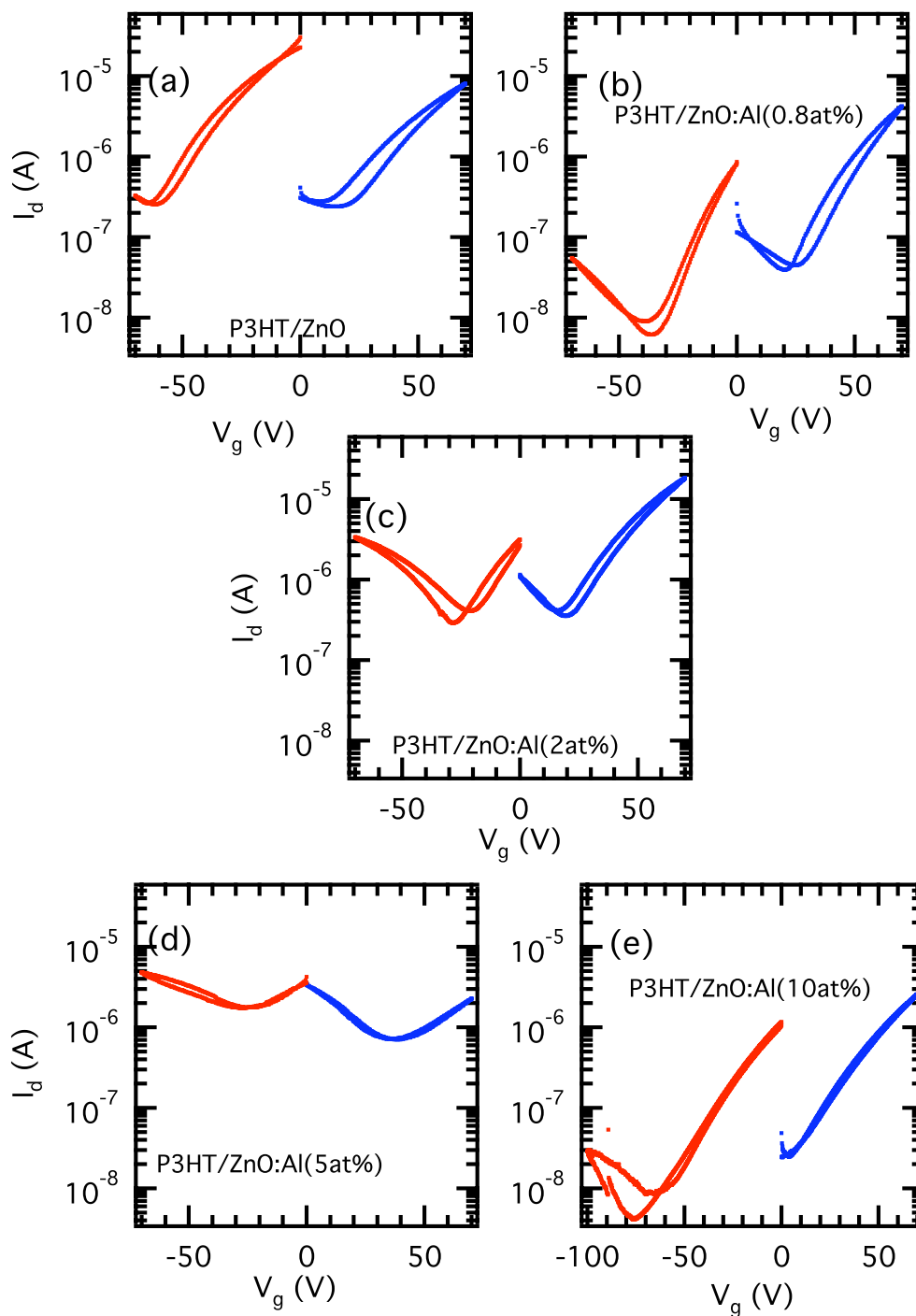
Abbildung 6.29: ZnO:Al/P3HT-Transistor: (a)-(e)Transfer characteristics in saturation regime at $|V_d|$=40 V for hole (red line) and electron (blue line) accumulation. Forward and backward direction show little charging effects. V_g ranges from -70 V to +70 V, except for the 10 at% system (e).
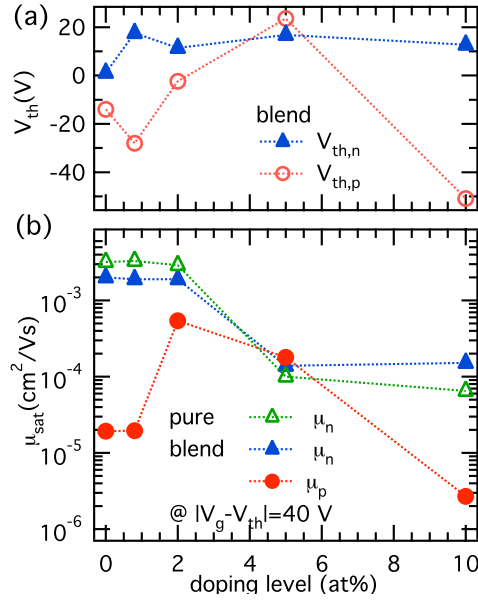
Abbildung 6.30: ZnO:Al/P3HT-transistor: (a) Threshold voltage $V_{th,n}$ for electrons and $V_{th,p}$ for holes at various doping levels of th inorganic semiconductor. (b)Saturation mobility derived from the transfer characteristics; green triangles: electron mobility in pure ZnO:Al as reference, blue full triangles and red circles: electron and hole mobility in ZnO:Al/P3HT, respectively.

top of SiO_2. The accumulated charge per unit area Q_i depends on the thickness of the dielectric

$$Q_i = \varepsilon_{ins}\varepsilon_0/d \cdot (V_g - V_{th}), \tag{6.10}$$

where ε and ε_0 are the relative and absolute permittivities and d is the thickness of the dielectric. Note that the calculated hole mobilities refer to a 200 nm SiO_2 dielectric solely. The assumption of a constant capacitance was verified experimentally. Capacitance measurements on Si n^{++}/SiO_2(200 nm)/ZnO:Al/Au, i.e. treating SiO_2 and ZnO:Al as two series capacitors did not reveal significant changes with respect to the bare SiO_2 dielectric. This result is plausible since the smallest capacitance, here that of SiO_2, determines the total capacitance.

Evidently, the undoped and the 0.8 at.% Al-doped ZnO/P3HT hybrid transistors do not exhibit balanced electron and hole mobilities: μ_e and μ_p differ by two orders of magnitude. In the case of 2 at.% Al doping a hole mobility of $5 \cdot 10^{-4}$ $cm^2V^{-1}s^{-1}$ was observed and the value differs by only a factor of five from μ_e at the same doping level. For doping levels of 5 at.% balanced mobilities were indeed obtained and aside from that, a decrease of the electron mobility. The highest Al-doping level of 10 at.% leads to a strong decrease in μ_p and a large difference between μ_p and μ_e.

Interface morphology

The dependence of the P3HT hole mobility on the Al-doping level of ZnO cannot be understood merely from the data obtained from the electrical measurements. The relation between μ_p and doping level could have several reasons:

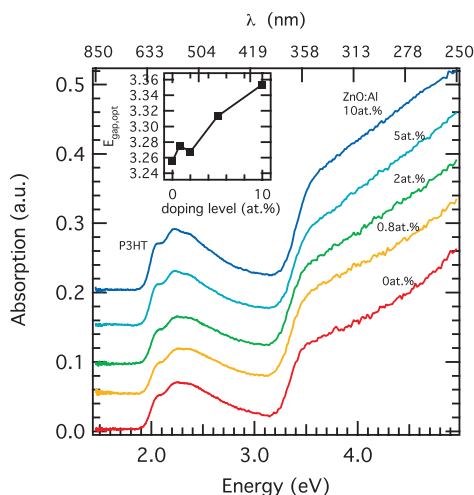**(i)** various degrees of crystallinity in the polymer phase,

Abbildung 6.31: nc-ZnO:Al/P3HT absorption spectra. The inset shows the optical band gap of nc-ZnO at different doping levels. The substrate was sapphire.

(ii) the interface topography of nc-ZnO and the related ability to infiltrate P3HT,

(iii) the dielectric properties at the interface,

(iv) defects or charged traps at the organic/inorganic interfaces generated by doping.

Obviously, in any of the four cases the interface topography is of essential relevance for the density of free holes in the FET channel.

Absorption   Absorption spectra were measured in order to obtain information on the polymer aggregation in the hybrid films (interchain absorption) and to clarify the effect of doping on the absorption edge of ZnO:Al. The absorption spectra of differently doped hybrid films are shown in Fig. 6.31. Photon absorption by ZnO is observed in the UV region at wavelengths lower than 380 nm, in good agreement with literature [73]. Using $(\alpha h\nu)^2 = A(h\nu - E_g)$ [29], where A is a function of the refractive index of the material, the reduced mass and the speed of light in vacuum, h is the Planck's constant, ν is the frequency of the monochromatic probe beam and E_g is the energy band gap. From a plot of $(\alpha h\nu)^2$ versus the photon energy an optical band gap was obtained by applying a linear fit and an extrapolation to $(\alpha h\nu)^2=0$ eVm^{-1}. The undoped nc-ZnO exhibits an optical band gap of 3.26 eV and a shift by 100 meV to higher energies for the highest Al-doping level was observed.

The polymer P3HT absorbs in the visible range between $\sim$1.9 eV and $\sim$3 eV. It has been reported that enhanced ordering of this polymer gives rise to an increased absorption at $\sim$2.09 eV [21, 25]. The absorption spectra shown in Fig. 6.31 indicate a high degree of ordering of P3HT for all doping levels. As the spectral shape of polymer absorption, particularly around 2.09 eV, does not change, these results do not provide further information on the actual interface formation between the two components.

X-ray reflectivity   The intermixing of both semiconductor phases can be quantified via X-ray reflectivity measurements: XRR is sensitive to the electron density (free and bound) of the

Tabelle 6.2: Electron density ρ, thickness d and rms roughness R_{rms} of the ZnO:Al layer resulting from fits of the XRR spectra shown in Fig. 6.32.

	0 at.%	0.8 at.%	2 at.%	5 at.%	10 at.%
$\rho_{ZnO:Al}$ $(e^-\text{Å}^{-3})$	1.1	1.1	1.3	1.1	1.2
ρ_{P3HT} $(e^-\text{Å}^{-3})$	0.1	0.2	0.1	0.2	0.3
$\rho_{interlayer}$ $(e^-\text{Å}^{-3})$	0.1	0.4	0.2	0.9	1.0
$d_{ZnO:Al}$ (nm)	15	16	12	17	23
d_{P3HT} (nm)	20	19	23	26	25
$d_{interlayer}$ (nm)	4	5	19	1	2
$R_{rms,ZnO:Al}$ (nm)	2	1	1	0	1

materials which differs by one order of magnitude in P3HT and undoped/Al doped ZnO. XRR has the unique advantage over, e.g. AFM, that buried interfaces can be probed in the complete sample.

The XRR measurements of ZnO:Al/P3HT for different Al-doping levels are shown in Fig. 6.32. The XRR measurements were carried out on SiO_2 and additionally on sapphire substrates. The data were in qualitative agreement using different substrates. The reproducibility on SiO_2 was confirmed by different samples. All shown data are from one series on SiO_2.

Four of the five hybrid structures clearly exhibit Kiessig fringes. The most pronounced fringes can be detected for the 5 at.% and 10 at.% Al-doped compounds: One can distinguish between two different oscillations hinting at the two layers, P3HT and nc-ZnO:Al, respectively, and a surprisingly small roughness at their interface. The spectra of the undoped and 0.8 at.% Al-doped samples comprise fringes, as well. The spectrum of the 2 at.% Al-doped ZnO/P3HT does not show pronounced interference features indicating a high level of interpenetration of the organic and the inorganic components accompanied by a high effective interface roughness.

To obtain *quantitative* information about the thickness of P3HT and ZnO and of the interface roughness it is essential to perform simulations and fitting of the experimental data. This allows a direct determination of the interface roughness related to the infiltration of P3HT. The theoretical reflectivity was calculated by an optical matrix method, with a refinement procedure minimizing the difference between the calculated and the measured XRR curve: the program MOTOFIT [87] based on the Parratt-formalism[98]. The optimization of the parameters was done by minimizing the chi square in logarithmic form. Here, χ^2 values around 5 % could be obtained The real part of the scattering length density (SLD) which is directly related to the mass density and the atomic number ranges between $30.0 \cdot 10^{-5}\text{Å}^{-2}$ and $35.5 \cdot 10^{-5}\text{Å}^{-2}$ for ZnO and between $3.0 \cdot 10^{-5}\text{Å}^{-2}$ and $9.3 \cdot 10^{-5}\text{Å}^{-2}$ for P3HT. The layer thickness of ZnO:Al ranges between 12 and 23 nm, for P3HT between 19 nm and 26 nm. The extracted data including the electron density, derived from $\rho=SLD/r_e$, with r_e the classical electron radius, are shown in Table 6.2.

The fits based on the Parratt formalism are shown in Fig 6.32(a). In order to obtain appropriate fits, it was necessary to assume intermixing of the P3HT and the ZnO:Al phases. A thin intermixing layer between 1.1 and 2.2 nm is estimated for 0, 0.8, 5 and 10 at.% Al doping and
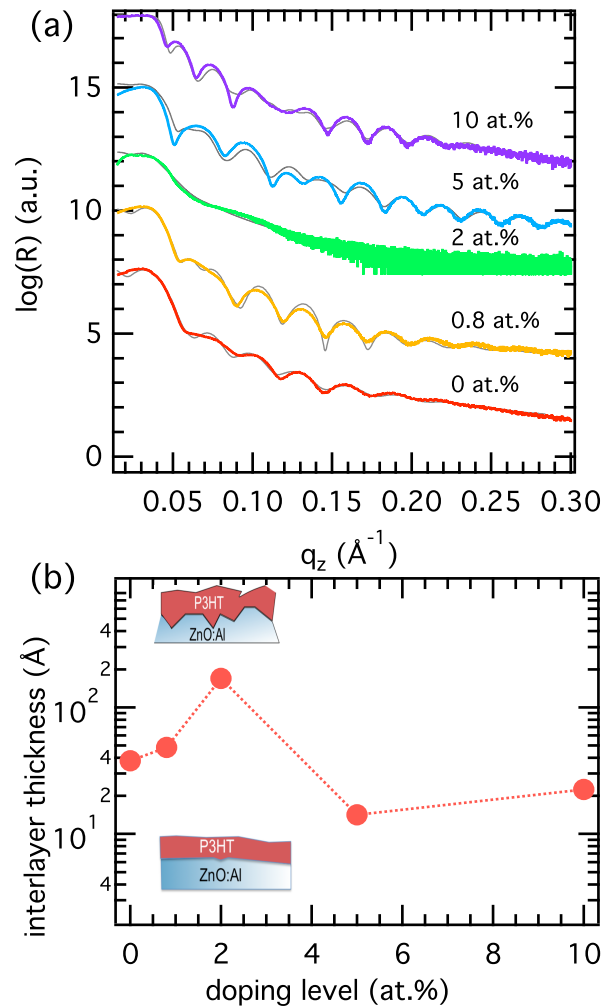
Abbildung 6.32: (a) X-ray reflectivity curve of nc-ZnO:Al/P3HT at various Al-doping levels as indicated by the legend. Grey lines are corresponding to fits based on the Parratt formalism. The profiles have been offset for clarity. (b) ZnO:Al/P3HT effective interlayer thickness as derived from XRR spectra. A schematical drawing of intermixing is provided by the insets: upper drawing: high degree of intermixing, lower drawing: low degree of intermixing.

a very high value of 18.6 nm for 2 at.% as shown in Fig 6.32(b).

Discussion

The first part of the discussion addresses the Al-doping of nanocrystalline ZnO which was found to result in substantial implications for the electron transport. Remarkably, it also influences the mobility of holes in P3HT infiltrated into the non-sintered inorganic layer. The reasons for the latter mechanism will be discussed in the second part of this section. The mobility of nc- ZnO decreases by more than one order of magnitude with increasing doping concentration and remains nearly unaffected by the infiltration of P3HT. Unlike in the sintered system (see sec.6.2), two mobility plateaus were observed (see Fig. 6.30). The mobility stays at a nearly constant value of 2 to $3 \cdot 10^{-3}$ $cm^2V^{-1}s^{-1}$ for the undoped, the 0.8 at.% and the 2 at.% Al-doped ZnO. Also no significant change of the mobility could be observed for 5 to 10 at.% doping level. This effect is mainly attributed to scattering at crystal imperfections: The electron transport in *unsintered* nc-ZnO:Al is preferentially limited by scattering effects due to the reduced level of crystallinity in the doped material, additional defect formation due to doping does not seem to have a drastic effect on the mobility. It is worth mentioning that the unsintered layers are X-ray amorphous. The values for σ and the corresponding charge carrier density n of around 10^{-4} $\Omega^{-1}m^{-1}$ and 10^{17} cm^{-3} are rather low for ZnO:Al due to the omitted sintering step and, therefore, the low level of crystallinity. Also, errors due to the contact resistance cannot be neglected. However, this effect is expected to be small due to the large channel length, i.e., the transport within the semiconductor limits the current between source and drain. The hole mobility was found to depend on the Al-doping level of nc-ZnO. The origin of this behavior will be discussed below:

(i) The hole transport is assumed to occur solely in P3HT, e.g., the differences of the surface properties in undoped and doped zinc oxide layers has an influence on the morphology of the polymer. The hole mobility is further influenced by the morphology of the P3HT itself, i.e. determined by the degree of π-π-stacking and also by the relative orientation to the substrate because of the anisotropy of charge transport [66]. In this respect and in view of the hybrid system the nanostructure and hence the mobility of the infiltrated polymer will benefit from the porous topology of nc-ZnO via ordered chain aggregation. The absorption spectra revealed strong indication of interchain absorption and, among all investigated hybrid systems, a similar vibronic structure and therefore a similar degree of short range order in the P3HT phase.

(ii) The porosity of nc-ZnO determines the ability to infiltrate P3HT. The hole mobility sensitively depends on the roughness of the Al-doped ZnO layers. XRR spectra exhibit a strong correlation of the organic/inorganic interface layer and the chosen doping level. The sample with 2 at.% doping shows a high degree of phase intermixing, i.e., an interface thickness of around 18.6 nm (see Fig. 6.32) and also the highest hole mobility (see Fig. 6.30) within the set of doping levels. Treating SiO_2 and ZnO:Al as two capacitors in series for the accumulation of holes in P3HT (ZnO:Al becomes depleted) a higher level of intermixing results in a smaller thickness of the dielectric. Hence, as the mobility is indirectly proportional to the thickness of the dielectric, the thickness variation due to a stronger intermixing can be one explanation for the behavior of the hole mobility. But, unless the interface roughness is much higher for 2 at.%-doped ZnO the thickness of the oxide layer in the case of hole accumulation is decreased by less than 10 % compared to higher and lower doping levels. This means that the value of the

hole mobility, derived from Eq. (4.7) (assuming a constant thickness of the dielectric for the various doping levels) would show a 10 % increase compared to smoother interfaces. Hence, the effective thickness of the dielectric alone cannot explain the origin of the hole-mobility dependence on the doping level of ZnO. Nevertheless, the highest roughness value coincides with the highest hole mobility value.

(iii) The polarizability of the dielectric, i.e. ZnO:Al in the case of hole accumulation, influences the mobility of accumulated positive carriers at the organic/inorganic interface. Fröhlich polarons, reported for organic single crystals on different dielectrics by Hulea *et al.*[59], where the mobility depends on the value of the dielectric constant of the oxide, cannot describe μ_p *vs. doping level*, due to the necessity of a largely varying dielectric constant with doping level. However, a $\mu \sim 1/\varepsilon$ behavior was found. A change in ε by almost two orders of magnitude would be mandatory to explain the results presented in this thesis, e.g. from 8 to 0.08. In the case of nc-ZnO, a change in ε from ~ 8 to ~ 11 [129] could be estimated, if a third phase, Al_2O_3, is present in a high percentage at the interface at high doping levels. Hence, Fröhlich polarons can be excluded from having a significant influence on the dependence of the hole mobility on the Al-doping level in nc-ZnO. On the other hand, the mobility in disordered organic semiconductors and especially in the respective FET structures was found to be diminished due to the systematic broadening of the Gaussian density of states with dipolar disorder at the semiconductor/dielectric interface due to the value of ε [103, 122]. This scenario can also be excluded from having a drastic influence, as the explanation of mobilty dependence on the doping level would imply unrealistic variations of the dielectric constant (see Section 6.1).

(iv) Defects or charged traps at the organic/inorganic interfaces generated by doping can positively or negatively influence the accumulated density of free holes. In order to achieve ambipolar behavior a balanced intrinsic carrier density of both charge carrier types is required [94]. If, e.g., the density of free electrons outbalances that of the holes, a higher negative gate voltage is needed in order achieve hole accumulation. The threshold voltage for electron transport in pure nc-ZnO:Al transistors has been investigated (Fig. 6.27(a)). It ranges between 15.5 V and 33.4 V for the undoped and the 0.8 at.% -doped nc-ZnO and for the 5 at.%-doped system, respectively, which reflects the doping dependence of n. The threshold voltage for hole accumulation (Fig. 6.30), which qualitatively indicates the density of intrinsic carriers and trap states, shows some correlation with the hole mobility, but appears to be too complex to be quantitatively explained. The trap scenario is affirmed by the fact that a low threshold voltage for electrons results in a high V_{th} for holes after application of P3HT. The free-electron density n reaches a maximum in the 0.8 at.% and also in the 10 at.% Al-doped samples. In both cases low hole mobilities were observed, i.e. at $2.0 \cdot 10^{-5}$ cm^2/Vs and $2.7 \cdot 10^{-6}$ cm^2/Vs. A lower mobility value for the highest doping level is attributed to the doping-induced formation of additional traps. The lowest charge carrier density was estimated to be $1.0 \cdot 10^{16}$ cm^{-3} and was observed for the undoped ZnO, although 2 at.% Al-doping with $1.6 \cdot 10^{16}$ cm^{-3} and 5 at.% with $1.8 \cdot 10^{16}$ cm^{-3} do not present a significant difference. If only the free electron density was responsible for the hole-mobility dependence on the doping level of nc-ZnO, the highest hole mobility should be observed in case of >2 at.% Al-doping, which could not be confirmed. Here, an interplay of different parameters, mainly the P3HT/ZnO:Al intermixing (ii) *and* the free electron density in ZnO:Al (iv), causes the maximum hole mobility at 2 at.% Al doping. Interestingly, a minimum in σ, i.e., minimum in $\mu \cdot n$ can be found for the 5 at.% Al-doped sample, where indeed *balanced* electron and hole mobilities were observable after intrusion of P3HT. Nevertheless,
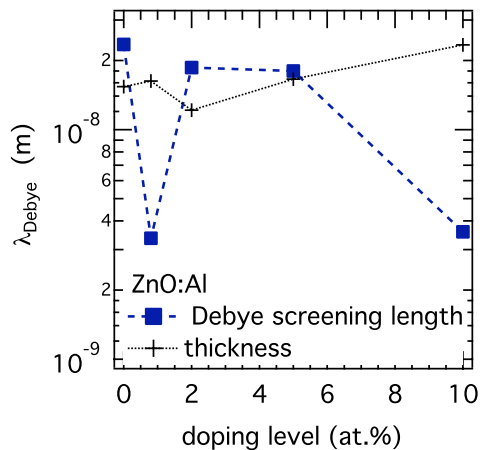
Abbildung 6.33: Comparison of the Debye screening length and the ZnO:Al layer thicknes at various doping levels. The accumualtion of holes is assumed to be most efficient when the electrons in ZnO:Al are repelled and pushed towards the P3HT interface.

the *highest* hole mobility was observed for 2 at.% Al-doping. The Debye screening length in ZnO:Al with 0, 2, and 5 at .% , i.e., at the moderate electron densities of about 10^{16} cm^{-3} , amounts to 20 nm as illustrated in Fig. 6.33. This extends over the ZnO:Al thickness and hence, the free electrons will be repelled from the dielectric to the P3HT/ZnO:Al interface. In the case of the 2 at.%- doped sample, where the highest degree of intermixing was observed, local field enhancement at the P3HT/oxide interface and therefore improved injection and accumulation of holes is expected.

Conclusion

Ambipolar charge transport in a hybrid organic/inorganic transistor consisting of the polymer P3HT and the sol-gel-synthesized undoped and Al-doped nanocrystalline ZnO was demonstrated. The influence of doping of ZnO on its electron mobility and also on the hole mobility in P3HT was discussed. The maximum conductivity in non-sintered ZnO has been reached for 0.8 at.% Al-doping and also doping strongly affects the density of free electrons. The electron mobility decreases with increasing doping level and remains nearly unaffected upon the infiltration of the organic component. Remarkably, the hole mobility has been found to depend on the Al-doping level of ZnO. The hole mobility reaches its maximum at the doping level of 2 at.%. After evaluation of several physical explanations, this effect was attributed to an enhanced intermixing of ZnO:Al and P3HT as confirmed via X-ray reflectivity data. In conclusion the infiltration of the ZnO:Al phase with P3HT is a necessary prerequisite for achieving a proper electronic interaction between the two components. In particular the Al-doping of nanocrystalline ZnO allows to control the equilibrium electron concentration and the morphology, which means that intermixing of the two semiconductors can be controlled via doping and, hence, a balanced electron and hole mobility can be adjusted in P3HT/ZnO:Al hybrids. This is the fundamental precondition for the implementation of hybrid field effect transistors in organic electronics.

7 Summary and Conclusion

The charge transport properties of disordered organic and nanocrystalline inorganic semiconductors as well as their combinations have been investigated in regard to the charge carrier density employing field-effect-transistor structures. The results were discussed in the framework of different theoretical models as presented in Sections 3.1.1 and 3.1.2.

In organic semiconductors the presence of positional and energetic disorder determines the transport of charges through the respective thin films and interfaces. The electronic disorder is characterized by statistically distributed and localized transport sites which were shown to form a Gaussian density of states. In this electronic environment the charge transport occurs via thermally activated hopping between the localized states and therefore depends on the temperature and the local electric field. Particularly, a dependence of the carrier mobility on the charge carrier concentration is observed due to filling of tail states. Inorganic nanocrystalline semiconductors, however, are expected to present a different electronic structure: Within the volume of a nanocrystallite the semiconductor is assumed to reflect the electronic properties of the crystalline bulk material. However, the outer shell is characterized by a relatively large density of surface states and correspondingly bending of the energy bands, which creates an energetic barrier between the adjacent particles. In a nanocrystalline thin film this characteristic can be rate-limiting for the inter-particle carrier transport as reflected by reduced charge carrier mobility. The effective barrier height can be reduced by controlled doping of the nanocrystals which results in improved majority carrier transfer rates across the barrier. However, doping results in the simultaneous increase of the defect density and consequently to enhanced limitation of the mobility due to charge carrier scattering.

In the experiments, thin films of commercially available p- and n-type organic semiconductors (P3HT, and two derivatives of PCBM) were investigated in field-effect transistor structures. Further, sol–gel synthesized n-type nanocrystalline-ZnO (nc-ZnO) with varied doping concentration (agent: aluminum Al^{3+}) was introduced in order to establish an alternative way of customizing the charge transport properties of the neat material and in combination with the organic polymer semiconductor P3HT.

While the hole transport in P3HT was found to occur via hopping in a Gaussian density of states [50, 119], the density of states in methanofullerene thin film FETs was so far considered to be best described by an exponential distribution at medium carrier densities and, contrarily, by a Gaussian function at low carrier densities. By investigating the electron transport in field-effect transistors based on [60]PCBM and [70]PCBM in terms of the charge carrier density and temperature, the data were consistently expressed in the framework of the extended energy correlated Gaussian disorder model. For both fullerene derivates an increase of the mobility with increasing carrier density up to a maximum of $2 \cdot 10^{-2}$ cm^2/Vs at moderate charge carrier densities of $n=10^{18}$cm^{-3} was observed at room temperature. However, further enhancement of the carrier density results in a decrease of the mobility. The temperature dependent measurements of the respective mobility revealed two different transport regimes with a transition at T=160 K.

The dependence of the charge carrier density on the gate potential and the vertical variation in distance from the dielectric was derived from Poisson's equation considering a Gaussian density of states: While the carriers are spread over the sample at low gate voltages, most of the carriers are located near the dielectric at high gate voltages.

A significant decrease of the electron mobility was observed at higher carrier concentrations. Ruling out an underestimated electron density and dipolar disorder broadening near the dielectrics (which would have the most pronounced effect at high gate voltages), the mobility decrease at high carrier densities was attributed to long-range Coulomb repulsion among the charge carriers.

The electron transport in thin films of sol–gel processed nc-ZnO was studied regarding the impact of the charge carrier density introduced via accumulation in FETs as well as by Al-doping. This approach allowed for assessing scattering effects on the electron mobility due to extrinsic doping. The increasing accumulation of charge carriers results in higher electron mobilities. In contrast, decreasing mobilities were observed at higher doping densities. The activation energy for the charge transport as well as the mean-free path was derived from temperature dependent mobility measurements. The extrinsic doping initially leads to a lowering of the activation energy, followed by its increase due to doping–induced structural defects. However, the mobility did not show a clear dependence on the activation energy and the average crystallite size as determined from X-ray diffraction studies. This was attributed to the reduction of the mean-free path due to doping. The electrical conductivity is governed by the interplay of the enhanced charge carrier density and the doping-induced charge carrier scattering.

The requirements for achieving balanced charge carrier mobilities in field-effect transistors based on p- and n-type semiconductor combinations have been evaluated. The properties of the combinations are only to some extent dictated by the characteristics of the neat materials. Instead, their arrangement, in particular relative to the dielectric, requires specific attention.

In this regard, blending ratios of P3HT and PCBM, commonly used as donor and acceptor materials in organic solar cells, have been adjusted in order to achieve ambipolar transport in P3HT:PCBM-based field-effect transistors. As the neat materials exhibit similar mobility values on SiO_2 surfaces, a naive conclusion would suggest similar compositions for the realization of balanced electron and hole mobilities in field-effect transistors. However, the dielectric-semiconductor interface seems to become depleted of one phase and, hence, the surface composition may substantially differ from that of the bulk.

In this thesis an alternative approach for achieving ambipolar transistors was suggested by substituting PCBM with nc-ZnO:Al. Doping of nc-ZnO was shown to be a tool to control the charge transport in nc-ZnO/P3HT hybrids, using one single injecting metal (gold bottom contacts) on a SiO_2 dielectric. As the electron mobility in undoped nc-ZnO is higher than the hole mobility in P3HT, a direct route towards balanced charge transport could be that the doping-induced electron mobility degradation in nc-ZnO:Al balances the mobilities in combinations of the two semiconductors. Remarkably, the hole mobility has been found to be sensitive to the Al-doping level in nc-ZnO. Al-doping enforces a morphological change of the nanoparticular zinc oxide layer which enables the infiltration of P3HT into the inorganic matrix. X-ray reflectivity measurements confirm the desired change of the interface morphology for the various doping levels. After evaluation of several physical reasons, this effect was attributed to an enhanced intermixing of ZnO:Al and P3HT as confirmed by X-ray reflectivity data.

As an overall conclusion, the specific geometry of field-effect transistors provides a straight-

forward way of probing the charge carrier mobility in dependence of the charge carrier density in solution-processed organic and inorganic semiconductors as well as in their combinations. It should be stressed that the technique is rather sensitive to the actual properties of the semiconductor-dielectric interface, i.e. the compositional and electrostatic interaction of the components. Hence, results on electronic properties of semiconductor systems elaborated in FET structures may provide information on the interface properties relevant for application of these materials in other device structures such as diodes and solar cells.

8 Zusammenfassung

Der Ladungstransport in ungeordneten organischen und nanokristallinen anorganischen Halbleitern sowie in deren Mischsystemen wurde im Hinblick auf die Ladungsträgerdichte in Feldeffekttransistoren untersucht. Die Ergebnisse wurden anhand verschiedener theoretischer Modelle, wie in den Abschnitten 3.1.1 und 3.1.2 gezeigt, diskutiert.

In organischen Halbleitern bestimmt die räumliche und energetische Unordnung den Ladungstransport durch die jeweiligen dünnen Schichten und Grenzflächen. Dabei ist die elektronische Unordnung charakterisiert durch statistisch verteilte und lokalisierte Transportzustände, die eine Gaußsche Zustandsdichte zeigen. In dieser elektronischen Umgebung ist der Ladungstransport durch thermisch aktiviertes Hüpfen zwischen lokalisierten Zuständen gekennzeichnet und hängt demzufolge von der Temperatur und dem lokalen elektrischen Feld ab. Insbesondere wurde eine Abhängigkeit der Mobilität von der Ladungsträgerdichte beobachtet, was eine Folge des Füllens energetisch tief liegender Zustände ist.

Anorganische nanokristalline Halbleiter zeigen eine andere elektronische Struktur: Im Volumen des Nanokristalls kann man vereinfacht die elektrischen Eigenschaften des jeweiligen Einkristalls annehmen. Jedoch ist die äußere Hülle durch eine relativ hohe Dichte an Oberflächenzuständen und einer damit einhergehenden Energiebandverbiegung charakterisiert. Daher ergibt sich eine Energiebarriere zwischen den angrenzenden Kristalliten. In nanokristallinen dünnen Schichten kann diese Eigenschaft den Ladungstransport limitieren, was durch eine verringerte Beweglichkeit widergespiegelt wird. Die effektive Barrierenhöhe kann durch kontrollierte Dotierung der Nanokristalle vermindert werden, was die Transferraten über die Barriere erhöht. Jedoch führt Dotierung gleichzeitig zu einer Zunahme der Defektdichte und folglich zu einer weiteren Minderung der Beweglichkeit durch Streuprozesse der Ladungsträger.

In den hier gezeigten Experimenten wurden dünne Schichten bestehend aus kommerziell erhältlichen organischen p- und n-Halbleitern (P3HT und zwei Derivate von PCBM) in Feldeffekttransistorstrukturen untersucht. Des weiteren wurde Sol–Gel synthetisiertes n-leitendes nanokristallines ZnO (nc-ZnO) mit variiertem Aluminium Dotierlevel eingeführt, was einen alternativen Weg aufzeigt, die Eigenschaften des Ladungstransports sowohl im reinen Material als auch in dessen Kombination mit dem organischen Polymer P3HT einzustellen.

Während bereits in früheren Arbeiten gezeigt wurde, dass der Lochtransport in P3HT durch Hüpfen in einer Gaußschen Zustandsdichte charakterisiert ist [50, 119], wurde bisher in der Literatur eine Zustandsdichte mit exponentieller Form für Methanofulleren-Feldeffekttransistoren, also bei erhöhten Ladungsträgerdichten, angenommen. In Dioden bei niedrigen Ladungsträgerdichten hingegen ging man von einer Gaußförmigen Zustandsdichte aus. Durch die Untersuchung des Ladungstransports in [60]PCBM und [70]PCBM in Abhängigkeit von der Temperatur und der Ladungsträgerdichte konnten die Daten in dieser Arbeit konsistent im Rahmen des Gaußschen Unordnungsmodells mit energetisch korrelierten Zuständen beschrieben werden. Für beide Fullerenderivate nimmt die Mobilität bei Raumtemperatur bis zu einem Maximum von $2 \cdot 10^{-2}$ cm^{2}V^{-1}s^{-1} bei mittleren Ladungsträgerdichten von $n=10^{18}$cm^{-3} zu. Bei höheren

Ladungsträgerdichten sinkt die Mobilität wieder. Die temperaturabhängigen Daten der Mobilität zeigten zwei verschiedene Transportregime mit einem Übergang bei T=160 K. Die Abhängigkeit der Ladungsträgerdichte vom Gate-Potential und die vertikale Variation gemäß der Entfernung vom Dielektrikum wurden aus der Lösung der Poisson Gleichung unter Berücksichtigung der Gaußschen Zustandsdichte hergeleitet: Während die Ladungsträger bei kleinen Gate-Spannungen über die Schicht verteilt sind, befinden sie sich bei hohen Gate-Spannungen nahe am Dielektrikum. Bei höheren Ladungsträgerdichten wurde ein deutliches Absinken der Mobilität beobachtet. Nach Ausschluss einer Überschätzung der Elektronendichte und einer Verbreiterung der Zustandsdichte verursacht durch Dipole im Dielektrikum (was einen größeren Effekt bei hohen Dichten hat), wurde das Absinken bei hohen Ladungskonzentrationen der langreichweitigen Coulomb Abstoßung zwischen den Ladungsträgern zugeschrieben.

Die Eigenschaften des Elektronentransports in dünnen Schichten bestehend aus Sol–Gel prozessiertem nc-ZnO wurden im Hinblick auf die Ladungsträgerdichte, die sowohl durch Anreicherung in FETs als auch durch Al-Dotierung variiert wurde, untersucht. Dieser Ansatz ermöglichte die Auswirkug der erhöhten Anzahl der Streuprozesse, verursacht durch extrinsische Dotierung, auf die Elektronenmobilität abzuschätzen. Akkumulation von Ladungsträgern führt zu höherer Elektronenbeweglichkeit. Im Gegensatz dazu wurden bei erhöter Dotierkonzentration verminderte Werte der Beweglichkeit beobachtet. Die Aktivierungsenergie für den Ladungstransport sowie die mittlere freie Weglänge wurden aus temperaturabhängigen Beweglichkeitsmessungen abgeleitet. Extrinsisches Dotieren führt zunächst zur Verringerung der Aktivierungsenergie, gefolgt von einem Anstieg, der strukturellen Defekten verursacht durch Dotierung zuzuschreiben ist. Die Mobilität zeigte aber keine klare Abhängigkeit von der Aktivierungsenergie und der aus Röntgenbeugungstudien ermittelten Kristallitgröße. Dies wurde der Verminderung der mittleren freien Weglänge innerhalb des Kristallits durch Dotierung zugeschrieben. Die elektrische Leitfähigkeit hängt also von einem Zusammenspiel der erhöhten Ladungsträgerdichte und der Ladungsträgerstreuung, verursacht durch Dotierung, ab.

Die Voraussetzungen für ausgeglichene Werte der Elektronen- und Lochbeweglichkeit in Feldeffekttransistoren basierend auf p- und n-Typ Halbleiterkombinationen wurden bestimmt. Die Eigenschaften dieser Kombinationen sind nur zu einem gewissen Grad durch die Eigenschaften der reinen Materialien bestimmt. Vielmehr fordert die Anordnung der Materialien zueinander und im speziellen relativ zum Dielektrikum besondere Aufmerksamkeit.

In diesem Zusammenhang wurden Mischungsverhältnisse von P3HT und PCBM, die verbreitet Nutzung in organischen Solarzellen finden, so angepasst, dass ambipolarer Ladungstransport in P3HT:PCBM-basierten Feldeffelttransistoren erreicht wurde. Da die reinen Materialien einen vergleichbaren Betrag der Beweglichkeit auf SiO_2 Oberflächen zeigen, würde man naiverweise erwarten, dass der gleiche Anteil beider Komponenten in der Mischung zu balancierter Beweglichkeit in Feldeffekttransistoren führt. Allerdings scheint die Halbleiter-Isolator Grenzfläche verarmt von einer der beiden Phasen zu sein, so dass sich die Oberflächenzusammenstellung substantiell von der Volumenkomposition unterscheidet.

In dieser Dissertation wurde ein alternativer Ansatz zum Erreichen ambipolarer Transistoren vorgeschalgen, nämlich durch Substitution von PCBM durch nc-ZnO:Al. Es wurde gezeigt, dass Dotieren von nc-ZnO ein Werkzeug darstellt, um den Ladungstransport im nc-ZnO/P3HT Hybridmaterial einzustellen, und zwar unter Benutzung nur eines Injektionsmetalls (Gold bottom-contact) auf einem SiO_2 Dielektrikum. Da die Elektronenmobilität in undotiertem nc-ZnO höher ist als die Lochbeweglichkeit in P3HT, wäre ein direkter Weg zu ausgeglichenem

Ladungstransport der, die Verminderung der Elektronenmobilität in nc-ZnO:Al durch Dotierung auszunutzen, um ausgeglichene Beweglichkeiten in einer Verbindung der beiden Halbleiter zu erreichen. Bemerkenswerterweise wurde aber eine Abhängigkeit der Lochmobiltät im P3HT vom Al-Dotierlevel im nc-ZnO:Al gefunden. Al-Dotierung ruft eine morphologische Veränderung hervor, die das Infiltrieren von P3HT in die anorganische Matrix ermöglicht. Röntgenreflektivitätsmessungen bestätigen die gewünschte Veränderung der Grenzflächenmorphologie mit der Dotierkonzentration. Nach Erwägung verschiedener physikalischer Erklärungsansätze wurde der Effekt der erhöhten Vermischung von ZnO:Al und P3HT zugeschrieben.

Kurzgefasst zeigt die Feldeffekttransistorgeometrie eine Möglichkeit auf, die Ladungsträgerbeweglichkeit in lösungsmittelprozessierten organischen und anorganischen Halbleitern sowie in deren Gemischen in Abhängigkeit von der Ladungsträgerdichte direkt zu untersuchen. Es soll hier noch einmal eindringlich darauf hingewiesen werden, dass die Methode relativ stark von den Grenzflächeneigenschaften abhängt. Insbesondere von der Wechselwirkung der Komponenten bezüglich ihrer relativen Anordnung und der Elektrostatitk. Das heisst, die Ergebnisse zu elektrischen Eigenschaften, die mithilfe von FET-Strukturen abgeleitet wurden, können Informationen über die Grenzflächenbeschaffenheit liefern, welche für die Anwendung dieser Materialien in anderen Bauteilen, wie Dioden und Solarzellen, von Relevanz sein können.

9 Outlook

Several aspects beyond the results of this thesis should be addressed in future work.

Disordered Semiconductors   The charge transport in PCBM could be consistently described within the framework of the energy correlated Gaussian disorder model [18]. Nevertheless, polaronic transition rates as well as long-range Coulomb interactions were, so far, neglected within the framework of the enhanced correlated disordered model. However, other approches which take into account Coulomb interactions neglect the energy-correlation of states [33, 75].

The results in this work demand the development of a model including the combination of

- energy-correlation of states,

- polaronic transition rates and

- long-range Coulomb interactions.

Doping of nanocrystalline-ZnO   The doping-dependent roughness enhancement in solution-processed nanocrystalline-ZnO:Al had a remarkable influence on the performance of the ambipolar transport in FETs based on combinations of the inorganic semiconductor with P3HT. Nevertheless, the origin of the morphological modification remains unclear. As the roughness increases with doping and peaks at 2 at.% while very smooth interfaces were achieved at high doping levels. Partly, this circumstance originates in the phase transition from the crystalline to the amorphous phase. However, the preferential columnar growth at 2 at.% doping concentration remains unclear.

Hybrid organic/inorganic semiconductors   Via experiments on hybrid organic/inorganic FET structures the relevance of the surface roughness and the screening length of the inorganic material for the charge transport characteristics in the organic semiconductor phase was demonstrated. It was pointed out that local field enhancement at the organic/inorganic interface results in enhanced accumulation of holes. This finding should be further confirmed with scanning probe techniques like surface-potential measurements or scanning tunneling spectroscopy, as it suggests an alternative path for achieving high carrier densities.

Literaturverzeichnis

[1] M. J. Alam and D. C. Cameron. Preparation and properties of transparent conductive aluminium-doped zinc oxide thin films by sol-gel process. The 47th international symposium: Vacuum, thin films, surfaces/interfaces, and processing NAN06, 19:1642, 2001.

[2] V. Ambegaokar, B. I. Halperin, and J. S. Langer. Hopping conductivity in disordered systems. *Phys. Rev. B*, 4:2612, 1971.

[3] R. L. Anderson. Experiments on Ge-GaAs heterojunctions. *Sol. State Electron.*, 5:341, 1962.

[4] T. Ando, A. B. Fowler, and F. Stern. Electronic properties of two-dimensional systems. *Rev. Mod. Phys.*, 54:437, 1982.

[5] T. D. Anthopoulos, D. M. de Leeuw, E. Cantatore, J. Alma, and J. C. Hummelen. Solution processible organic transistors and circuits based on a C_{70} methanofullerene. *J. Appl. Phys.*, 98:054503, 2005.

[6] T. D. Anthopoulos, D. M. de Leeuw, E. Cantatore, S. Setayesh, E. J. Meijer, C. Tanase, J. C. Hummelen, and P. W. M. Blom. Organic complementary-like inverters employing methanofullerene-based ambipolar field-effect transistors. *Appl. Phys. Lett.*, 85:4205, 2004.

[7] V. I. Arkhipov, E. V. Emelianova, and G. J. Adriaenssens. Effective transport energy versus the energy of most probable jumps in disordered hopping systems. *Phys. Rev. B*, 64:125125, 2001.

[8] V. I. Arkhipov, E. V. Emelianova, Y.H. Tak, and H. Bässler. Charge injection into light emitting diodes: Theory and experiment. *J. Appl. Phys.*, 84:848, 1998.

[9] V. I. Arkhipov, U. Wolf, and H. Bässler. Current injection from a metal to a disordered hopping system. II. comparison between analytic theory and simulation. *Phys. Rev. B*, 59:7514, 1999.

[10] G. Baccarani, B. Ricco, and G. Spadini. Transport properties of polycrystalline silicon films. *J. Appl. Phys.*, 49(11):5565, 1978.

[11] Z. Bao, A. Dodabalapur, and A. J. Lovinger. Soluble and processable regioregular poly(3-hexylthiophene) for thin film field-effect transistor applications with high mobility. *Appl. Phys. Lett.*, 69:4108, 1996.

[12] S. D. Baranovskii, H. Cordes, F. Hensel, and G. Leising. Charge-carrier transport in disordered organic solids. *Phys. Rev. B*, 62:7934, 2000.

[13] H. Bässler. Charge transport in disordered organic photoconductors — A Monte Carlo simulation study. *Phys. Stat. Sol. B*, 175:15, 1993.

[14] A. Baumann, J. Lorrmann, C. Deibel, and V. Dyakonov. Bipolar charge transport in poly(3-hexyl thiophene)/methanofullerene blends: A ratio dependent study. *Appl. Phys. Lett.*, 93:252104, 2008.

[15] W. J. E. Beek, L. H. Slooff, M. M. Wienk, J. M. Kroon, and R. A. J. Janssen. Hybrid solar cells using a zinc oxide precursor and a conjugated polymer. *Adv. Funct. Mater.*, 15:1703, 2005.

[16] W. J. E. Beek, M. M. Wienk, and R. A. J. Janssen. Efficient hybrid solar cells from zinc oxide nanoparticles and a conjugated polymer. *Adv. Funct. Mater.*, 12:1009, 2004.

[17] M. Berggren, D. Nilsson, and N. D. Robinson. Organic materials for printed electronics. *Nat. Mater.*, 6:3, 2007.

[18] M. Bouhassoune, S.L.M. van Mensfoort, P.A. Bobbert, and R. Coehoorn. Carrier-density and field-dependent charge-carrier mobility in organic semiconductors with correlated gaussian disorder. *Org. Electron.*, 10:437, 2009.

[19] W. L. Bragg. The crystalline structure of zinc oxide. *Phil. Mag.*, 39:649, 1920.

[20] L.J. Brillson. The structure and properties of metal-semiconductor. *Surface Science Reports*, 2:123, 1982.

[21] P. J. Brown, D. S. Thomas, A. Köhler, J. S. Wilson, J.-S. Kim, C. M. Ramsdale, H. Sirringhaus, and R. H. Friend. Effect of interchain interactions on the absorption and emission of poly(3-hexylthiophene). *Phys. Rev. B*, 67:064203, 2003.

[22] L.L. Chang. The conduction properties of Ge-GaAs$_{1-x}$P$_x$ $n-n$ heterojunctions. *Solid-State Electronics*, 8(9):721, 1965.

[23] T. A. Chen, X. Wu, and R. D. Rieke. Regiocontrolled synthesis of poly(3-alkylthiophenes) mediated by Rieke Zinc: Their characterization and solid-state properties. *J. Am. Chem. Soc.*, 117:233, 1995.

[24] H.-C. Cheng, C.-F. Chen, and Chien-Yie Tsay. Transparent ZnO thin film transistor fabricated by sol-gel and chemical bath deposition combination method. *Appl. Phys. Lett.*, 90:012113, 2007.

[25] D. Chirvase, J. Parisi, J. C. Hummelen, and V. Dyakonov. Influence of nanomorphology on the photovoltaic action of polymer–fullerene composites. *Nanotechn.*, 15:1317, 2004.

[26] L.-L. Chua, J. Zaumseil, J.-F. Chang, E. C.-W. Ou, P. K.-H. Ho, H. Sirringhaus, and R. H. Friend. General observation of n-type field-effect behaviour in organic semiconductors. *Nature*, 434:194, 2005.

[27] R. Coehoorn, W. F. Pasveer, P. A. Bobbert, and M. A. J. Michels. Charge-carrier concentration dependence of the hopping mobility in organic materials with gaussian disorder. *Phys. Rev. B*, 72(15):155206, Oct 2005.

[28] V. Coropceanu, J. Cornil, D. A. da Silva Filho, Y. Olivier, R. Silbey, and J.-L. Brédas. Charge transport in organic semiconductors. *Chem. Rev.*, 2007.

[29] E. A. Davis and N. F. Mott. Conduction in non-crystalline systems v. conductivity, optical absorption and photoconductivity in amorphous semiconductors. *Philosophical Magazine*, 22:903, 1970.

[30] C. G. Van de Walle. Hydrogen as a cause of doping in zinc oxide. *Phys. Rev. Lett.*, 85(5):1012, 2000.

[31] C. Deibel, D. Mack, J. Gorenflot, A. Schöll, S. Krause, F. Reinert, D. Rauh, and V. Dyakonov. Energetics of excited states in the conjugated polymer poly(3-hexylthiophene). *Phys. Rev. B*, 81:085202, 2010.

[32] C. Deibel, A. Wagenpfahl, and V. Dyakonov. Influence of charge carrier mobility on the performance of organic solar cells. *Phys. Stat. Sol.*, page 1, 2008.

[33] L. Demeyu and S. Stafström. Monte Carlo simulations of charge carrier mobility in semiconducting polymer field-effect transistors. *Phys. Rev. B*, 76:155202, 2007.

[34] R. Devi, P. Purkayastha, P. K. Kalita, and B. K. Sarma. Synthesis of nanocrytsalline CdS thin films in pva matrix. *Bull. Mater. Sci.*, 30:123, 2007.

[35] K. Ellmer and R. Mientus. Carrier transport in polycrystalline transparent conductive oxides: A comparative study of zinc oxide and indium oxide. *Thin Solid Films*, 516:4620, 2008.

[36] K. Ernst, A. Belaidi, and R. Könenkamp. Solar cell with extremely thin absorber on highly structured substrate. *Semicond. Sci. Technol.*, 18:475, 2003.

[37] I. I. Fishchuk, A. Kadashchuk, H. Bässler, and S. Nespurek. Nondispersive polaron transport in disordered organic solids. *Phys. Rev. B*, 67:224303, 2003.

[38] I. I. Fishchuk, A. K. Kadashchuk, J. Genoe, Mujeeb Ullah, H. Sitter, Th. B. Singh, N. S. Sariciftci, and H. Bässler. Temperature dependence of the charge carrier mobility in disordered organic semiconductors at large carrier concentrations. *Phys. Rev. B*, 81:045202, 2010.

[39] S. R. Forrest. The path to ubiquitous and low-cost organic electronic appliances on plastic. *Nature*, 428:911, 2004.

[40] D. S. Germack, C. K. Chan, B. H. Hamadani, L. J. Richter, D. A. Fischer, D. J. Gundlach, and D. M. DeLongchamp. Substrate-dependent interface composition and charge transport in films for organic photovoltaics. *Appl. Phys. Lett.*, 94:233303, 2009.

[41] W. D. Gill. Drift mobilities in amorphous charge-transfer complexes of trinitrofluorenone and poly-n-vinylcarbazole. *J. Appl. Phys.*, 43:5033, 1972.

[42] J. Gilot, I. Barbu, M. M. Wienk, and R. A. J. Janssen. The use of ZnO as optical spacer in polymer solar cells: Theoretical and experimental study. *Appl. Phys. Lett.*, 91(11):113520, 2007.

[43] J. Gilot, M. M. Wienk, and R. A. J. Janssen. Double and triple junction polymer solar cells processed from solution. *Appl. Phys. Lett.*, 90:143512, 2007.

[44] M. Grundmann. *The Physics of Semiconductors: An Introduction Including Devices and Nanophysics*. Springer, Berlin, 1 edition, 2006.

[45] Z-L. Guan, J. B. Kim, H. Wang, C. Jaye, D. A. Fischer, Y.-L. Loo, and A. Kahn. Direct determination of the electronic structure of the poly(3-hexylthiophene):phenyl-[6,6]-C_{61} butyric acid methyl ester blend. *Org. Electron.*, 11:1779, 2010.

[46] D. J. Gundlach, L. Zhou, J. A. Nichols, T. N. Jackson, P. V. Necliudov, and M. S. Shur. An experimental study of contact effects in organic thin film transistors. *J. Appl. Phys.*, 100:024509, 2006.

[47] A. Hadipour, B. de Boer, and P. W. M. Blom. Organic tandem and multi-junction solar cells. *Adv. Funct. Mater.*, 18(2):169, 2008.

[48] B. H. Hamadani and D. Natelson. Nonlinear charge injection in organic field-effect transistors. *J. Appl. Phys.*, 97:064508, 2005.

[49] I. W. Hamley and J. S. Pedersen. Analysis of neutron and X-ray reflectivity data. I. Theory. *J. Appl. Cryst.*, 27:29, 1994.

[50] M. S. Hammer. Ladungsträgermobilität in organischen Halbleitern. Diploma thesis, Universität Würzburg, 2006.

[51] M. S. Hammer, D. Rauh, V. Lorrmann, C. Deibel, and Vladimir Dyakonov. Effect of doping- and field-induced charge carrier density on the electron transport in nanocrystalline ZnO. *Nanotechn.*, 19:485701, 2008.

[52] I. G. Hill. Numerical simulations of contact resistance in organic thin-film transistors. *Appl. Phys. Lett.*, 87:163505, 2005.

[53] D. M. Hofmann, A. Hofstaetter, F. Leiter, H. Zhou, F. Henecker, and B. K. Meyer. Hydrogen: A Relevant Shallow Donor in Zinc Oxide. *Phys. Rev. Lett.*, 88:045504, 2002.

[54] G. Horowitz, M. E. Hajlaoui, and R. Hajlaoui. Temperature and gate voltage dependence of hole mobility in polycrystalline oligothiophene thin film transistors. *J. Appl. Phys.*, 87:4456, 2000.

[55] G. Horowitz, R. Hajlaoui, H. Bouchriha, R. Bourguiga, and M. Hajlaoui. The concept of threshold voltage in organic field-effect transistors. *Adv. Mater.*, 10:923, 1998.

[56] G. Horowitz, R. Hajlaoui, D. Fichou, and A. El Kassmi. Gate voltage dependent mobility of oligothiophene field-effect transistors. *J. Appl. Phys.*, 85:3202, 1999.

[57] F. M. Hossain, J. Nishii, S. Takagi, A. Ohtomo, T. Fukumura, H. Fujioka, H. Ohno, H. Koinuma, and M. Kawasaki. Modeling and simulation of polycrystalline ZnO thin-film transistors. *J. Appl. Phys.*, 94:7768, 2003.

[58] F. M. Hossain, J. Nishii, S. Takagi, T. Sugihara, A. Ohtomo, T. Fukumura, H. Koinuma, H. Ohno, and M. Kawasaki. Modeling of grain boundary barrier modulation in ZnO invisible thin film transistors. *Physica E*, 21:911, 2004.

[59] I. N. Hulea, S. Fratini, H. Xie, C. L. Mulder, N. N. Iossad, G. Rastelli, S. Ciuchi, and A. F. Morpurgo. Tunable Fröhlich polarons in organic single-crystal transistors. *Nat. Mater.*, 5:982, 2006.

[60] J. C. Hummelen, B. W. Knight, F. LePeq, F. Wudl, J. Yao, and C. L. Wilkins. Preparation and characterization of fulleroid and methanofullerene derivatives. *The Journal of Organic Chemistry*, 60:532, 1995.

[61] L. H. Jimison, M. F. Toney, I. McCulloch, M. Heeney, and A. Salleo. Charge-Transport Anisotropy Due to Grain Boundaries in Directionally Crystallized Thin Films of Regioregular Poly(3-hexylthiophene). *Adv. Mater.*, 21:1568, 2009.

[62] W. Jones. The measurement of particle size by the X-ray method. *Proc. R. Soc*, 166:16, 1938.

[63] K. Kaneto, M. Yano, M. Shibao, T. Morita, and W. Takashima. Ambipolar field-effect transistors based on poly(3-hexylthiophene)/fullerene derivative bilayer films. *Japan. J. Appl. Phys.*, 46:1736, 2007.

[64] O. Katz, Y. Roichman, G. Bahir, N. Tessler, and J. Salzman. Charge carrier mobility in field effect transistors: analysis of capacitance–conductance measurements. *Semicond. Sci. Tech.*, 20:90, 2005.

[65] M. Kimura, S. Inoue, T. Shimoda, and T. Sameshima. The effect of annealing processes on electronic properties of sol-gel derived Al-doped ZnO films. *Japan. J. Appl. Phys.*, 40:5237–5243, 2001.

[66] R. J. Kline and M. D. McGehee. Morphology and charge transport in conjugated polymers. *Polymer Reviews*, 46:27, 2006.

[67] R. J. Kline, M. D. McGehee, E. N. Kadnikova, J. Liu, and J. M. J. Fréchet. Controlling the Field-Effect Mobility of Regioregular Polythiophene by Changing the Molecular Weight. *Adv. Mater.*, 15:1519, 2003.

[68] C. Klingshirn. ZnO: Material, physics and applications. *Chem. Phys. Chem.*, 8:782, 2007.

[69] M. Koehler and I. Biaggio. Space-charge and trap-filling effects in organic thin film field-effect transistors. *Phys. Rev. B*, 70:045314, 2004.

[70] L. J. A. Koster, V. D. Mihailetchi, and P. W. M. Blom. Bimolecular recombination in polymer/fullerene bulk heterojunction solar cells. *Appl. Phys. Lett.*, 88:052104, 2006.

[71] L. J. A. Koster, W. J. van Strien, W. J. E. Beek, and P. W. M. Blom. Device Operation of Conjugated Polymer/Zinc Oxide Bulk Heterojunction Solar Cells. *Adv. Funct. Mater.*, 17(8):12971302, 2007.

[72] N. H. Langton and D. Matthews. The dielectric constant of zinc oxide over a range of frequencies. *British Journal of Applied Physics*, 9(11):453, 1958.

[73] C.-H. Lin, S.-C. Tseng, Y.-K. Liu, Y. Tai, S. Chattopadhyay, C.-F. Lin, J.-H. Lee, J.-S. Hwang, Y.-Y. Hsu, L.-C. Chen, W.-C. Chen, and K.-H. Chen. Suppressing series resistance in organic solar cells by oxygen plasma treatment. *Appl. Phys. Lett.*, 92:233302, 2008.

[74] D. C. Look, J. W. Hemsky, and J. R. Sizelove. Residual native shallow donor in ZnO. *Phys. Rev. Lett.*, 82(12):2552–2555, 1999.

[75] J. Lorrmann. Ladungstransport in ungeordneten organischen Halbleitern. Diploma thesis, Universität Würzburg, June 2008.

[76] R. A. Marcus. Electron transfer reactions in chemistry. theory and experiment. *Rev. Mod. Phys.*, 120:745, 1993.

[77] J. Marien. Field emission study of the specificity of zinc oxide polar surfaces (0001) and (0001). Work function and hydrogen adsorption. *Phys. Stat. Sol. A*, 38(2):513, 1976.

[78] R. Martins, P. Barquinha, A. Pimentel, L. Pereira, and E. Fortunato. Transport in high mobility amorphous wide band gap indium zinc oxide films. *Phys. Stat. Sol. A*, 202(9):R95–R97, 2005.

[79] R. D. McCullough. The chemistry of conducting polythiophenes. *Adv. Mater.*, 10:93, 1998.

[80] E. J. Meijer, D. M. de Leeuw, S. Setayesh, E. van Veenendaal, B.-H-Huisman, P. W. M. Blom, J. C. Hummelen, U. Scherf, and T. M. Klapwijk. Solution-processed ambipolar organic field-effect transistors and inverters. *Nat. Mater.*, 2:678, 2003.

[81] E. A. Meulenkamp. Synthesis and Growth of ZnO Nanoparticles. *J. Phys. Chem. B*, 102:5566, 1998.

[82] V. D. Mihailetchi, J. K. J. van Duren, P. W. M. Blom, J. C. Hummelen, R. A. J. Janssen, J. M. Kroon, M. T. Rispens, W. J. H. Verhees, and M. M. Wienk. Electron transport in a methanofullerene. *Adv. Funct. Mater.*, 13:43, 2003.

[83] A. Miller and E. Abrahams. Impurity conduction at low concentrations. *Phys. Rev.*, 120:745, 1960.

[84] D. B. Mitzi, L. L. Kosbar, C. E. Murray, M. Copel, and A. Afzali. High-mobility ultrathin semiconducting films prepared by spin coating. *Nature*, 428:299, 2004.

[85] N. F. Mott. Conduction in non-crystalline systems I. localized electronic states in disordered systems . *Phil. Mag.*, 19:835, 1969.

[86] Y. Natsume, H. Sakata, T. Hirayama, and H. Yanagida. Low-temperature conductivity of ZnO films prepared by chemical vapor deposition. *J. Appl. Phys.*, 72(9):4203–4207, 1992.

[87] A. Nelson. Co-refinement of multiple-contrast neutron/X-ray reflectivity data using mo-tofit. *J. Appl. Cryst.*, 39:273, 2006.

[88] K. Nomura, H. Ohta, A. Takagi, T. Kamiya, M. Hirano, and H. Hosono. Room-temperature fabrication of transparent flexible thin-film transistors using amorphous oxi-de semiconductors. *Nature*, 432:488, 2004.

[89] S. V. Novikov, D. H. Dunlap, V. M. Kenkre, P. E. Parris, and A. V. Vannikov. Essential role of correlations in governing charge transport in disordered organic materials. *Phys. Rev. Lett.*, 81:4472, 1998.

[90] S. B. Orlinskii, J. Schmidt, P.l G. Baranov, V. Lorrmann, I. Riedel, D. Rauh, and V. Dya-konov. Identification of shallow Al donors in Al-doped ZnO nanocrystals: EPR and ENDOR spectroscopy. *Phys. Rev. B*, 77:115334, 2008.

[91] A. Ortiz-Conde, F. J. García Sánchez, J. J. Liou, A. Cerdeira, M. Estrada, and Y. Yue. A review of recent MOSFET threshold voltage extraction methods. *J. Phys. Chem. B*, 42:583, 2001.

[92] J. W. Orton and M. J. Powell. The hall effect in polycrystalline and powdered semicon-ductors. *Reports on Progress in Physics*, 43(11):1263, 1980.

[93] G. Paasch and S. Scheinert. Space charge layers in organic field-effect transistors with gaussian or exponential semiconductor density of states. *J. Appl. Phys.*, 101:024514, 2007.

[94] B. N. Pal, P. Trottman, J. Sun, and H. E. Katz. Solution-deposited zinc oxide and zinc oxide/pentacene bilayer transistors: High mobility n-channel, ambipolar, and nonvolatile devices. *Adv. Funct. Mater.*, 18:1832, 2008.

[95] D. H-K. Pan and M. W. Prest. Surfaces of polymer blends: X-ray photoelectron spec-troscopy studies of polystyrene/poly(vinyl methyl ether) blends. *J. Appl. Phys.*, 58:2861, 1985.

[96] S. K. Park, Y.-H. Kim, and J.-I. Han. All solution-processed high-resolution bottom-contact transparent metal-oxide thin film transistors. *J. Phys. D: Appl. Phys.*, 42(12):125102, 2009.

[97] A. J. Parnell, A. D. F. Dunbar, A. J. Pearson, P. Staniec, A. J. C. Dennison, H. Hamamat-su, M. W. A. Skoda, D. G. Lidzey, and R. A. L. Jones. Depletion of PCBM at the cathode interface in P3HT/PCBM thin films as quantified via neutron reflectivity measurements. *Adv. Mater.*, 22:2444, 2010.

[98] L. G. Parratt. Surface studies of solids by total reflection of X-rays. *J. Appl. Cryst.*, 95:359, 1954.

[99] W. F. Pasveer, J. Cottaar, C. Tanase, R. Coehoorn, P. A. Bobbert, P. W. M. Blom, D. M. de Leeuw, and M. A. J. Michels. Unified description of charge-carrier mobilities in disordered semiconducting polymers. *Phys. Rev. Lett.*, 94:206601, 2005.

[100] G. K. Paul, S. Bandyopadhyay, and S. K. Sen. Transport properties of as-prepared al-doped zinc oxide films using sol-gel method. *Phys. Stat. Sol. A*, 191(2):509, 2002.

[101] J. S. Pedersen and I. W. Hamley. Analysis of neutron and X-ray reflectivity data. II. Constrained least-squares methods. *J. Appl. Cryst.*, 27:36, 1994.

[102] L. Pfeiffer and K. W. West. The role of MBE in recent quantum Hall effect physics discoveries. *Physica E*, 20:57, 2003.

[103] T. Richards, M. Bird, and H. Sirringhaus. A quantitative analytical model for static dipolar disorder broadening of the density of states at organic heterointerfaces. *J. Chem. Phys.*, 128:234905, 2008.

[104] P. Sagar, M. Kumar, and R. M. Mehra. Electrical and optical properties of sol-gel derived ZnO:Al thin films. *Materials Science-Poland*, 23:685, 2005.

[105] L. B. Schein. Comparison of charge transport models in molecularly doped polymers. *Phil. Mag. B*, 65:795, 1992.

[106] R. Schmechel, R. Ahles, and H. von Seggern. A pentacene ambipolar transistor: Experiment and theory. *J. Appl. Phys.*, 98:084511, 2005.

[107] T. Schuler and M. A. Aegerter. Optical, electrical and structural properties of sol gel ZnO:Al coatings. *Thin Solid Films*, 351(1–2):125–131, 1999.

[108] J. Y. W. Seto. The electrical properties of polycrystalline silicon films. *J. Appl. Phys.*, 46(12):5247, 1975.

[109] M. Shibao, T. Morita, W. Takashima, and K. Kaneto. Ambipolar Transport in Field-Effect Transistors Based on Composite Films of Poly(3-hexylthiophene) and Fullerene Derivative. *Jpn. J. Appl. Phys.*, 46:L123, 2007.

[110] W. Shockley. A unipolar field-effecttransistor. *Prog. Inst. Radio Engrs.*, 40:1365, 1952.

[111] M. Shur, M. Hack, and J. G. Shaw. A new analytic model for amorphous silicon thin-film transistors. *J. Appl. Phys.*, 66:3371, 1989.

[112] I. Sieber, N. Wanderka, I. Urban, I. Dörfel, E. Schierhornand F. Fenske, and W. Fuhs. Electron microscopic characterization of reactively sputtered ZnO films with different Al-doping. *Thin Solid Films*, 330:108, 1998.

[113] Th. B. Singh, N. Marjanović, P. Stadler, M. Auinger, G. J. Matt, S. Günes, N. S. Sariciftci, R. Schwödiauer, and S. Bauer. Fabrication and characterization of solution-processed methanofullerene-based organic field-effect transistors. *J. Appl. Phys.*, 97:083714, 2005.

[114] H. Sirringhaus, P. J. Brown, R. H. Friend, M. M. Nielsen, K. Bechgaard, B. M. W. Langeveld-Voss, A. J. H. Spiering, R. A. J. Janssen, E. W. Meijer, P. Herwig, and D. M. de Leeuw. Two-dimensional charge transport in self-organized, high-mobility conjugated polymers. *Nature*, 401:685, 1999.

[115] H. Sirringhaus, N. Tessler, and R. H. Friend. Integrated optoelctronic devices based on conjugated polymers. *Science*, 280:1741, 1998.

[116] E. C. P. Smits, S. G. J. Mathijssen, M. Cölle, A. J. G. Mank, P. A. Bobbert, P. W. M. Blom, B. de Boer, and D. M. de Leeuw. Unified description of potential profiles and electrical transport in unipolar and ambipolar organic field-effect transistors. *Phys. Rev. B*, 76:125202, 2007.

[117] V. Srikant and D. R. Clarke. On the optical band gap of zinc oxide. *J. Appl. Phys.*, 83:5447, 1998.

[118] S. M. Sze and K. N. Kwok. *Physics of semiconductor devices*. John Wiley & Sons Inc., USA, 3nd edition, 2007.

[119] C. Tanase, E. J. Meijer, P. W. M. Blom, and D. M. de Leeuw. Unification of the hole transport in polymeric field-effect transistors and light-emitting diodes. *Phys. Rev. Lett.*, 91:216601, 2003.

[120] N. Tessler, Y. Preezant, N. Rappaport, and Y. Roichman. Charge transport in disordered organic materials and its relevance to thin-film devices: A tutorial review. *Adv. Mater.*, 21:2741, 2009.

[121] B. P. Tyagi and K. Sen. Effective mobility of polycrystalline semiconductors. *Int. J. Electronics*, 58:83, 1985.

[122] J. Veres, S. D. Ogier, S. W. Leeming, D. C. Cupertino, and S. Mohialdin Khaffaf. Low-k insulators as the choice of dielectrics in organic field-effect transistors. *Adv. Funct. Mater.*, 13(3):199, 2003.

[123] M. C. J. M. Vissenberg and M. Matters. Theory of the field-effect mobility in amorphous organic transistors. *Phys. Rev. B*, 57:12964, 1998.

[124] E. von Hauff, V. Dyakonov, and J. Parisi. Study of field effect mobility in PCBM films and P3HT:PCBM blends. *Sol. Ener. Mat. Sol. Cells*, 87:149, 2005.

[125] E. von Hauff, J. Parisi, and V. Dyakonov. Investigations of the effects of tempering and composition dependence on charge carrier field effect mobilities in polymer and fullerene films and blends. *J. Appl. Phys.*, 100:043702, 2006.

[126] R. Winter, M. S. Hammer, C. Deibel, and J. Pflaum. Improvement of the poly-3-hexylthiophene transistor performance using small molecule contact functionalization. *Appl. Phys. Lett.*, 95:263313, 2009.

[127] P. H. Wöbkenberg, D. D.C. Bradley, D. Kronholm, J. C. Hummelen, D. M. de Leeuw, M. Cölle, and T. D. Anthopoulos. High mobility n-channel organic field-effect transistors based on soluble C_{60} and C_{70} fullerene derivatives. *Synth. Met.*, 158:468, 2008.

[128] S. W. Xue, X. T. Zu, W. G. Zheng, H. X. Deng, and X. Xiang. Effects of Al doping concentration on optical parameters of ZnO:Al thin films by sol-gel technique. *Physica B: Condensed Matter*, 381(1–2):209, 2006.

[129] K. F. Young and H. P.R. Frederikse. Compilation of the static dielectric constant of inorganic solids. *J. Phys. Chem Ref. Data*, 2:313, 1973.

[130] Ralph H. Young. Dipolar lattice model of disorder in random media analytical evaluation of the Gaussian disorder model. *Phil. Mag. B*, 72:435, 1995.

[131] G. Yu, J. Gao, J. C. Hummelen, F. Wudl, and A. J. Heeger. Polymer photovoltaic cells: enhanced efficiencies via a network of internal donor-acceptor heterojunctions. *Science*, 270:1789, 1995.

[132] Z. G. Yu, D. L. Smith, A. Saxena, R. L. Martin, and A. R. Bishop. Molecular geometry fluctuations and field-dependent mobility in conjugated polymers. *Phys. Rev. B*, 63:085202, 2001.

[133] J. Zaumseil and H. Sirringhaus. Electron and ambipolar transport in organic field-effect transistors. *Chem. Rev.*, 107:1296, 2007.

A Danksagung

Hiermit möchte ich mich bei allen bedanken, die dem Gelingen dieser Arbeit beigetragen haben. Zur Fertigstellung der Endfassung der Dissertation gehört natürlich ein langer Weg auf dem ich von vielen positiv beeinflusst wurde.

Natürlich gilt mein besonderer Dank Prof. Dr. Vladimir Dyakonov, der mir die Anfertigung einer Dissertation in diesem interessanten Gebiet der Physik ermöglicht hat. Insbesondere war er es, der in Fragen der Außendarstellung, wie bei Vorträgen oder Posterpräsentationen, die entscheidenden Fähigkeiten aus mir herausgelockt hat. Besonders hat er die Teilnahme an nationalen und internationalen Konferenzen gefördert.

Des weiteren möchte ich mich bei Prof. Dr. Jean Geurts für die interessierte Begutachtung meiner Arbeit bedanken und natürlich für die interessanten Diskussionen über den Einfluss lokaler und nicht-lokaler Schwingungsmoden auf den Ladungstransport.

Die Ergebnisse dieser Arbeit wurden zu großen Teilen mit Dr. Carsten Deibel diskutiert. Durch seine kritische Herangehensweise an neue Ergebnisse und sein penibles Lesen von Entwürfen wurden meine Arbeiten vorangetrieben.

Für besonders anregende und interessante Diskussionen möchte ich Prof. Dr. Jens Pflaum ganz herzlich danken. Durch sein Vertrauen in mein Experiment konnten wir in der Diskussion sehr weit in die Grundlagen einsteigen. Herzlichen Dank!

Ich durfte in drei Semestern bei der Vorlesung/dem Seminar zur Einführung in die Energietechnik bei Herrn Prof. Dr. Jochen Fricke assistieren. Es hat mir sehr viel Spaß gemacht, mit Herrn Fricke zusammenzuarbeiten. Zur gleichen Zeit hat die Veranstaltung meinen Horizont enorm erweitert und zwar nicht nur in physikalischer, sondern auch in politischer und gesellschaftlicher Hinsicht.

Die Arbeiten an P3HT Feldeffekttransistoren wurden tatkräftig und kompetent von der damaligen Diplomandin Rebecca Wörner (geb. Winter) durchgeführt. Außerdem hat Michael Schneider in seinem sechswöchigen Praktikum einen entscheidenden Beitrag zur Untersuchung an P3HT:PCBM blend Transistoren gegeben. Des weiteren möchte ich mich bei Nis Hauke Hansen für die interessanten Diskussionen und den Spaß im Labor bedanken.

Die wissenschaftliche Arbeit am Zink Oxid wurde durch Vorarbeiten von Dipl.-Phys. Daniel Rauh und Dr. Ingo Riedel ins Leben gerufen.

Ich danke Prof. Dr. Gernot Paasch (IFW Dresden) und Dr. Edit Bellet-Amalric (CEA-Grenoble, Frankreich) für wichtige Hinweise.

Ich bedanke mich bei bei Prof. Dr. Batke und Dipl.-Phys. Jürgen Schuster für die Ermöglichung, den Reinraum für die optische Lithographie zu benutzen, bei der Gruppe von Dr. Harald Graaf (TU Chemnitz) für gemeinsame Kelvin-Probe Studien und bei Dipl.-Phys. Pavo Vrdoljak (EP7 Uni Würzburg) für gemeinsame UPS bzw. XPS-Messungen.

Andrè Thiem-Riebe danke ich ganz besonders für kompetente Unterstützung in Sachen Technik und selbstverständlich für die Unterhaltungen über physikalische und unphysikalische Belange.

Des weiteren danke ich Dipl.-Phys. Julia Schafferhans für interessante Diskussionen und ihr Oberpfälzer Temperament.

Ich bedanke mich sehr herzlich beim ZAE für Unterstützung dieser Arbeit in finanzieller und experimenteller Hinsicht.

Wissenschaftliche Diskussionen im Transportgruppentreffen mit Dr. Carsten Deibel, Jens Lorrmann, Julia Schafferhans, Andreas Baumann und deren Diplomanden sind besonders hervorzuheben.

Außerdem danke ich Dipl.-Phys. Alexander Wagenpfahl für die interessanten Gespräche zum Ladungstransport.

Die freundliche und kompetente Soft- und Hardwareunterstützung durch Dipl.-Phys. Andreas Sperlich und Dipl.-Phys. Hannes Kraus verdient ein großes Lob.

Dipl.-Phys. Moritz Liedtke, der von Anfang an mit am Lehrstuhl war, danke ich für fachliche und weltliche Diskussionen.

M.Eng. Julien Gorenflot danke ich für die Suche nach der Photolumineszenz und seine wunderbare Art.

Dipl.-Phys. Valentin Baianov möchte ich für seine Unterstützung an den Aufbauten und für seinen einzigartigen Humor danken.

Außerdem möchte ich mich bei der gesamten EP6 für die schöne Zeit und die angenehme Atmosphäre bedanken.

Bei Ingo Riedel bedanke ich mich sehr herzlich für die seelische, moralische, physikalische und englische Unterstützung und für genaues Lesen der Doktorarbeit. Besonders hat er grenzenlose Freundlichkeit und abfärbende gute Laune.

Vielen Dank an meine Eltern Elisabeth und Johann Hammer und meine Schwester Barbara Hammer dafür, dass sie mich so weit gebracht haben und an mich glauben.

B Lebenslauf

Biographische Daten

Geburtstag	11. April 1982
Geburtsort	Hirschau
Nationalität	German
Familienstand	ledig

Adresse

Dienststelle	Experimentelle Physik VI
	Fakultät für Physik und Astronomie,
	Universität Würzburg
	Am Hubland
	D-97074 Würzburg
Telefon	
E-Mail	Maria.Hammer@physik.uni-wuerzburg.de
Privat	
Telefon	

Schulische Bildung

1988 –	1992	Grundschule Vilseck
1992 –	2001	Max-Reger-Gymnasium, Amberg
		Leistungskurse: Physik und Biologie

Studium

10/2001 – 11/2006 Diplomstudiengang Nanostrukturtechnik: Fakultät für Physik und Astronomie der Julius-Maximilians-Universität Würzburg, Diplomarbeit über die „Ladungsträgermobilität in organischen Halbleitern" bei Prof. Dr. Vladimir Dyakonov (Abschluss: Dipl.-Ing. Univ.)

Doktorarbeit

seit 1/2007 Fakultät für Physik und Astronomie der Universität Würzburg bei Prof. Dr. Vladimir Dyakonov

Lehre

	2006	Betreuung des Physikpraktikums für Chemiker (Dr. Rommel)
	2007	Betreuung des Physikpraktikums für Physiker (Prof. Dr. Ossau)
2008 –	2011	Übungsleiter zur Einführung in die Energietechnik (Prof. Dr. Fricke)

C List of Publications

Full Papers

- M. S. Hammer, D. Rauh, V. Lorrmann, C. Deibel, and V. Dyakonov. Effect of doping- and field-induced charge carrier density on the electron transport in nanocrystalline ZnO. *Nanotechn.* 19:485701, 2008

- R. Winter, M. S. Hammer, C. Deibel and J. Pflaum. Improvement of the poly(3-hexyl-thiophene) transistor performance using small molecule contact functionalization. *Appl. Phys. Lett.* 95:263313, 2009

- M. S. Hammer, C. Deibel, J. Pflaum and V. Dyakonov. Effect of doping of zinc oxide on the hole mobility of poly(3-hexylthiophene) in hybrid transistors. *Org. Electron.* 11:1569, 2010

- D. Reitzenstein, T. Quast, F. Kanal, M. Kullmann, S. Ruetzel, M. S. Hammer, C. Deibel, V. Dyakonov, T. Brixner and C. Lambert. Synthesis and electron transfer characteristics of a neutral low band gap mixed-valence polyradical. *Chem. Mater.* 22:6641, 2010

- M. S. Hammer, C. Deibel and V. Dyakonov. Reconsideration of the charge transport in [60]PCBM and [70]PCBM field effect transistors. *to be submitted*

- J. Pflaum, R. Winter, F. Wörner, M. S. Hammer, A. Wagenpfahl. Correlation between the effective contact resistance and the charge carrier transport in organic semiconductors of different mobility. *in preparation*

Contributed Talks

- DPG spring Meeting 2008, Berlin:

  M. S. Hammer, D. Rauh, I. Riedel, C. Deibel, and V. Dyakonov. Comparison of charge transport in organic P3HT and inorganic Al-doped zinc oxide nanoparticles

- EMRS Fall Meeting 2008, Warsaw: Transparent and Flexible Electronics: from Materials to Devices:

  M. S. Hammer, D. Rauh, C. Deibel, and V. Dyakonov. Balanced electron and hole mobility in organic/inorganic hybrid materials

- Physikerinnentagung 2008, Münster:

  M. S. Hammer, D. Rauh, C. Deibel, and V. Dyakonov. Charge transport in organic/inorganic hybrid solar cells

- DPG Spring Meeting 2009, Dresden:

  M. S. Hammer, D. Rauh, C. Deibel, and V. Dyakonov. Ambipolar organic/inorganic field effect transistor

- DPG Spring Meeting 2010, Regensburg:
  - M. S. Hammer, C. Deibel, V. Dyakonov. Electron mobility in methanofullerenes
  - R. Winter, F. Wörner, M. S. Hammer, C. Deibel, J. Pflaum. Correlation between the effective contact resistance and the charge carrier transport in organic semiconductors of different mobility

Poster presentations

- II-VI-Conference 2009, St. Petersburg:

  M. S. Hammer, C. Deibel, V. Dyakonov. Tuning the charge carrier density in nanocrystalline ZnO via Al doping and field effect

- MRS Fall Meeting 2009, Boston:

  M. S. Hammer, C. Deibel, V. Dyakonov. Adjusting ambipolar charge transport in a hybrid organic (P3HT)/inorganic (ZnO:Al) system

- DPG Spring Meeting 2006, Dresden:

  M. S. Hammer, C. Deibel, I. Riedel, V. Dyakonov. Field effect mobility of the polymer poly(3-hexylthiophene)

- DPG Spring Meeting 2007, Regensburg: Symposium organic electronics:

  M. S. Hammer, J. Schafferhans, I. Riedel, C. Deibel, V. Dyakonov. Temperature and gate-voltage dependent field effect mobility of the conjugated polymer Poly(3-Hexyl Thiophene)

Conference Papers

- I. Riedel, J. Ohland, J. Neerken, J. Keller, J. Parisi, M. S. Hammer, O. Kiowski, S. Spiering. Photodoping and band offsets in CIGS solar cells with varied buffer layers. *Proc. 25th EU PV SEC/ 5th WCPEC*, Valencia, Spain 2010

EHRENWÖRTLICHE ERKLÄRUNG

gemäß §5 Abs. 2 Ziff. 2 und 5
der Promotionsordnung der
Fakultät für Physik und Astronomie
der Julius-Maximilians-Universität Würzburg

Hiermit erkläre ich ehrenwörtlich, dass ich die Dissertation selbstständig und ohne Hilfe eines Promotionsberaters angefertigt und keine weiteren als die angegebenen Quellen und Hilfsmittel benutzt habe.

Die Dissertation wurde bisher weder vollständig noch teilweise einer anderen Hochschule mit dem Ziel einen akademischen Grad zu erwerben vorgelegt.

Am 15. November 2006 wurde mir von der Julius-Maximilians-Universität Würzburg der akademische Grad "Diplom-Ingenieurin Univ."verliehen. Weitere akademische Grade habe ich weder erworben noch versucht zu erwerben.

Die Dissertation wurde von Prof. Dr. Vladimir Dyakonov betreut.

Würzburg, den 24. Januar 2011

Maria Hammer